



Measurement of differential cross-sections in $t\bar{t}$ and $t\bar{t}+\text{jets}$ production in the lepton+jets final state in pp collisions at $\sqrt{s} = 13$ TeV using 140 fb^{-1} of ATLAS data

The ATLAS Collaboration

Differential cross-sections for top-quark pair production, inclusively and in association with jets, are measured in pp collisions at a centre-of-mass energy of 13 TeV with the ATLAS detector at the LHC using an integrated luminosity of 140 fb^{-1} . The events are selected with one charged lepton (electron or muon) and at least four jets. The differential cross-sections are presented at particle level as functions of several jet observables, including angular correlations, jet transverse momenta and invariant masses of the jets in the final state, which characterise the kinematics and dynamics of the top–antitop system and the hard QCD radiation in the system with associated jets. The typical precision is 5%–15% for the absolute differential cross-sections and 2%–4% for the normalised differential cross-sections. Next-to-leading-order and next-to-next-to-leading-order QCD predictions are found to provide an adequate description of the rate and shape of the jet-angular observables. The description of the transverse momentum and invariant mass observables is improved when next-to-next-to-leading-order QCD corrections are included.

Contents

1	Introduction	3
2	ATLAS detector	3
3	Data sample	4
4	Monte Carlo samples	5
4.1	Signal simulation samples	5
4.2	NNLO signal simulated samples	6
4.3	Theoretical uncertainties in the signal predictions	7
4.4	Background simulation samples	8
5	Object reconstruction and event selection	9
5.1	Detector-level object reconstruction, identification, calibration and selection	9
5.2	Particle-level object definition	10
5.3	Particle- and detector-level event selection	11
6	Background determination	11
6.1	Background determination from MC samples	12
6.2	Background from fake leptons	12
7	Pseudo-top reconstruction algorithm	12
8	Event yields, observables and detector-level distributions	13
8.1	Event yields	13
8.2	Observables and detector-level distributions	14
9	Cross-section measurement	20
9.1	Unfolding method	20
9.2	Closure and stress tests	23
10	Systematic uncertainties	23
10.1	Total systematic uncertainty	25
11	Results	35
11.1	Differential cross-sections for the $t\bar{t}$ inclusive channel	35
11.2	Differential cross-sections for the $t\bar{t}+1\text{jet}$ channel	40
11.3	Differential cross-sections for the $t\bar{t}+2\text{jets}$ channel	45
11.4	χ^2 and p -values	54
12	Summary and Conclusions	57
	Acknowledgements	58
	References	67

1 Introduction

The production of top-quark pairs ($t\bar{t}$) in proton–proton (pp) collisions provides a testing ground for the Standard Model (SM) at the TeV scale. Differential cross-sections can be used to extract fundamental parameters of the SM, such as the top-quark mass [1, 2] and the strong coupling constant α_s [3], and to derive constraints [3] on the parton distribution functions (PDFs). These measurements are also sensitive to the existence of new physics beyond the SM [4, 5], which would appear as deviations of the measurements from the SM predictions. In addition, for all searches for new physics in which $t\bar{t}$ production constitutes a background, the $t\bar{t}$ differential cross-sections are particularly useful to highlight the differences between Monte Carlo (MC) generators and can be used to tune the parameters of those generators.

The ATLAS [6–17] and CMS [3, 18–28] Collaborations have published measurements of $t\bar{t}$ differential cross-sections at centre-of-mass energies $\sqrt{s} = 7, 8$ and 13 TeV in pp collisions at the LHC [29] using final states containing a pair of leptons or a single lepton plus jets, both in the full phase space using parton-level variables and in fiducial phase-space regions using observables constructed from final-state particles (particle level). These results have been used extensively to improve the modelling of MC generators [30–34] and to reduce the uncertainties in the gluon PDF [35].

The analysis presented here focuses on the study of jet observables, some of which have not been explored in previous analyses, in the $t\bar{t}$ and $t\bar{t}$ +jets systems. In the SM, the top quark decays almost exclusively into a W boson and a b -quark. The signature of a $t\bar{t}$ decay is therefore determined by the W boson decay modes. This analysis makes use of the ℓ +jets ($\ell = e, \mu$) $t\bar{t}$ decay mode, also called the semileptonic channel, where one W boson decays into an electron or a muon and a neutrino, and the other W boson decays into a quark–antiquark pair¹. Since the reconstruction of the top quark depends on its decay products, in the following the top quark is referred to as ‘hadronically or leptonically decaying top quark’, depending on the W boson decay mode.

Absolute and normalised differential cross-sections for the $t\bar{t}$ and $t\bar{t}$ +jets systems are measured as functions of various jet observables to characterise the kinematics, topology and dynamics of the $t\bar{t}$ system and are also sensitive to initial- and final-state quantum chromodynamics (QCD) radiation effects, represented by the production of additional jets. Some of these observables are measured for the first time. State-of-the-art next-to-leading-order (NLO) and next-to-next-to-leading-order (NNLO) QCD predictions interfaced to parton-shower (PS) algorithms are compared with the measurements. The measured particle-level differential cross-sections as functions of the jet observables presented here benefit from the increase in integrated luminosity and the reduced detector-related uncertainties compared to previous publications. In addition, the comparison of NNLO+PS differential cross-sections for jet observables at particle level with the measurements is performed for the first time. Therefore, more stringent tests of perturbative QCD (pQCD) are achieved than in the previous analyses.

2 ATLAS detector

The ATLAS detector [36] at the LHC covers nearly the entire solid angle around the collision point.² It consists of an inner tracking detector surrounded by a thin superconducting solenoid, electromagnetic (EM)

¹ Events in which the W boson decays into an electron or muon through a τ -lepton decay may also meet the selection criteria.

² ATLAS uses a right-handed coordinate system with its origin at the nominal interaction point (IP) in the centre of the detector and the z -axis along the beam pipe. The x -axis points from the IP to the centre of the LHC ring, and the y -axis points upwards. Polar coordinates (r, ϕ) are used in the transverse plane, ϕ being the azimuthal angle around the z -axis. The pseudorapidity is

and hadron calorimeters, and a muon spectrometer incorporating three large superconducting air-core toroidal magnets.

The inner-detector system (ID) is immersed in a 2 T axial magnetic field and provides charged-particle tracking in the range of $|\eta| < 2.5$. The high-granularity silicon pixel detector covers the vertex region and typically provides four measurements per track, the first hit normally being in the insertable B-layer (IBL) installed before Run 2 [37, 38]. It is followed by the silicon microstrip tracker (SCT), which usually provides eight measurements per track. These silicon detectors are complemented by the transition radiation tracker (TRT), which enables radially extended track reconstruction up to $|\eta| = 2.0$. The TRT also provides electron identification information based on the fraction of hits (typically 30 in total) above a higher energy-deposit threshold corresponding to transition radiation.

The calorimeter system covers the pseudorapidity range $|\eta| < 4.9$. Within the region $|\eta| < 3.2$, electromagnetic calorimetry is provided by barrel and endcap high-granularity lead/liquid-argon (LAr) calorimeters, with an additional thin LAr presampler covering $|\eta| < 1.8$ to correct for energy loss in material upstream of the calorimeters. Hadron calorimetry is provided by the steel/scintillator-tile calorimeter, segmented into three barrel structures with $|\eta| < 1.7$, and two copper/LAr hadron endcap calorimeters. The solid angle coverage is completed with forward copper/LAr and tungsten/LAr calorimeter modules optimised for electromagnetic and hadronic energy measurements respectively.

The muon spectrometer (MS) comprises separate trigger and high-precision tracking chambers measuring the deflection of muons in a magnetic field generated by the superconducting air-core toroidal magnets. The field integral of the toroids ranges between 2.0 and 6.0 T m across most of the detector. Three layers of precision chambers, each consisting of layers of monitored drift tubes, cover the region $|\eta| < 2.7$, complemented by cathode-strip chambers in the forward region, where the background is highest. The muon trigger system covers the range $|\eta| < 2.4$ with resistive-plate chambers in the barrel, and thin-gap chambers in the endcap regions.

Interesting events are selected by the first-level trigger system implemented in custom hardware, followed by selections made by algorithms implemented in software in the high-level trigger [39]. The first-level trigger accepts events from the 40 MHz bunch crossings at a rate below 100 kHz, which the high-level trigger further reduces in order to record events to disk at about 1 kHz.

An extensive software suite [40] is used in data simulation, in the reconstruction and analysis of real and simulated data, in detector operations, and in the trigger and data acquisition systems of the experiment.

3 Data sample

The data used in this analysis were collected with the ATLAS detector during the pp collision running periods of 2015–2018, when the LHC operated at a centre-of-mass energy of $\sqrt{s} = 13$ TeV. Only events taken during stable beam conditions and satisfying detector- and data-quality requirements [41], which include the calorimeters, muon system and inner tracking detectors operating normally, are considered. The total integrated luminosity of the collected sample is 140 fb^{-1} . The uncertainty in the combined 2015–2018 integrated luminosity is 0.83% [42], obtained using the LUCID-2 detector [43] for the primary luminosity measurements, complemented by measurements using the inner detector and calorimeters.

defined in terms of the polar angle θ as $\eta = -\ln \tan(\theta/2)$ and is equal to the rapidity $y = \frac{1}{2} \ln \left(\frac{E+p_z c}{E-p_z c} \right)$ in the relativistic limit. Angular distance is measured in units of $\Delta R \equiv \sqrt{(\Delta y)^2 + (\Delta \phi)^2}$.

4 Monte Carlo samples

Samples of MC generated events are used to study the characteristics of the signal events. These samples are also used to perform the unfolding procedure to obtain the measured cross-sections. In addition, several MC samples are used to determine the background to the signal process, except for the background from misidentified or non-prompt leptons (called ‘fakes’ background), which relies instead on a data-driven technique (see Section 6). All the MC samples are described below and summarised in Table 1.

Most of the samples of generated events were passed through a full detector simulation [44] based on the GEANT4 [45] program. Other samples, used for estimating some of the systematic uncertainties, were produced using the fast simulation software Atfast-II. All MC samples were reconstructed and analysed by the same algorithms as for the data.

Pile-up from additional pp collisions in the same and neighbouring bunch crossings was simulated by overlaying each MC event with a variable number of simulated inelastic pp collisions generated using PYTHIA 8.186 [46] with the ATLAS set of tuned parameters for minimum-bias events (A3 tune) [47]. The MC events were weighted (‘pile-up reweighting’) so that the distribution of the average number of interactions per bunch crossing matches that observed in the data.

4.1 Signal simulation samples

In this section the MC generators used for the simulation of the $t\bar{t}$ event samples are described for the nominal sample, the alternative samples used to estimate systematic uncertainties and the other samples used in the comparisons of the measured differential cross-sections. The top-quark mass (m_t) and width were set to 172.5 GeV and 1.32 GeV [48], respectively, in all samples; additional samples, in which m_t and the width of the top quark were varied, are used to study the effect of these parameters (see below).

The nominal signal $t\bar{t}$ events were generated using the NLO matrix elements (MEs) implemented in the POWHEG-BOX v2 [49–52] generator with the NNPDF3.0NLO PDF set [35]. Events where both top quarks decayed hadronically were not included. The PS, fragmentation, and the underlying events were simulated using PYTHIA 8.230 [53] with the NNPDF2.3LO PDF set [54] and the A14 tune [55]. The h_{damp} parameter, which controls the p_T of the first gluon emission beyond the Born configuration in POWHEG-BOX v2, was set to $1.5 m_t$ [31]. The main effect of this parameter is to regulate the high- p_T emission against which the $t\bar{t}$ system recoils. Signal $t\bar{t}$ events generated with these settings are referred to as the nominal signal sample. In all the following figures and tables the predictions based on this MC sample are referred to as ‘PwG+PY8’.

Additional signal samples were generated for estimating modelling uncertainties (see Section 10). These samples are:

- Events were generated using the same POWHEG-BOX v2 set-up but interfaced to HERWIG 7.1.3 [56, 57], which includes an angular-ordered PS model. This sample was generated using the H7.1-Default tune [58] and the MMHT2014LO PDF set [59] in the PS. This MC sample is referred to as ‘PwG+Hw7’.
- Events were generated with MADGRAPH5_AMC@NLO 2.3.3 [60] and the NNPDF3.0NLO PDF set. The PS, fragmentation, and the underlying events were simulated using HERWIG 7.1.3 with

the MMHT2014LO PDF set and the H7.1-Default tune. This MC sample is referred to as ‘aMC@NLO+Hw7’.

- Events were generated with SHERPA 2.2.12 [61], which models the zero and one additional-parton processes at NLO accuracy and up to four additional partons at leading-order (LO) accuracy using the MEPS@NLO prescription [62], with the NNPDF3.0NNLO PDF set [35]. The matrix elements were calculated with the COMIX [63] and OPENLOOPS [64–66] libraries. The calculation uses its own parton-shower tune and hadronisation model [67]. These MC samples are referred to as ‘SHERPA 2.2.12’.
- A sample was produced with the same settings as the nominal PwG+Py8 sample but with the h_{damp} parameter set to $3 m_t$. This MC sample is referred to as ‘PwG+Py8 h_{damp} ’.
- Two other PwG+Py8 samples with $m_t = 169$ GeV or $m_t = 176$ GeV were also generated. All other parameters remained the same as in the nominal PwG+Py8 sample, except for the width of the top quark, which was set to 1.23 GeV and 1.42 GeV for $m_t = 169$ GeV and $m_t = 176$ GeV, respectively. These MC samples are referred to as ‘PwG+Py8 m_t ’.

All the samples mentioned above, except for that used to unfold the data (see Section 9), were processed using fast simulation. All these MC predictions were normalised to NNLO plus next-to-next-to-leading-log (NNLL) calculations in pQCD using a k -factor. The cross-section used to evaluate the k -factor is $\sigma_{t\bar{t}} = 832_{-29}^{+20}$ (scale) ± 35 (PDF, α_s) ± 23 (m_t) pb, as calculated with the Top++2.0 [68–74] program at NNLO in pQCD, including soft-gluon resummation at NNLL, and assuming $m_t = 172.5$ GeV. This calculation does not include electroweak corrections. The first uncertainty comes from the independent variation of the factorisation (μ_F) and renormalisation (μ_R) scales, the second one is associated with variations in the PDFs and α_s , following the PDF4LHC prescription [75] with the MSTW2008 NNLO at 68% confidence-level error [76], CT10 NNLO [77] and NNPDF2.3 5f FFN [54] PDF sets, and the third uncertainty arises from the assumed value of m_t .

4.2 NNLO signal simulated samples

The first matched computation of top-quark pair production at NNLO in QCD, including all-order radiative corrections as implemented via PS simulations, is reported in Ref. [78] and referred to as the MiNNLOPS procedure. This procedure involves three steps. In the first step, $t\bar{t}$ pairs plus one light parton were generated using the POWHEG-BOX v2 program, which provides a NLO calculation and includes a second light parton. The second step involves the calculation of the limit in which the light partons generated in the previous step become collinear to the $t\bar{t}$ pair; appropriate Sudakov form factors and higher-order terms are used to guarantee that the calculation remains finite and accurate at NNLO for inclusive $t\bar{t}$ production. The third step includes the generation of the kinematics of the second radiated parton using POWHEG-BOX v2, which was accounted for only inclusively in the first step; in this way, the NLO accuracy of the $t\bar{t}$ +jet cross-section is preserved. After this third step, subsequent radiation was generated using the PS method of PYTHIA. For the generation of this sample, the NNPDF3.0NNLO PDF set was used. In addition to the PS step, PYTHIA 8.245 was also used for the fragmentation and underlying-event simulation with the NNPDF2.3LO PDF set and the A14 tune.

This prediction was also normalised to $O(\text{NNLO}+\text{NNLL})$ in pQCD using the cross-section $\sigma_{t\bar{t}} = 832$ pb calculated with the Top++2.0 program, as mentioned above. In all the following figures and tables the predictions based on this sample are referred to as ‘PwG+Py8 MiNNLOPS’.

Table 1: Summary of signal and background MC samples, showing the event generator for the hard-scattering process, the order in pQCD of the cross-section used for normalisation together with its value and total uncertainty, the PDF choice, as well as the parton-shower generator and the corresponding tune used.

Physics process	Generator	PDF set for hard process	Parton shower	Tune	Cross-section normalisation σ (pQCD order)
Signal samples:					832 \pm 51 pb (NNLO+NNLL)
– PwG+Py8	POWHEG-Box v2	NNPDF3.0NLO	PYTHIA 8.230	A14	
– PwG+Hw7	POWHEG-Box v2	NNPDF3.0NLO	HERWIG 7.1.3	H7.1-Default	
– aMC@NLO+Hw7	MADGRAPH5_AMC@NLO 2.3.3	NNPDF3.0NLO	HERWIG 7.1.3	H7.1-Default	
– SHERPA 2.2.12	SHERPA 2.2.12	NNPDF3.0NNLO	SHERPA	SHERPA	
– PwG+Py8 MiNNLOPS	POWHEG-Box v2	NNPDF3.0NNLO	PYTHIA 8.245 + MiNNLOPS	A14	
Background samples:					
– single-top quark samples:					
<i>s</i> -channel (top)					6.4 \pm 0.2 pb (NLO)
<i>s</i> -channel (anti-top)					3.4 \pm 0.2 pb (NLO)
<i>t</i> channel (top)					136 \pm 5 pb (NLO)
<i>t</i> channel (anti-top)					81 \pm 4 pb (NLO)
<i>tW</i> channel					72 \pm 4 pb (NLO+NNLL)
• PwG+Py8	POWHEG-Box v2	NNPDF3.0NLO	PYTHIA 8.230	A14	
• PwG+Hw7	POWHEG-Box v2	NNPDF3.0NLO	HERWIG 7.0.4	H7-UE-MMHT	
– W+jets	SHERPA 2.2.1	NNPDF3.0NNLO	SHERPA	SHERPA	20100 \pm 1000 pb (NNLO)
– Z+jets	SHERPA 2.2.1	NNPDF3.0NNLO	SHERPA	SHERPA	1906 \pm 95 pb (NNLO)
– diboson	SHERPA 2.2.2	NNPDF3.0NNLO	SHERPA	SHERPA	211 \pm 8 pb (NLO)
– <i>t</i> \bar{t} V	MADGRAPH5_AMC@NLO 2.3.3	NNPDF3.0NLO	PYTHIA 8.230	A14	1.5 \pm 0.1 pb (NLO)
– <i>t</i> \bar{t} H	POWHEG-Box v2	NNPDF3.0NLO	PYTHIA 8.230	A14	0.51 \pm 0.05 pb (NLO)

4.3 Theoretical uncertainties in the signal predictions

The theoretical uncertainties in the differential cross-section predictions are estimated in the following way:

- The uncertainties in the QCD predictions from PwG+Py8 and PwG+Py8 MiNNLOPS due to higher-order terms are estimated by repeating the calculations using values of μ_R and μ_F scaled by factors 0.5 and 2; the scales are varied independently.
- The uncertainty in the QCD predictions from PwG+Py8 due to the uncertainty in the proton PDFs is estimated using the 100 replicas from the NNPDF3.0 analysis [35].
- The uncertainty in the QCD predictions from PwG+Py8 due to the uncertainty in α_s is estimated by repeating the calculations using two additional sets of proton PDFs from the NNPDF3.0 analysis, for which different values of α_s at the mass of the Z boson are assumed in the fits, namely 0.117 and 0.119; in this way, the correlation between α_s and the PDFs is preserved.
- The uncertainties in the QCD predictions from PwG+Py8 and PwG+Py8 MiNNLOPS due to the amount of initial- and final-state radiation in the PS are assessed by varying the corresponding parameter of the A14 PS tune (Var3c) and by varying the scale μ_R^{FSR} by factors of 2 and 0.5.

The total theoretical uncertainty in the NLO differential cross-section predictions of POWHEG is obtained by adding in quadrature the uncertainties listed above and it is dominated by the contribution from the scale variations. The total theoretical uncertainty is approximately 10% to 15% for the theoretical predictions from POWHEG as functions of the angular observables, whereas for the transverse-momentum and invariant-mass observables the uncertainty rises to approximately 34% to 42% in the tail of the distributions. The uncertainty from the scale variations in the aMC@NLO predictions is very similar to

that of POWHEG. For the SHERPA 2.2.12 predictions, it is a factor between approximately one and three times larger than for POWHEG. This increase in the uncertainty for the SHERPA calculation is expected due to the presence of a matrix element calculation with up to four additional partons at LO. These LO terms lead to larger uncertainties when varying the scales. For POWHEG and aMC@NLO these LO terms are absent and handled by the PS at lower accuracy and, when comparing these uncertainties with those from SHERPA 2.2.12, it is necessary to take into account the fact that these uncertainties in POWHEG and aMC@NLO are only partly evaluated since not all contributions to the uncertainty can be estimated.

For PWG+PY8 MiNNLOPS, only scale variations are available; in these calculations at NNLO, a significant reduction of the scale uncertainty relative to those for the NLO calculations is obtained. The uncertainties due to the PDFs and α_s are expected to be similar to, or smaller than, those affecting the NLO prediction [79]; the uncertainty due to the scale variations in the NNLO prediction is still larger than those arising from the PDFs and α_s uncertainties. For the comparison with the data in Section 11, the total uncertainty associated with the PWG+PY8 MiNNLOPS prediction is taken as the sum in quadrature of the scale uncertainties, the uncertainties in the PS and, as an approximation, the uncertainties due to the PDFs and α_s as estimated from PWG+PY8 at NLO.

4.4 Background simulation samples

Several processes can produce the same final state as the $t\bar{t} \ell$ +jets decay mode. The events produced by these backgrounds need to be estimated and subtracted from the data to determine the top-quark pair cross-sections. The MC simulation used for these background processes are described below:

- Single top-quark production processes in the t - and s -channels and in association with a W boson were modelled at NLO in QCD using POWHEG-BOX v2 with the NNPDF3.0NLO PDF set. The PS and hadronisation effects were simulated with PYTHIA 8.230, using the A14 tune and the NNPDF2.3LO PDF set. The t -channel sample was generated with the four-flavour scheme. The diagram-removal scheme (DR) [80] was employed in the tW simulation to handle the interference with $t\bar{t}$ production [31]. The single-top-quark cross-section for the tW channel was normalised using its NLO+NNLL prediction, while the t - and s -channels were normalised using their NLO predictions [81–85]. Events generated using the diagram-subtraction method [86] (DS) instead of the DR technique were considered as a systematic uncertainty in the modelling of this background (see Section 10). In addition, events generated with POWHEG-BOX v2 and interfaced to HERWIG 7.0.4 were also generated using the H7-UE-MMHT tune [58] and the MMHT2014LO PDF.
- Events containing a W or Z boson in association with jets (W +jets and Z +jets) were simulated with the SHERPA 2.2.1 generator using NLO-accurate MEs for up to two jets, and MEs accurate to LO for up to four jets calculated with the COMIX and OPENLOOPS libraries. They were matched to the SHERPA PS using the ME+PS@NLO prescription and the tune developed by the SHERPA authors with the NNPDF3.0NNLO PDF set. The W +jets and Z +jets predictions were normalised to the NNLO cross-sections [87].
- Diboson production (WW , ZZ and WZ), with one of the bosons decaying hadronically and the other leptonically, was generated using SHERPA 2.2.2 with MEs computed at NLO accuracy in QCD with up to one additional parton and at LO accuracy with up to three additional partons. The NNPDF3.0NNLO PDF set was used. These predictions were normalised to the NLO cross-sections evaluated by the generator.

- The MADGRAPH5_AMC@NLO 2.3.3 generator was used for the production of $t\bar{t}V$, with $V = W, Z$. The events were modelled at NLO with the NNPDF3.0NLO PDF set. PYTHIA 8.230 with the A14 tune and the NNPDF2.3LO PDF set was used to simulate the PS. These predictions were normalised to the NLO cross-sections evaluated by the generator.
- The production of $t\bar{t}H$ events was modelled at NLO using the POWHEG-BOX v2 generator with the NNPDF3.0NLO PDF set. PYTHIA 8.230 with the A14 tune and the NNPDF2.3LO PDF set was used to simulate the PS. These predictions were normalised to the fixed-order calculation including NLO QCD and electroweak corrections [88].

5 Object reconstruction and event selection

The following sections describe the detector- and particle-level objects used to characterise the final-state event topology and to define the fiducial phase-space regions for the measurements.

5.1 Detector-level object reconstruction, identification, calibration and selection

Primary vertices are formed from reconstructed tracks that are spatially compatible with the interaction region. The hard-scatter primary vertex is chosen to be the one with at least two associated tracks and the highest $\sum p_T^2$, where the sum extends over all tracks with $p_T > 0.5$ GeV matched to the given vertex [89].

Electron candidates are reconstructed by matching tracks in the ID to energy deposits in the EM calorimeter [90]. The electron candidates are required to have a transverse momentum $p_T > 27$ GeV and a pseudorapidity $|\eta| < 2.47$, excluding the transition region between the barrel and endcap calorimeters ($1.37 < |\eta| < 1.52$). The longitudinal impact parameter z_0 of the associated track is required to satisfy $|z_0 \sin \theta| < 0.5$ mm, where θ is the polar angle of the track, and the transverse impact parameter significance $|d_0|/\sigma(d_0) < 5$, where d_0 is the transverse impact parameter and $\sigma(d_0)$ is its uncertainty. The impact parameters z_0 and d_0 are calculated relative to the beam spot and the beam line, respectively. The electron candidates must satisfy a ‘tight’ likelihood-based identification criterion based on shower shape and track selection requirements [90]. The candidates must also satisfy p_T - and η -dependent isolation requirements based on tracks and energy clusters, defined for the ‘tight’ isolation working point [90]; these isolation requirements are used to reduce the background from jets misidentified as prompt leptons (fake leptons) or due to semileptonic decays of heavy-flavour hadrons (non-prompt real leptons).

Muon candidates are reconstructed by combining tracks reconstructed in the ID and the MS [91]. The track p_T is determined through a global fit to the hits, which takes into account the energy loss in the calorimeters. The track associated with the muon candidate must have $|z_0 \sin \theta| < 0.5$ mm and $|d_0|/\sigma(d_0) < 3$. Candidates are required to have $p_T > 27$ GeV and $|\eta| < 2.5$. To reduce the background from muons originating from heavy-flavour decays inside jets, muons are required to be isolated using track-quality and isolation criteria similar to those applied to electrons [91].

Jets are reconstructed using the anti- k_t algorithm [92] with radius parameter $R = 0.4$ as implemented in the FASTJET package [93]. Jet reconstruction is performed on particle flow objects (PFlow) [94]. The PFlow algorithm directly combines measurements from both the tracker and the calorimeter to form the input signals for jet reconstruction, which are intended to approximate individual particles. They are calibrated to be consistent with electromagnetic clusters using corrections determined in simulation and

inferred from test-beam data. Jet four-momenta are then corrected for pile-up effects using the jet-area method [95]. To reduce the number of jets originating from pile-up, an additional selection criterion based on a jet-vertex tagging (JVT) technique is applied. The JVT is a likelihood discriminant that combines information from several track-based variables [96] and the criterion is only applied to jets with $p_T < 60$ GeV and rapidity $|y| < 2.4$. The jet energy and direction are calibrated using an energy- and η -dependent simulation-based calibration scheme with in situ corrections based on data [97]. The jets are selected if they have $p_T > 25$ GeV and $|y| < 2.5$.

To identify jets containing b -hadrons, a flavour tagging algorithm called DL1r [98] based on a deep neural network is used. In this approach, the jet flavours are considered equally during training and multiple output nodes are used, each node trained to predict a specific jet flavour, which provides a highly flexible tagger. The input information is a combination of several discriminants. Jets are considered as b -tagged if the value of the DL1r-algorithm output is larger than a certain threshold that provides a 70% b -jet tagging efficiency obtained in $t\bar{t}$ MC events. The working point of 70% is selected after studying the number of events obtained in data, contributions from the different types of background processes and systematic uncertainties.

To remove ambiguities in the identification of the objects mentioned above, a procedure called ‘overlap removal’ is applied to assign a unique hypothesis to each object. If a muon shares a track with an electron, it is likely to have undergone bremsstrahlung and hence the electron is not selected. To prevent double-counting of electron energy deposits as jets, the jet closest to a reconstructed electron is discarded if $\Delta R(\text{jet}, e) < 0.2$. Subsequently, to reduce the impact of non-prompt electrons, if $\Delta R(\text{jet}, e) < 0.4$, then that electron is removed. In cases where a jet is within $\Delta R(\text{jet}, \mu) = 0.4$ of a muon, if the jet has fewer than three tracks the jet is removed whereas if the jet has at least three tracks the muon is removed.

The missing transverse momentum in the event, whose magnitude is denoted in the following by E_T^{miss} , is defined as the negative vector sum of the p_T of the reconstructed and calibrated objects in the event [99]. This sum also includes the momenta of the ID tracks that are matched to the primary vertex but are not associated with any other reconstructed objects.

5.2 Particle-level object definition

Particle-level objects are defined in simulated events using only stable particles, which are defined as those with a proper lifetime $\tau > 30$ ps. The fiducial phase space used for the measurements in this analysis is defined using a series of requirements applied to particle-level objects analogous to those used in the selection of the detector-level objects.

Electrons and muons are required to not originate from a generated hadron in the MC event, either directly or through a τ -lepton decay. This ensures that the lepton comes from an electroweak decay without requiring a direct match to a W boson. Events where the W boson decays into a leptonically decaying τ -lepton are accepted. The four-momenta of the bare leptons are then modified by adding the four-momenta of all photons, not originating from hadron decay, within a cone of size $\Delta R = 0.1$, to take into account final-state photon radiation. Such ‘dressed leptons’ are then required to have $p_T > 27$ GeV and $|\eta| < 2.5$.

Particle-level jets are reconstructed using the same anti- k_r algorithm used at the detector level with $R = 0.4$. The jet-reconstruction procedure takes as input all stable particles, except for charged leptons and neutrinos not from hadron decay as described above. Particle-level jets are required to have $p_T > 25$ GeV and $|y| < 2.5$.

A particle-level jet is identified as a b -jet if a hadron with $p_T > 5$ GeV containing a b -quark is matched to the jet through the ghost-matching technique described in Ref. [95].

Particle-level objects are subject to different overlap removal criteria than reconstructed objects. After lepton dressing and jet clustering, events in which the separation of the selected charged lepton and a jet is $\Delta R < 0.4$ are excluded. This removes 6.5% of the events at particle level.

Neutrinos from hadron decays, either directly or via a τ -lepton decay, are not considered. All other neutrinos are included. The particle-level missing transverse momentum is calculated from the four-vector sum of these selected neutrinos.

5.3 Particle- and detector-level event selection

The event selection comprises a set of requirements based on the general event quality and on the reconstructed objects, defined above, that characterise the final-state event topology. The event selection follows closely that of the previous analysis [17]. In addition in this analysis, three channels are selected according to the number of jets in the final state. The selection described below is applied to the reconstruction-level objects in the data and the MC samples. A similar event selection is applied to the particle-level objects in the MC, except for the trigger and primary vertex requirements.

Events were selected online during data taking by single-electron [100] or single-muon [101] triggers. Multiple triggers were combined in a logical OR to increase the selection efficiency. The lowest-threshold triggers utilised isolation requirements to reduce the trigger rate. The isolated-lepton triggers had p_T thresholds of 20 GeV for muons and 24 GeV for electrons in 2015 data, and 26 GeV for both lepton types in 2016, 2017 and 2018 data. They were complemented by other triggers with higher p_T thresholds but no isolation requirements to increase the trigger efficiency.

Offline, events are required to have a reconstructed primary vertex with two or more associated tracks and to contain exactly one reconstructed charged-lepton (electron or muon) candidate with $p_T > 27$ GeV. Each event is also required to contain at least four jets with $p_T > 25$ GeV and $|y| < 2.5$, of which at least two must be tagged as b -jets. This is the first channel studied, called ‘ $t\bar{t}$ inclusive’. The second channel is selected by requiring at least five jets and called ‘ $t\bar{t}+1\text{jet}$ ’. The third channel is selected by requiring the presence of at least six jets and called ‘ $t\bar{t}+2\text{jets}$ ’. In this way, the $t\bar{t}+2\text{jets}$ sample is a subset of the $t\bar{t}+1\text{jet}$ and the $t\bar{t}+1\text{jet}$ is a subset of the $t\bar{t}$ inclusive sample.

6 Background determination

After the event selection explained in Section 5.3, various backgrounds contribute to the event yields. Data-driven techniques are used to estimate the background that derives from events containing jets mimicking the signature of charged leptons or leptons from hadron decays, for which precise enough simulations are not available. Background from other physics processes, which include leptons in the final state, are taken into account using the MC samples described in Section 4.4.

Dilepton top-quark pair events (including decays into τ -leptons) can satisfy the event selection and are considered in the analysis as signal at both the detector and particle levels. All the $t\bar{t}$ semileptonic events that satisfy the fiducial selection described in Section 5.3 are considered as signal. For this reason, the leptonically decaying top quark decays into τ -leptons are considered as signal only if the τ -lepton decays

leptonically. Cases where both top quarks decay into a τ -lepton, which in turn decays into hadrons, are accounted for in the multijet background.

6.1 Background determination from MC samples

The single-top-quark background, comprising t -channel, s -channel and tW production modes, constitutes the largest contribution, amounting to 4.3%, 3.6% and 3.1% of the total event yield for the $t\bar{t}$ inclusive, $t\bar{t}+1\text{jet}$ and $t\bar{t}+2\text{jets}$ channels, respectively. The W +jets background represents the second largest contribution to the background, amounting to 2.3%, 1.9% and 1.8% for the three channels, respectively. The background contributions from each of the Z +jets, diboson, $t\bar{t}V$ and $t\bar{t}H$ samples of events to the total yield is smaller than 1% for all three channels.

6.2 Background from fake leptons

Multijet production processes, including the production of hadronically decaying $t\bar{t}$ pairs, have a large cross-section and mimic the ℓ +jets signature due to fake leptons or non-prompt real leptons. The multijet background is estimated directly from data using a matrix method [102]. The estimate is based on the introduction of a ‘loose’ lepton definition, obtained by removing the isolation requirement and loosening the identification criteria given in Section 5.1. The number of fake and non-prompt leptons contained in the signal region is evaluated by inverting the matrix that relates the number of ‘loose’ and ‘tight’ leptons to the number of real and fake leptons. This matrix is built using the efficiencies for fake and real leptons to satisfy the ‘tight’ selection. The fake-lepton efficiency is measured using data in control regions dominated by multijet background with the real-lepton contribution subtracted using MC simulation. The real-lepton efficiency is extracted by applying a tag-and-probe technique using leptons from Z boson decays. The multijet background (called fakes) contributes 1.4%, 1.3% and 1.3% to the total event yield of each of the three channels, respectively.

7 Pseudo-top reconstruction algorithm

The pseudo-top algorithm [8] is used to reconstruct the leptonically and hadronically decaying top quarks. This algorithm reconstructs the four-momenta of the top quarks and their complete decay chain from final-state objects, namely the charged lepton (electron or muon), missing transverse momentum, and four jets, two of which are b -tagged, using the same method both at detector and particle levels which is described below.

First, the two b -jet candidates are chosen. In events with more than two b -jet candidates, only the two with the highest p_T values are considered as the b -jets from the decay of the top quarks, and called ‘jet-b1’ and ‘jet-b2’, with $p_T^{\text{jet-b1}} > p_T^{\text{jet-b2}}$. The rest of the jets are considered as non b -jet candidates.

The two non- b -tagged jets to form the hadronically decaying W boson are chosen from the available jets in each event (excluding those already tagged as coming from a b -quark) such that the invariant mass of the pair is closest to m_W and called ‘jet-W1’ and ‘jet-W2’, with $p_T^{\text{jet-W1}} > p_T^{\text{jet-W2}}$.

For the neutrino, the x and y components of its transverse momentum are taken from the corresponding components of the missing transverse momentum, whereas the z component is calculated by imposing the

W boson mass constraint on the invariant mass of the charged-lepton–neutrino system. If the resulting quadratic equation has two real solutions, the one with the smaller value of $|p_z|$ is chosen. If the discriminant is negative, only the real part is considered.

The leptonically decaying W boson is reconstructed from the charged lepton and the neutrino. The leptonically decaying top quark is reconstructed from the leptonically decaying W boson and the b -tagged jet closest (jet-b1 or jet-b2) in ΔR to the charged lepton. The hadronically decaying W boson is reconstructed from the two non- b -tagged jets (jet-W1 and jet-W2) whose invariant mass is closest to the mass of the W boson, as mentioned above, and the hadronically decaying top quark is reconstructed from the hadronically decaying W boson and the other b -tagged jet. This choice yields the best performance of the algorithm in terms of the correspondence between the detector and particle levels.

8 Event yields, observables and detector-level distributions

8.1 Event yields

The individual e +jets and μ +jets channels have very similar distributions at detector level, therefore they are combined by summing the distributions. Table 2 shows the final yields from the three channels for the combined ℓ +jets decay mode for data, signal and background events. The selection leads to a sample with an expected background of 9%, 8% and 8% for the three channels, respectively. The overall difference between the data and the predictions is 2%, 2% and 1% for the three channels, which means that there is a good agreement between the SM prediction and the data, after taking into account the systematic uncertainties (see Section 10).

Table 2: Observed and expected number of events in the ℓ +jets decay mode after the full event selection. The systematic uncertainties (see Section 10) are also included. Due to correlations, the quadratic sum of the different systematic uncertainties might not add up to the total systematic uncertainties.

Process	Yield for channel		
	$t\bar{t}$ inclusive	$t\bar{t}$ +1jet	$t\bar{t}$ +2jets
$t\bar{t}$	4 120 000 \pm 690 000	2 110 000 \pm 420 000	860 000 \pm 240 000
single-top quark	194 000 \pm 33 000	82 000 \pm 19 000	28 900 \pm 8 300
W +jets	103 000 \pm 53 000	44 000 \pm 23 000	17 200 \pm 8 900
fakes	66 000 \pm 33 000	30 000 \pm 15 000	12 000 \pm 6 000
Z +jets	37 000 \pm 19 000	14 600 \pm 7 600	5 400 \pm 2 800
$t\bar{t}V$	13 100 \pm 1 100	10 300 \pm 900	6 470 \pm 660
diboson	6 000 \pm 600	2 820 \pm 350	1 220 \pm 180
$t\bar{t}H$	5 460 \pm 320	4 710 \pm 310	3 260 \pm 270
Total SM prediction	4 540 000 \pm 710 000	2 300 000 \pm 440 000	940 000 \pm 240 000
Data	4 445 113	2 248 410	924 751

8.2 Observables and detector-level distributions

Measurements of differential cross-sections in the $t\bar{t}$ inclusive, $t\bar{t}+1\text{jet}$ and $t\bar{t}+2\text{jets}$ channels, as defined in Section 5.3, are performed as functions of different jet observables.

In the following, the two jets used to reconstruct the hadronically decaying W boson are called ‘jet-W1’ and ‘jet-W2, with $p_{\text{T}}^{\text{jet-W1}} > p_{\text{T}}^{\text{jet-W2}}$ (as defined in Section 7). For the $t\bar{t}+1\text{jet}$ and $t\bar{t}+2\text{jets}$ channels, the additional jets, called ‘jet-rad1’ and ‘jet-rad2’, are chosen as follows: ‘jet-rad1’ is the highest p_{T} jet of those that are not part of the $t\bar{t}$ system; and ‘jet-rad2’ is the second-highest p_{T} jet of those that are not part of the $t\bar{t}$ system.

The following observables are measured in the $t\bar{t}$ inclusive channel:

- The kinematics of the two jets forming the W boson are characterised by measuring the transverse momenta of jet-W1 ($p_{\text{T}}^{\text{jet-W1}}$) and jet-W2 ($p_{\text{T}}^{\text{jet-W2}}$) and the absolute value of their rapidities ($|y^{\text{jet-W1}}|$ and $|y^{\text{jet-W2}}|$).
- The topology of the two jets forming the W boson is characterised by measuring $|\Delta y^{\text{jet-W1} - \text{jet-W2}}|$, defined as the absolute value of the difference in rapidity between jet-W1 and jet-W2, and $|\Delta\phi^{\text{jet-W1} - \text{jet-W2}}|$, defined as the absolute value of the difference in azimuth between jet-W1 and jet-W2.

Figure 1 shows the data, backgrounds and signal MC distributions at detector level for these observables. Some differences in shape between the distributions for the data and the SM predictions are observed, especially at high values of $p_{\text{T}}^{\text{jet-W1}}$, which are covered by the systematic uncertainties.

The following observables are measured in the $t\bar{t}+1\text{jet}$ channel:

- The kinematics of the first gluon emission is characterised by measuring the transverse momentum of jet-rad1 ($p_{\text{T}}^{\text{jet-rad1}}$) and the absolute value of its rapidity ($|y^{\text{jet-rad1}}|$).
- The topology of the first gluon emission is characterised by measuring $|\Delta\phi^{\text{toplep} - \text{jet-rad1}}|$, defined as the absolute value of the difference in azimuth between the leptonically decaying top quark (toplep) and jet-rad1, and $|\Delta\phi^{\text{tophad} - \text{jet-rad1}}|$, defined as the absolute value of the difference in azimuth between the hadronically decaying top quark (tophad) and jet-rad1. In addition, the absolute value of the difference in azimuth between jet-W1 and jet-rad1 ($|\Delta\phi^{\text{jet-W1} - \text{jet-rad1}}|$) provides additional insight into the topology of these events.
- The dynamics of the $t\bar{t}+1\text{jet}$ events is characterised by measuring the invariant mass of the $t\bar{t}$ -jet-rad1 system ($m^{t\bar{t} - \text{jet-rad1}}$).

Figure 2 shows the data, backgrounds and signal MC distributions at detector level for these observables. There is an adequate description of the measured distributions by the SM prediction; the $m^{t\bar{t} - \text{jet-rad1}}$ measured distribution is described by the SM prediction, except for the $m^{t\bar{t} - \text{jet-rad1}} > 4$ TeV region.

The following observables are measured in the $t\bar{t}+2\text{jets}$ channel:

- The kinematics of the second gluon emission is characterised by measuring the transverse momentum of jet-rad2 ($p_{\text{T}}^{\text{jet-rad2}}$) and the absolute value of its rapidity ($|y^{\text{jet-rad2}}|$).

- The topology of the second gluon emission is characterised by measuring $|\Delta y^{\text{jet-rad1} - \text{jet-rad2}}|$, defined as the absolute value of the difference in rapidity between jet-rad1 and jet-rad2, and $|\Delta\phi^{\text{jet-rad1} - \text{jet-rad2}}|$, defined as the absolute value of the difference in azimuth between jet-rad1 and jet-rad2. Other angular correlations provide additional insight into the topology of the $t\bar{t}+2\text{jets}$ events: $|\Delta\phi^{\text{tolep} - \text{jet-rad2}}|$, defined as the absolute value of the difference in azimuth between the leptonically decaying top quark and jet-rad2, $|\Delta\phi^{\text{tophad} - \text{jet-rad2}}|$, defined as the absolute value of the difference in azimuth between the hadronically decaying top quark and jet-rad2, and $|\Delta\phi^{\text{jet-W1} - \text{jet-rad2}}|$, defined as the absolute value of the difference in azimuth between jet-W1 and jet-rad2.
- The dynamics of the $t\bar{t}+2\text{jets}$ events is characterised by measuring the invariant mass of the jet-rad1 and jet-rad2 system ($m^{\text{jet-rad1} - \text{jet-rad2}}$).

Figures 3 and 4 show the data, backgrounds and signal MC distributions at detector level for these observables. There is an adequate description of the measured observables by the SM predictions.

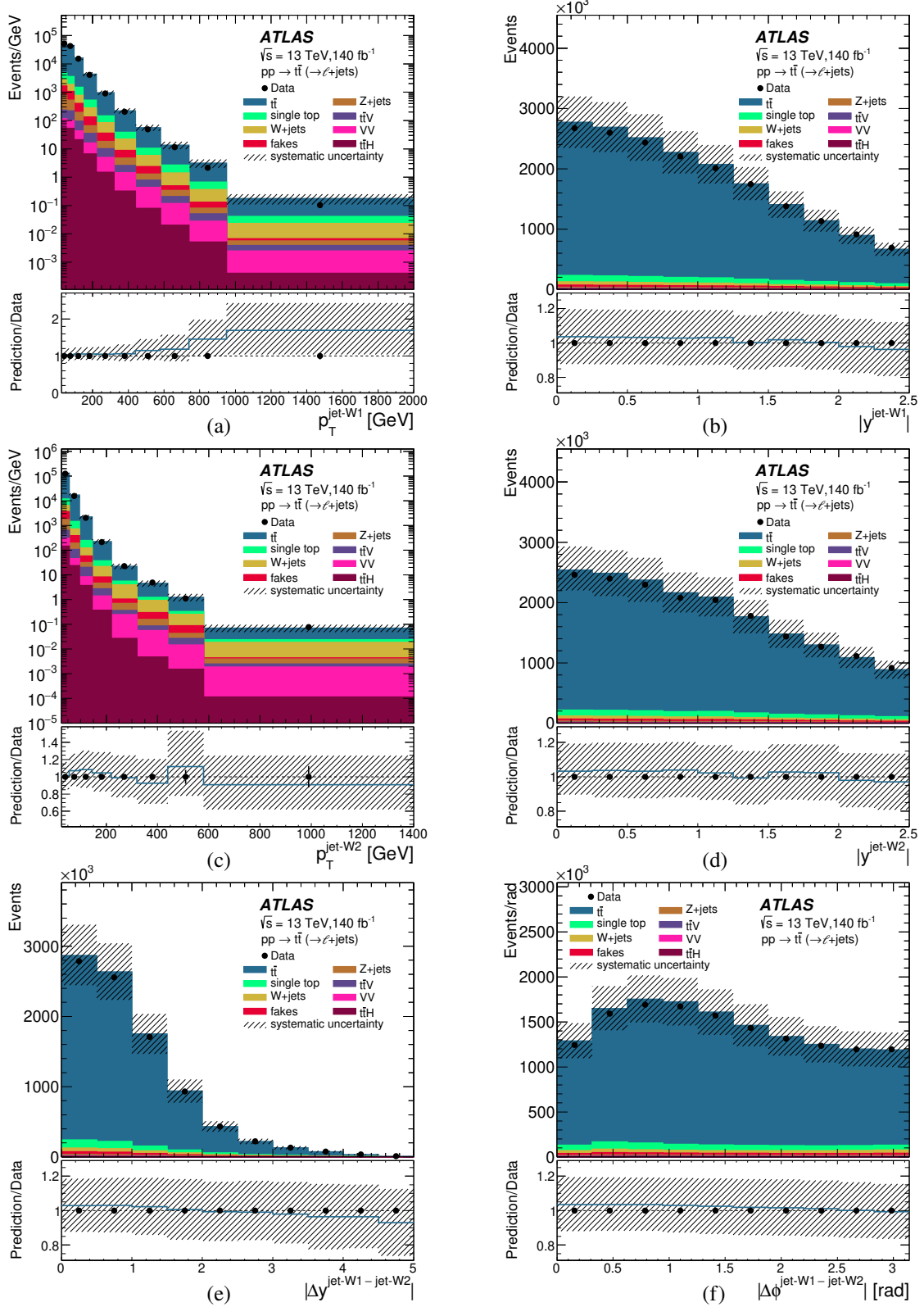


Figure 1: The measured (a) $p_T^{\text{jet-W1}}$, (b) $|y^{\text{jet-W1}}|$, (c) $p_T^{\text{jet-W2}}$, (d) $|y^{\text{jet-W2}}|$, (e) $|\Delta y^{\text{jet-W1-jet-W2}}|$ and (f) $|\Delta\phi^{\text{jet-W1-jet-W2}}|$ distributions divided by the bin width (dots) in the $t\bar{t}$ inclusive channel. The error bars represent the statistical uncertainty in the data; for many points, the uncertainty is smaller than the marker size and, thus, not visible. The hatched bands represent the systematic uncertainties (see Section 10). The prediction of the signal and various backgrounds (histograms) are also included. The lower panels of each figure show the ratio of the total prediction and the data distributions.

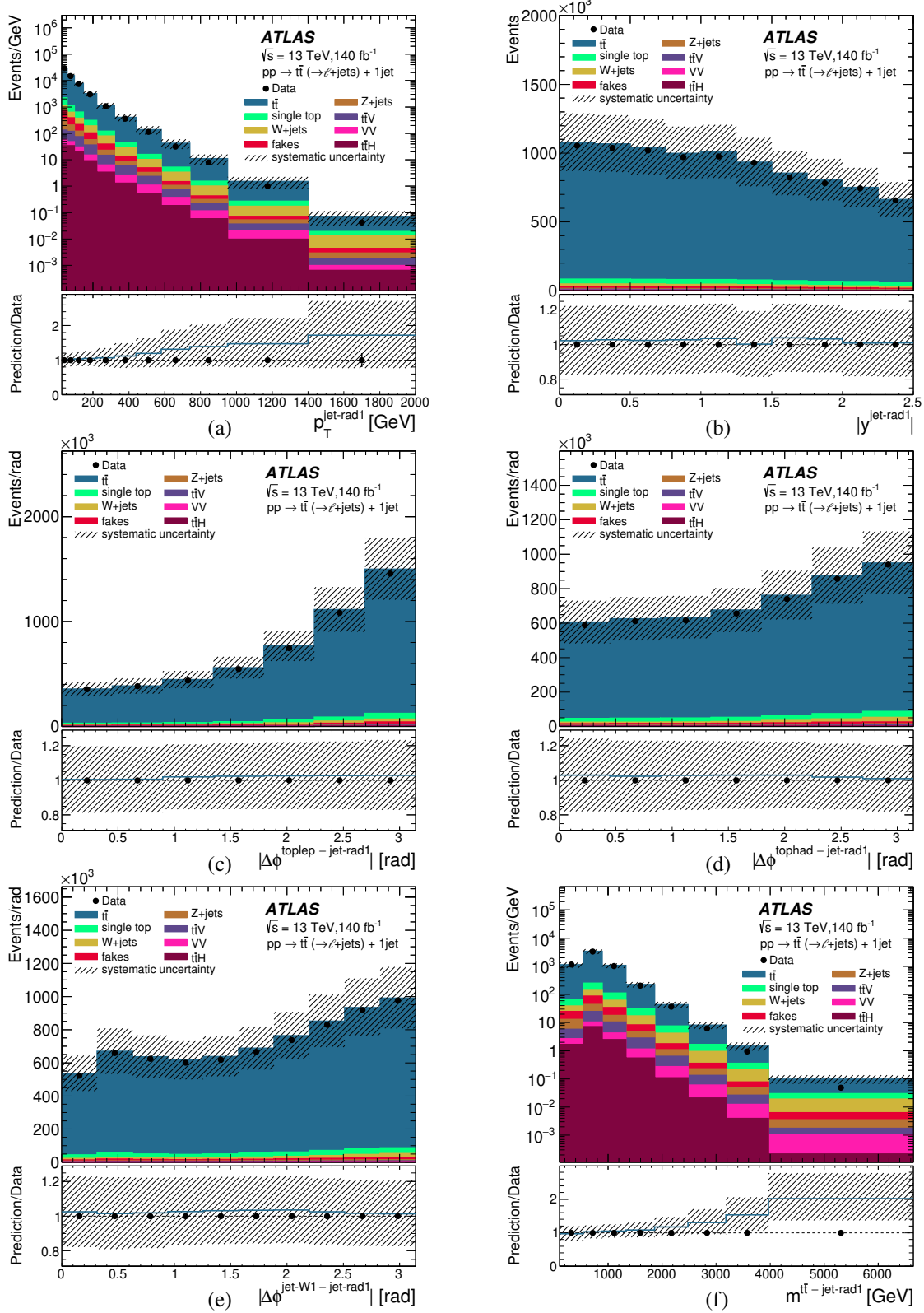


Figure 2: The measured (a) $p_T^{\text{jet-rad1}}$, (b) $|y^{\text{jet-rad1}}|$, (c) $|\Delta\phi^{\text{toplep} - \text{jet-rad1}}|$, (d) $|\Delta\phi^{\text{tophad} - \text{jet-rad1}}|$, (e) $|\Delta\phi^{\text{jet-W1} - \text{jet-rad1}}|$ and (f) $m^{t\bar{t} - \text{jet-rad1}}$ distributions divided by the bin width (dots) in the $t\bar{t}+1\text{jet}$ channel. The error bars represent the statistical uncertainty in the data; for many points, the uncertainty is smaller than the marker size and, thus, not visible. The hatched bands represent the systematic uncertainties (see Section 10). The prediction of the signal and various backgrounds (histograms) are also included. The lower panels of each figure show the ratio of the total prediction and the data distributions.

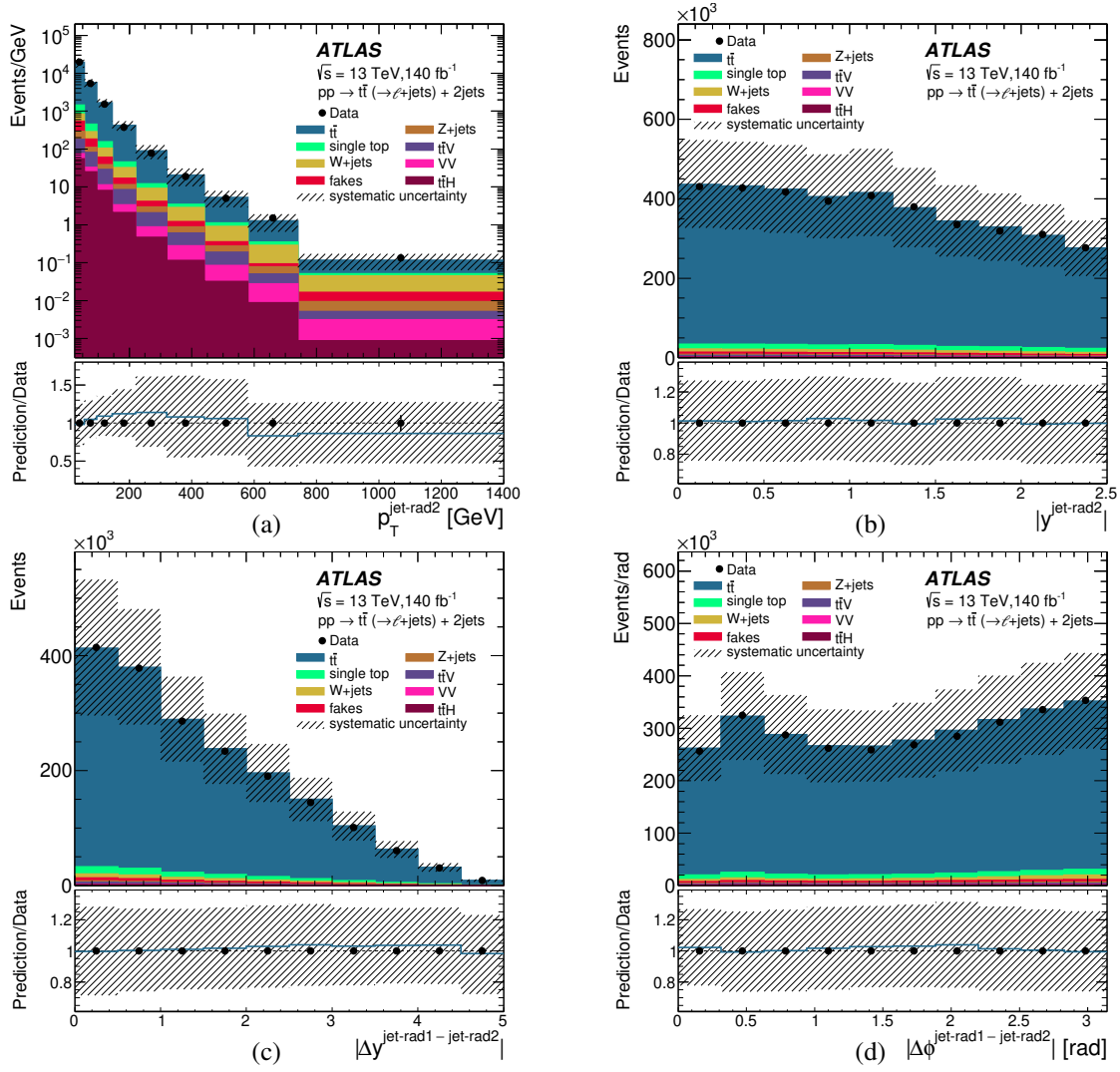


Figure 3: The measured (a) $p_T^{\text{jet-rad2}}$, (b) $|y^{\text{jet-rad2}}|$, (c) $|\Delta y^{\text{jet-rad1} - \text{jet-rad2}}|$ and (d) $|\Delta\phi^{\text{jet-rad1} - \text{jet-rad2}}|$ distributions divided by the bin width (dots) in the $t\bar{t}+2\text{jets}$ channel. The error bars represent the statistical uncertainty in the data; for many points, the uncertainty is smaller than the marker size and, thus, not visible. The hatched bands represent the systematic uncertainties (see Section 10). The prediction of the signal and various backgrounds (histograms) are also included. The lower panels of each figure show the ratio of the total prediction and the data distributions.

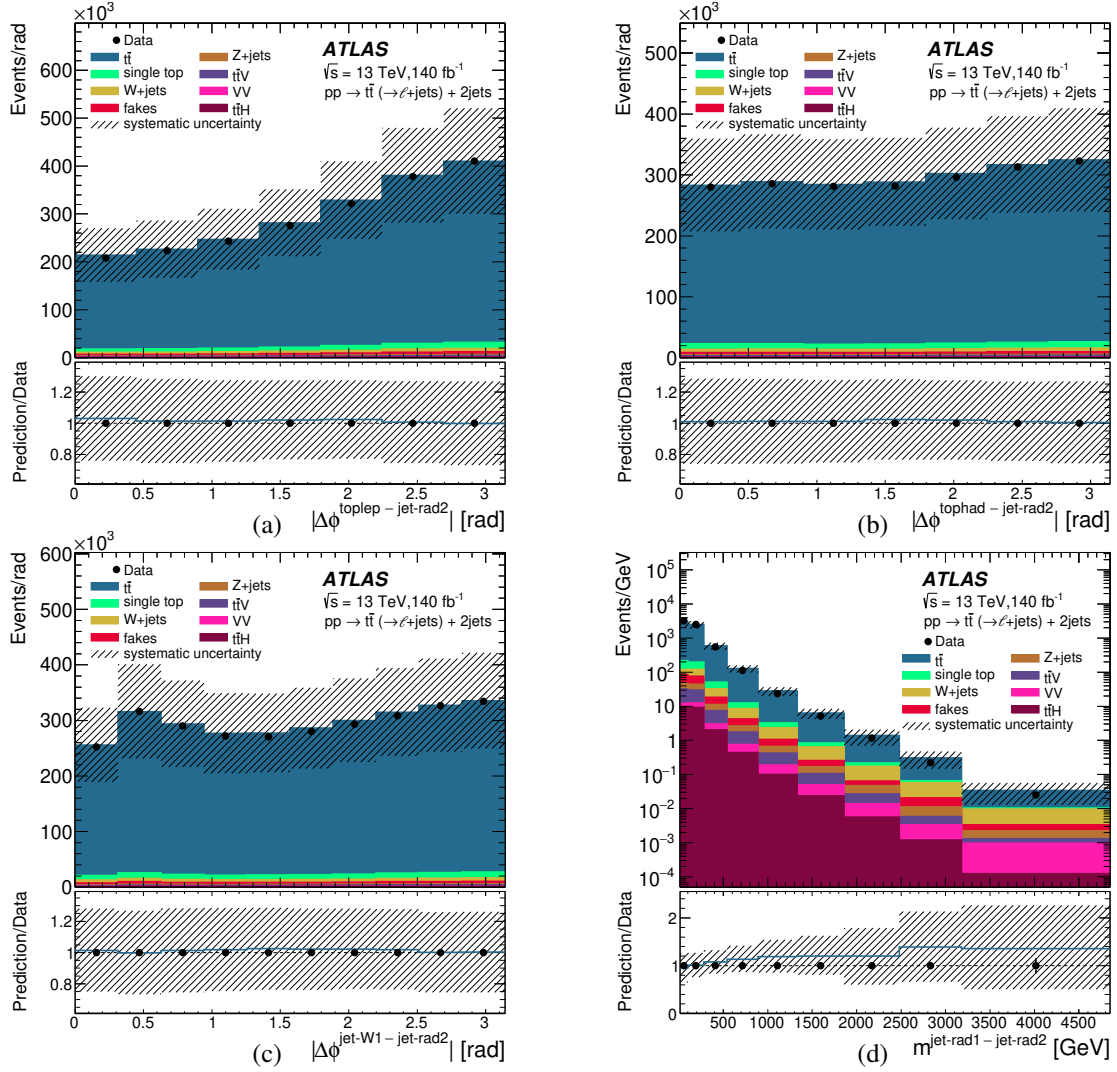


Figure 4: The measured (a) $|\Delta\phi^{\text{toplep} - \text{jet-rad}2}|$, (b) $|\Delta\phi^{\text{tophad} - \text{jet-rad}2}|$, (c) $|\Delta\phi^{\text{jet-W1} - \text{jet-rad}2}|$ and (d) $m^{\text{jet-rad}1 - \text{jet-rad}2}$ distributions divided by the bin width (dots) in the $t\bar{t}+2\text{jets}$ channel. The error bars represent the statistical uncertainty in the data; for many points, the uncertainty is smaller than the marker size and, thus, not visible. The hatched bands represent the systematic uncertainties (see Section 10). The prediction of the signal and various backgrounds (histograms) are also included. The lower panels of each figure show the ratio of the total prediction and the data distributions.

9 Cross-section measurement

Differential cross-sections are measured at particle level as functions of the observables defined in Section 8 for the three channels separately. The data distributions, after background subtraction (see Section 6), are unfolded to the particle level as explained below.

9.1 Unfolding method

The Bayesian unfolding [103] method as implemented in RooUnfold [104] is used to obtain the measured differential cross-sections. In this method, repeated applications of the Bayes' theorem are used to invert the unfolding matrix. The regularisation parameter is the number of iterations (N_{iter}), therefore regularisation is achieved by stopping the iterative procedure at a given value of N_{iter} . The results are found to be fairly insensitive to N_{iter} for most of the phase space measured; two iterations, i.e. $N_{\text{iter}} = 2$, are used. Uncertainties related to this choice of number of iterations are considered (see Sections 9.2 and 10).

The differential cross-section as a function of the observable X in bin i is computed using the equation

$$\frac{d\sigma}{dX_i} \equiv \frac{1}{\mathcal{L} \cdot \Delta X_i} \cdot N_i^{\text{unf}},$$

where the index i iterates over bins of observable X , ΔX is the bin width, \mathcal{L} is the integrated luminosity and N^{unf} represents the unfolded data value in each bin (overflow and underflow events are not considered when evaluating N^{unf}). It is calculated as

$$N_i^{\text{unf}} \equiv \frac{1}{\epsilon^i} \cdot \sum_j f_{\text{match}}^j \cdot \mathcal{M}_{ij}^{-1} \cdot f_{\text{acc}}^j \cdot (N_{\text{data}}^j - N_{\text{bkg}}^j),$$

where N_{data} (N_{bkg}) is the number of data (background) events in each bin of observable X . The acceptance fraction f_{acc} is defined as

$$f_{\text{acc}}^j = \frac{N_{\text{particle} \wedge \text{detector}}^j}{N_{\text{detector}}^j},$$

where $N_{\text{particle} \wedge \text{detector}}$ is the number of detector-level signal MC events that satisfy the particle-level selection in each bin; this factor corrects for events that are generated outside the fiducial phase-space but satisfy the detector-level selection. The unfolding matrix \mathcal{M} is constructed from the correlation matrix, which maps the generated particle-level signal MC events to the detector-level events in their overlap region. Thus, the probability for particle-level events to be reconstructed in the same bin is represented by the diagonal elements, and the off-diagonal elements describe the fraction of particle-level events that migrate into other bins. To suppress combinatorial background in \mathcal{M} , angular matching requirements are applied to the reconstructed objects. For all events, the reconstructed top quarks are required to satisfy $\Delta R(\text{top-}x_{\text{part}}, \text{top-}x_{\text{det}}) < 0.8$, where top- x represents the leptonically or hadronically decaying top quark. In the $t\bar{t}$ inclusive channel, matching of the jets is performed by requiring $\Delta R(\text{jet-}y_{\text{part}}, \text{jet-}y_{\text{det}}) < 0.3$, where jet- y represents jet-W1, jet-W2. In the $t\bar{t}+1\text{jet}$ and $t\bar{t}+2\text{jets}$ channels, this requirement is applied to jet-rad1, jet-rad2 or both, where necessary. In addition, the reconstructed objects (top quarks or jets) that are not matched to a generated object as well as reconstruction inefficiencies (generated objects that are not

matched to a reconstructed object) are taken into account in the Bayesian method. In addition, the inclusion of a matching scheme ensures the stability of the iterative process, so that the results are insensitive to N_{iter} , except for statistical fluctuations, as mentioned above. The effect of the matching procedure in the unfolding is accounted for by the matching fraction f_{match} , which is defined as

$$f_{\text{match}}^j = \frac{N_{\text{particle} \wedge \text{detector} \wedge \text{match}}^j}{N_{\text{particle} \wedge \text{detector}}^j},$$

where $N_{\text{particle} \wedge \text{detector} \wedge \text{match}}$ is the number of signal MC detector-level events that satisfy the particle-level selection and matching requirements and $N_{\text{particle} \wedge \text{detector}}$ is the number of particle-level events that satisfy the detector-level selection without the matching requirements. Finally, the efficiency ε is defined as

$$\varepsilon^i = \frac{N_{\text{particle} \wedge \text{detector}}^i}{N_{\text{particle}}^i},$$

where N_{particle} is the number of signal MC events at particle level in each bin; this factor corrects for events that satisfy the particle-level selection but are not selected at the detector level.

As examples, Figure 5 shows ε , f_{match} and f_{acc} for $p_{\text{T}}^{\text{jet-W1}}$, $|y^{\text{jet-W1}}|$ and $|\Delta\phi^{\text{tolep-jet-rad1}}|$ and the unfolding matrices for the same observables. The signal samples of PwG+PY8 are used in this figure.

The normalised differential cross-sections are measured by dividing the differential cross-sections by the total cross-section in the region of phase space considered for each channel.

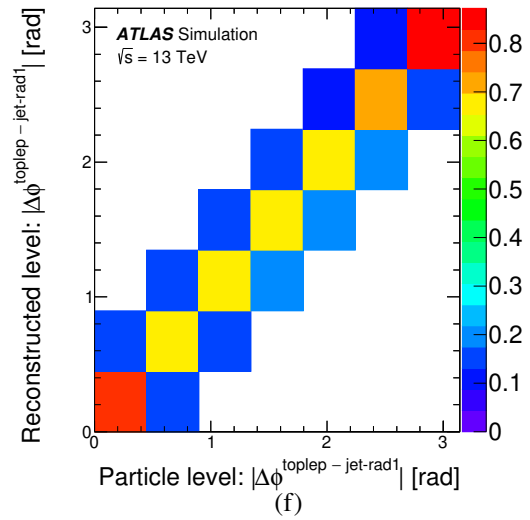
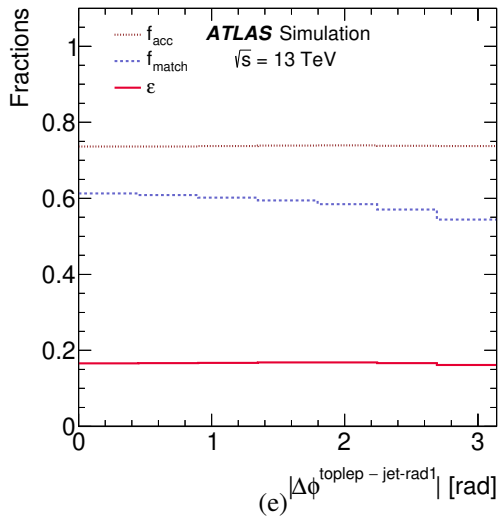
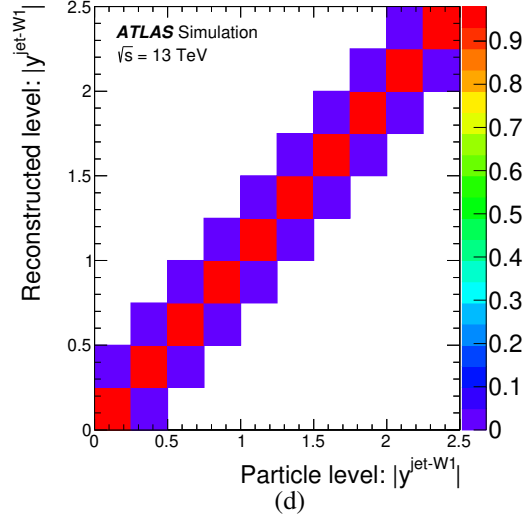
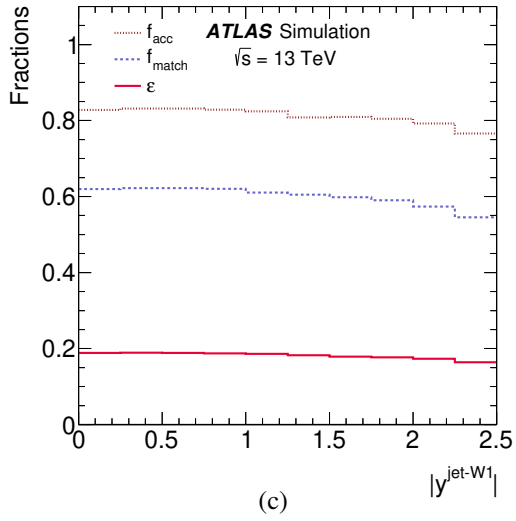
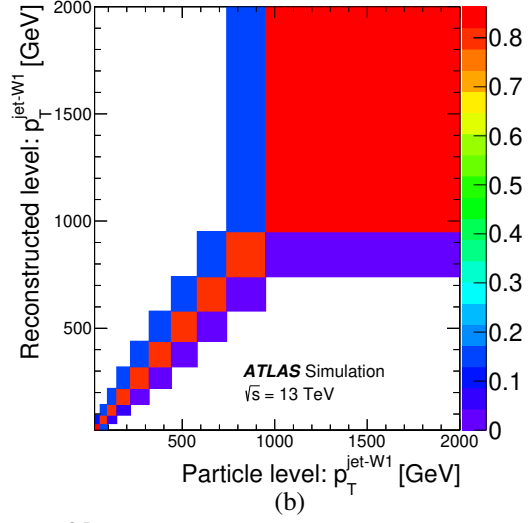
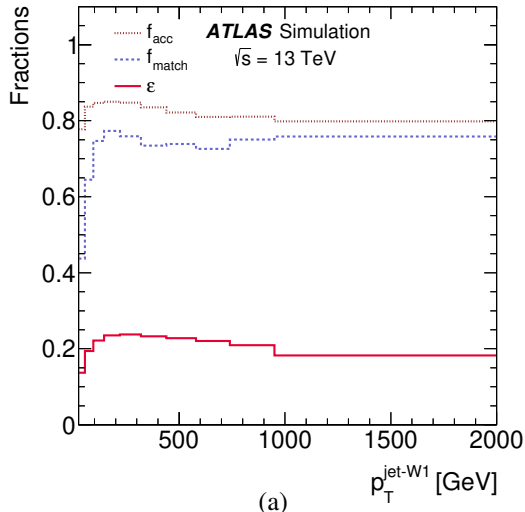


Figure 5: The efficiency ε (solid lines), matching fraction f_{match} (dashed lines) and acceptance fraction f_{acc} (dotted lines) for (a) $p_T^{\text{jet-W1}}$, (c) $|y^{\text{jet-W1}}|$ and (e) $|\Delta\phi^{\text{toplep-jet-rad1}}|$. The unfolding matrix M_{ij} for (b) $p_T^{\text{jet-W1}}$, (d) $|y^{\text{jet-W1}}|$ and (f) $|\Delta\phi^{\text{toplep-jet-rad1}}|$; the distributions are normalised such that the sum of the entries in each column is equal to unity. The signal samples of PWG+PY8 are used.

9.2 Closure and stress tests

The unfolding procedure is checked by performing several ‘closure’ and stress tests, which validate the consistency of the procedure.

The first closure test is a cross-check of the reconstruction-generation level matching procedure: the cross-sections are unfolded with (as in the nominal cross-sections) and without matching in the transfer matrices. The ratio of these two cross-sections is calculated; the ratios are typically consistent with unity within 1%. Thus, it is verified that the matching procedure does not affect the unfolding.

A second closure test is performed to check that the unfolding procedure recovers the generated result in a statistically independent sample. For this test, a MC signal sample is divided into two subsamples A and B; sample A is used as pseudo-data and unfolded to particle level using sample B (pseudo-data cross-section). The pseudo-data cross-sections are compared with the generated results of sample A, B or A+B; the differences observed in these comparisons are typically less than 1%. Therefore, the generated result is recovered in a statistically independent sample.

A first stress test is performed by weighting the nominal MC signal sample so that it matches the data distributions after background subtraction at reconstruction level. This weighted MC sample is used to unfold the data (weighted cross-sections); the ratios of the weighted and nominal cross-sections are typically consistent with unity within 1%. The differences observed in this test are considered as a non-closure systematic uncertainty (see Section 10).

A second stress test is performed by using the weighted MC sample as pseudo-data and unfolding it with the nominal MC sample (weighted pseudo-data cross-section); the ratio of the weighted pseudo-data cross-section and the generated result gives back, as expected, the input fitting function for each observable. Therefore, it is concluded that differences between data and MC at reconstruction level do not affect the unfolded measured cross-sections.

A third stress test is performed to ascertain the level of recoverability of the signal for the possible presence of new physics in the data. The existence of a $t\bar{t}$ resonance is hypothesised using a Gaussian distribution introduced at particle level and propagated to the reconstruction level using a weighting procedure (stressed pseudo-data). To determine whether the observables studied are sensitive to this hypothetical resonance and whether the unfolding procedure is able to recover the stressed shape and normalisation, the stressed pseudo-data is unfolded using the nominal MC sample and compared with the stressed generated result. The ratio of these cross-sections shows that the shape and normalisation of the effects due to the resonance are recovered for all observables.

10 Systematic uncertainties

The sources of systematic uncertainties that affect the measurements of the differential cross-sections include the b -tagging calibration and efficiency, the detector energy scale and resolution, the reconstruction efficiency, the background and signal modelling, the statistics of the MC samples and the uncertainty arising from the non-closure. Each source of uncertainty is separated into independent contributions and evaluated by varying the background and the signal MC samples in a correlated way, where necessary. The varied background samples are used to subtract the background and the varied signal samples are used to unfold the background-subtracted data distributions, as explained in Section 9. Systematic uncertainties are evaluated relative to the nominal measured cross-sections separately for the upward and downward

variations (or in the case of a single variation by symmetrising the single deviation) for each bin of each observable. For the normalised cross-sections, each contribution to the systematic uncertainty is assumed to be fully correlated between the differential cross-section in a given bin and the integrated cross-section. Each source of systematic uncertainty is discussed separately in the following.

***b*-tagging calibration and efficiency.** The uncertainties in the *b*-tagging calibration and efficiency are determined separately for *b*-jets, *c*-jets and light-flavour-jets [105–107] using a component breakdown with 19 independent contributions. They depend on the p_T for *b*- and *c*-jets, and on the p_T and η for light-flavour jets, and they account for differences between data and simulation. The dominant contribution arises from the *b*-quark eigenvectors and amounts to typically 3% for the absolute cross-sections and decreases to typically below 0.5% for the normalised cross-sections.

Detector energy scale and resolution. The jet energy scale (JES) is calibrated using a combination of test beam data, simulation and in situ techniques [97]. Its uncertainty is decomposed into a set of 30 uncorrelated components, with contributions from pile-up, jet flavour composition and response, single-particle response, and effects of jets not contained within the calorimeter. The uncertainty in the jet energy resolution (JER) is represented by eight components accounting for jet- p_T and η -dependent differences between simulation and data [97]. The uncertainty in E_T^{miss} due to a possible miscalibration of its soft-track component is derived from data and simulation comparisons of the p_T balance between the hard and the soft E_T^{miss} components [99]. To account for the difference in pile-up distributions between the simulation and data, the pile-up profile in the simulation is corrected to match the one in the data. The uncertainty associated with the correction factor is applied. The uncertainty in the electron [108] and muon [109] energy scale and resolution is also included. The resulting 49 up and down independent contributions are added in quadrature and the dominant contribution comes from the effect of the pile-up on the JES. This uncertainty is typically in the range of 3% to 10%, depending on the observable, for the absolute cross-sections and decreases to the range of 0.3% to 9% for the normalised cross-sections.

Reconstruction efficiency. Reconstruction, identification, isolation and trigger performance for electrons and muons differ between data and simulations. Scale factors are applied to simulated events to correct for these differences. These scale factors are assessed using $Z \rightarrow \ell^+\ell^-$ events in simulation and data with methods similar to those described in Refs. [91, 110]. The associated systematic uncertainties are propagated to the measured cross-sections. The JVT requirement and pile-up systematic uncertainties are also included. The resulting 16 up and down independent contributions are added in quadrature and the dominant contribution comes from the JVT contribution. This uncertainty is in the range of 0.5% to 2% for both the absolute and normalised cross-sections.

Background modelling. The uncertainties in the modelling of the background are estimated by changing the normalisation of the MC samples according to the uncertainty in the predicted cross-section used for the normalisation of these samples (see Table 1). For the *W*+jets, *Z*+jets and fakes background, an uncertainty of 50% is included for the normalisation. This value for the uncertainty in the normalisation covers the differences observed between data and simulations in control regions with exactly three jets and at most one *b*-tagged jet or at least four jets and at most one *b*-tagged jet; these control regions are away from the signal region and enriched in these background processes. In addition, for the single-top-quark background, since the *tW* contribution is the largest among the three single-top-quark production channels, the uncertainty arising from the method used to handle the interference between *tW* and $t\bar{t}$ production is determined by comparing the *tW* simulated sample that uses the DS method with the nominal one based on the DR technique. The resulting uncertainties are symmetrised and added in quadrature. This uncertainty is typically in the range of 1.5% to 15%, depending on the observable, for the absolute cross-sections and decreases to the range of 0.1% to 10% for the normalised cross-sections.

Signal modelling. The uncertainties that affect the signal modelling and the method of estimation are discussed below. The effects of the PS and hadronisation models are estimated by unfolding the data after background subtraction using the PwG+Hw7 sample and calculating the difference relative to the nominal cross-section (typically $< 2\%$). Since the single-top-quark processes are the dominant background, PwG+Hw7 samples are also used to model these processes when estimating this uncertainty. The impact of the matching procedure between the ME calculation and the PS model is evaluated using the aMC@NLO+Hw7 sample to unfold the data after background subtraction and calculating the difference relative to the cross-section unfolded using the PwG+Hw7 samples, both for signal and single-top-quark background (typically $\approx 1\%$). The uncertainties affecting the description of the hard gluon radiation are evaluated by unfolding the data after background subtraction using the PwG+PY8 h_{damp} sample and calculating the difference relative to the nominal cross-section (typically $< 0.5\%$). The effect of the assumed value of m_t (172.5 GeV) is estimated using samples of PwG+PY8 generated with $m_t = 169$ GeV or $m_t = 176$ GeV to unfold the data after background subtraction and calculating the difference relative to the nominal cross-section; the value of the uncertainty obtained in this way is then scaled by 1/3.5, to account for the current uncertainty in m_t (1 GeV) and amounts to typically $< 0.3\%$. The first three contributions listed above are symmetrised. The dominant contribution arises from the PS and hadronisation models. The resulting uncertainty is typically in the range of 0.5% to 10%, depending on the observable, for the absolute cross-sections and decreases to the range of 0.2% to 8% for the normalised cross-sections. The theoretical uncertainties that affect the unfolding procedure and the method of estimate are discussed below. These uncertainties affect the $t\bar{t}$ signal and the single-top-quark background samples and are taken as correlated between the two MC samples. The uncertainty due to missing higher-order QCD corrections in the ME computation is estimated by independently varying μ_R and μ_F by factors of 2 and 0.5 relative to the central value (typically $< 1\%$). The uncertainties in the amount of initial- and final-state radiation from the PS are assessed by varying the corresponding parameter of the A14 PS tune (Var3c) [55] (typically $< 0.5\%$) and by varying the scale μ_R^{FSR} by factors of 2 and 0.5 (typically $\approx 2\%$). The uncertainties due to the PDFs are estimated following the PDF4LHC prescription [75] (typically $< 0.5\%$). The dominant contribution to the systematic uncertainty arising from the theoretical uncertainties in the unfolding comes from the variation of the μ_R^{FSR} scale. The resulting uncertainty is typically in the range of 1% to 5%, depending on the observable, for the absolute cross-sections and decreases to the range of 0.5% to 4% for the normalised cross-sections.

Non-closure. As explained in Section 9.2, the differences observed in the stress test are considered as a non-closure systematic uncertainty. This uncertainty is typically below 0.5%.

10.1 Total systematic uncertainty

The total systematic uncertainty is computed by adding in quadrature the sources of uncertainty listed in the previous section. Figures 6 to 9 (10 to 13) show the resulting total systematic uncertainty, together with the contribution from each source, the statistical uncertainty in the MC samples and the statistical uncertainty in the data for the absolute (normalised) cross-sections. The statistical uncertainties in data and MC samples are evaluated using ‘pseudo-data experiments’ (bootstrap technique) with 1000 statistically independent replicas. In the figures, the systematic contributions are stacked, except for the statistical uncertainty in the data. In addition, there is an uncertainty from the combined 2015–2018 integrated luminosity, which amounts to 0.83% [42] (not included in the figures).

In the case of the angular observables, for the $t\bar{t}$ inclusive channel, the total relative systematic uncertainty is $\approx 7\%$ and dominated by the b -tagging calibration uncertainty. In the case of the $t\bar{t}+1\text{jet}$ channel, the

total relative systematic uncertainty amounts to $\approx 10\%$ and is dominated by the detector energy scale and resolution. The $t\bar{t}+2\text{jets}$ channel has a total relative systematic uncertainty of $\approx 13\%$ and is also dominated by the detector energy scale and resolution. For the normalised cross-sections, the total relative systematic uncertainties are $\approx 1\%$, $\approx 1.5\%$ and $\approx 2\%$ for the $t\bar{t}$ inclusive, $t\bar{t}+1\text{jet}$ and $t\bar{t}+2\text{jets}$ channels, respectively.

In the case of the transverse momentum and invariant-mass observables, the values for the uncertainties quoted above are only valid at low p_T or invariant mass. The total relative systematic uncertainty in the absolute (normalised) cross-sections increases up to $\approx 38\%$ ($\approx 37\%$) for $p_T^{\text{jet-W}1}$, $\approx 38\%$ ($\approx 37\%$) for $p_T^{\text{jet-W}2}$, $\approx 57\%$ ($\approx 55\%$) for $p_T^{\text{jet-rad}1}$, $\approx 77\%$ ($\approx 74\%$) for $m^{t\bar{t}-\text{jet-rad}1}$, $\approx 50\%$ ($\approx 52\%$) for $p_T^{\text{jet-rad}2}$ and $\approx 48\%$ ($\approx 46\%$) for $m^{\text{jet-rad}1-\text{jet-rad}2}$ in the last bins of these distributions. In these regions of phase space, the background modelling and statistical uncertainties dominate.

The statistical uncertainty in the data is below 0.3% for the angular observables in the $t\bar{t}$ inclusive channel; in the tails of the $p_T^{\text{jet-W}1}$ and $p_T^{\text{jet-W}2}$ cross-sections, it increases up to 17% and 19% , respectively. For the $t\bar{t}+1\text{jet}$ channel, the statistical uncertainty in the data is $\approx 0.3\%$ for the angular observables and increases up to 36% and 23% in the last bins of the $p_T^{\text{jet-rad}1}$ and $m^{t\bar{t}-\text{jet-rad}1}$ cross-sections, respectively. In the $t\bar{t}+2\text{jets}$ channel, the statistical uncertainty in the data is $\approx 0.4\%$ for the angular observables and increases up to 19% and 28% in the last bins of the $p_T^{\text{jet-rad}2}$ and $m^{\text{jet-rad}1-\text{jet-rad}2}$ cross-sections, respectively.

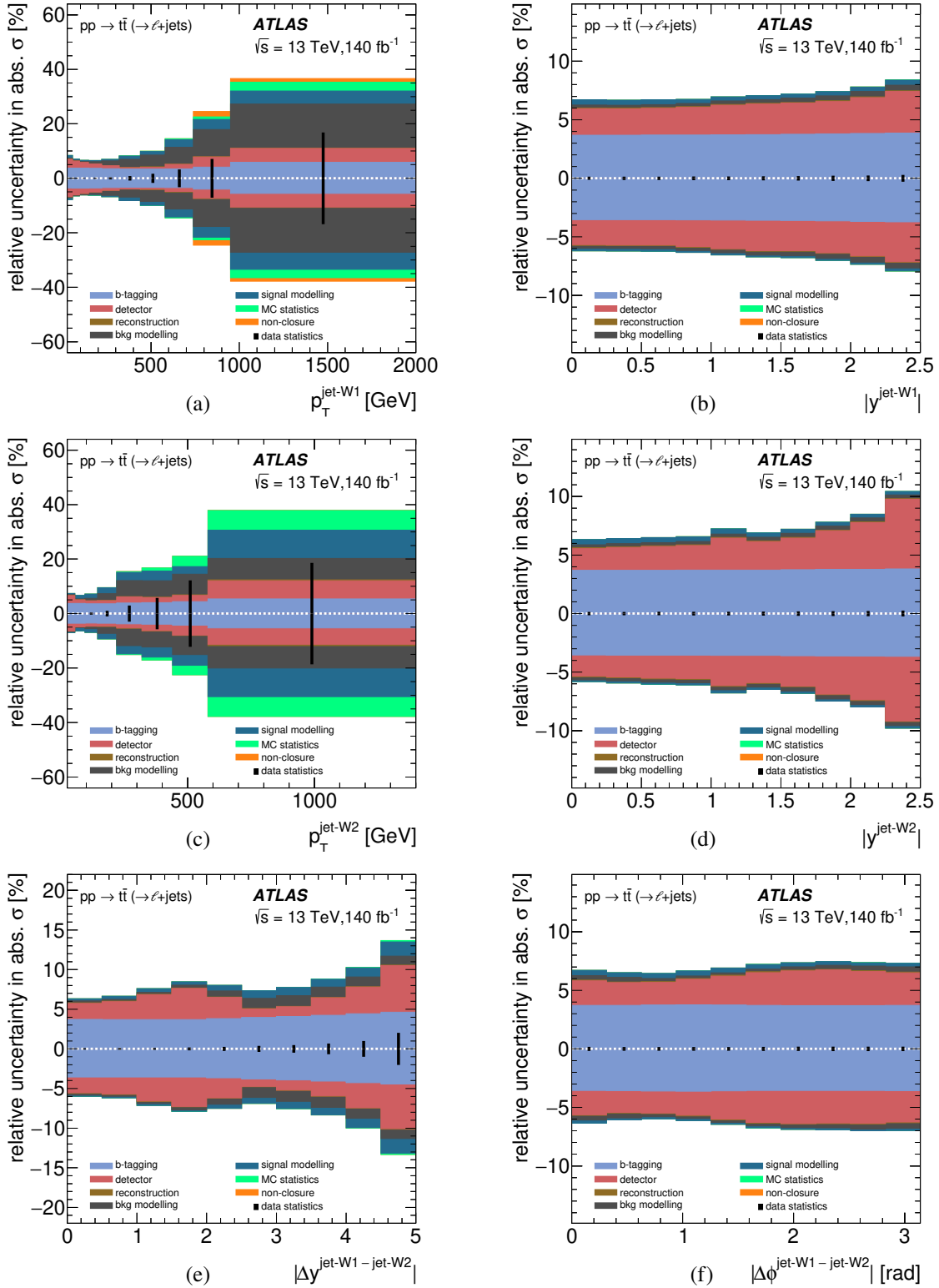


Figure 6: Total relative systematic uncertainties in the measured cross-sections in percentages for (a) $p_T^{\text{jet-W1}}$, (b) $|y^{\text{jet-W1}}|$, (c) $p_T^{\text{jet-W2}}$, (d) $|y^{\text{jet-W2}}|$, (e) $|\Delta y^{\text{jet-W1-jet-W2}}|$ and (f) $|\Delta\phi^{\text{jet-W1-jet-W2}}|$ in the $t\bar{t}$ inclusive channel. The individual sources of systematic uncertainty (plotted in stacked form) and the statistical uncertainty in the data are also included.

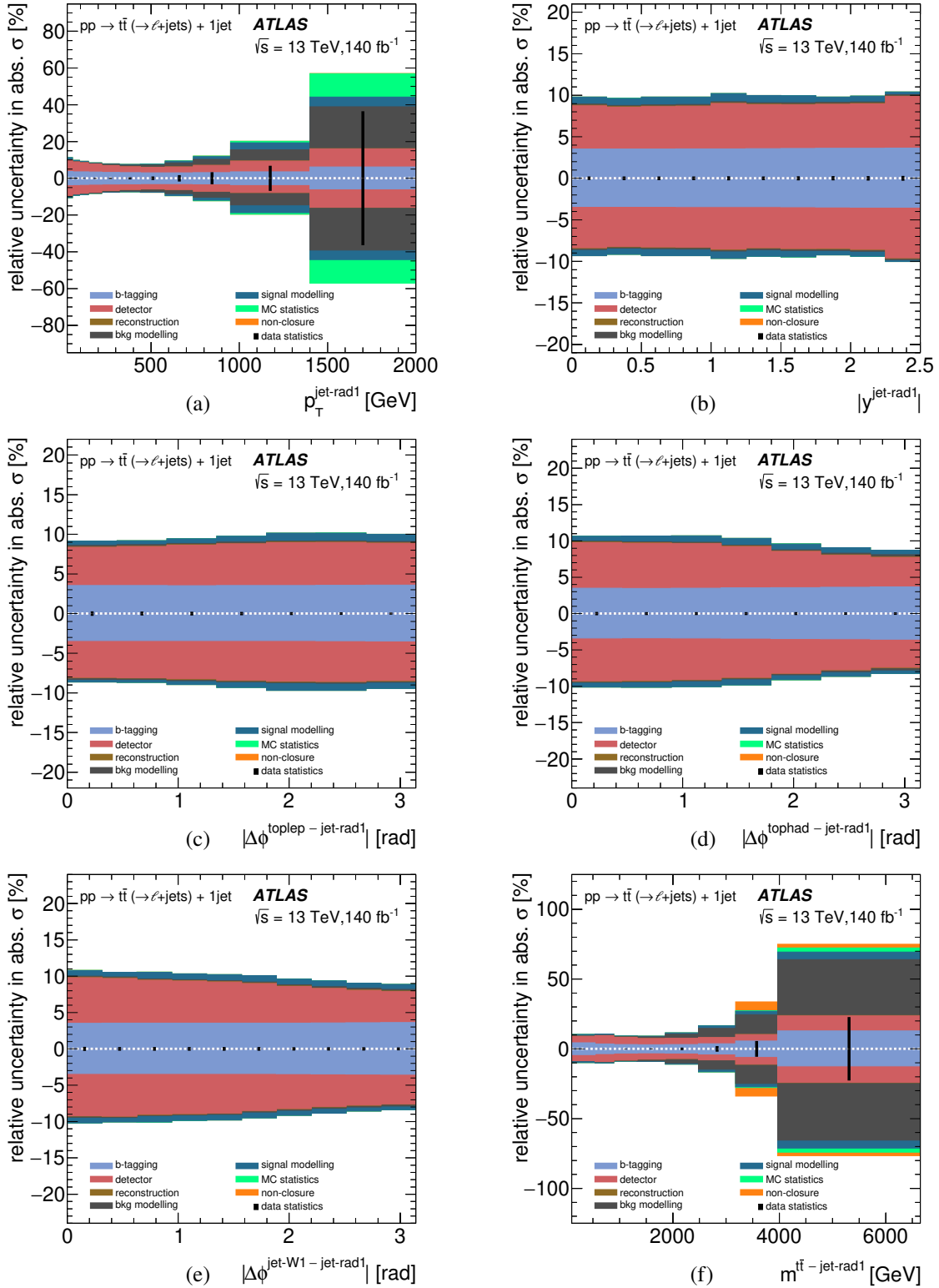


Figure 7: Total relative systematic uncertainties in the measured cross-sections in percentages for (a) $p_T^{\text{jet-rad1}}$, (b) $|y^{\text{jet-rad1}}|$, (c) $|\Delta\phi^{\text{toplep}} - \text{jet-rad1}|$, (d) $|\Delta\phi^{\text{tophad}} - \text{jet-rad1}|$, (e) $|\Delta\phi^{\text{jet-W1}} - \text{jet-rad1}|$ and (f) $m^{t\bar{t}} - \text{jet-rad1}$ in the $t\bar{t}+1\text{jet}$ channel. The individual sources of systematic uncertainty (plotted in stacked form) and the statistical uncertainty in the data are also included.

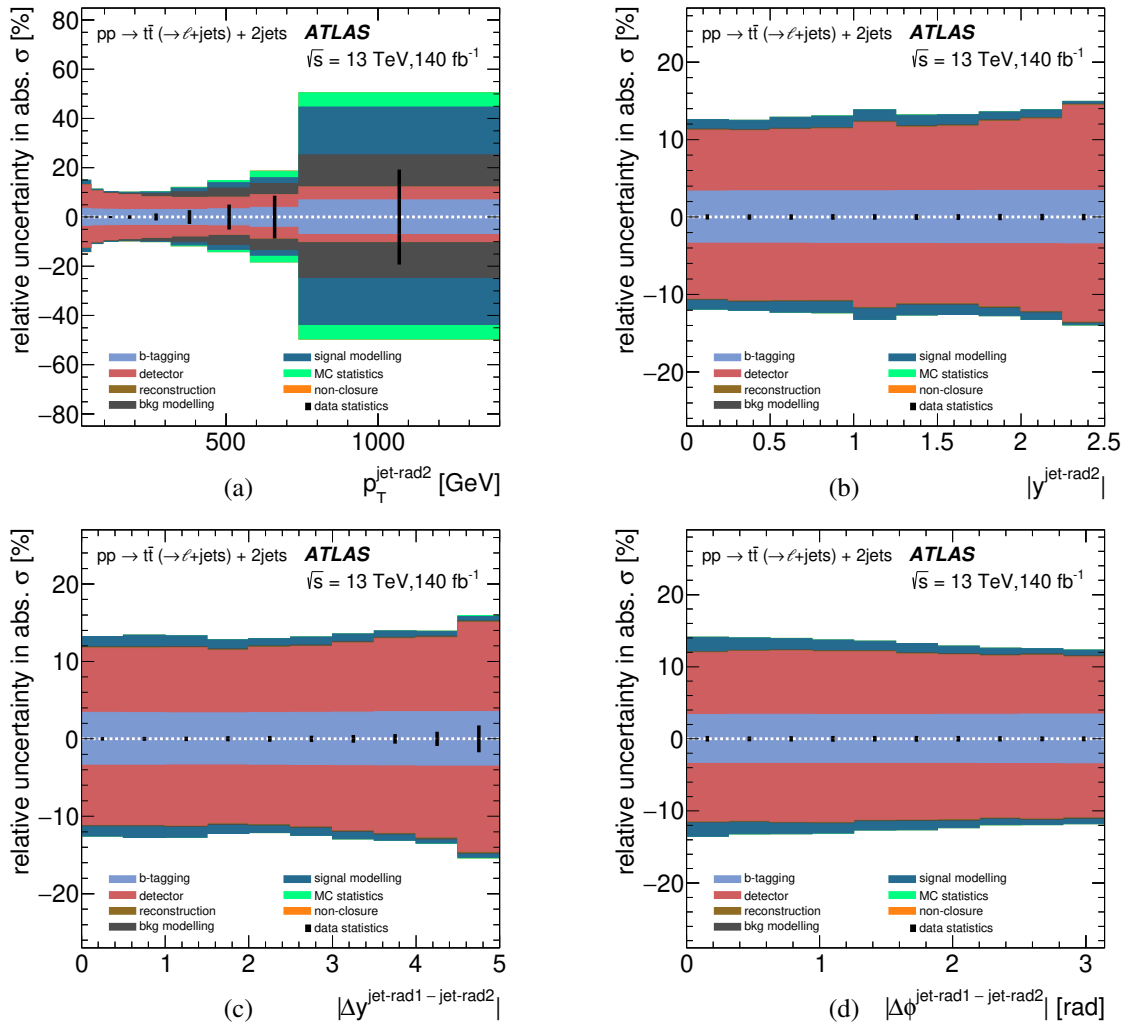


Figure 8: Total relative systematic uncertainties in the measured cross-sections in percentages for (a) $p_T^{\text{jet-rad2}}$, (b) $|y^{\text{jet-rad2}}|$, (c) $|\Delta y^{\text{jet-rad1} - \text{jet-rad2}}|$ and (d) $|\Delta\phi^{\text{jet-rad1} - \text{jet-rad2}}|$ in the $t\bar{t}+2\text{jets}$ channel. The individual sources of systematic uncertainty (plotted in stacked form) and the statistical uncertainty in the data are also included.

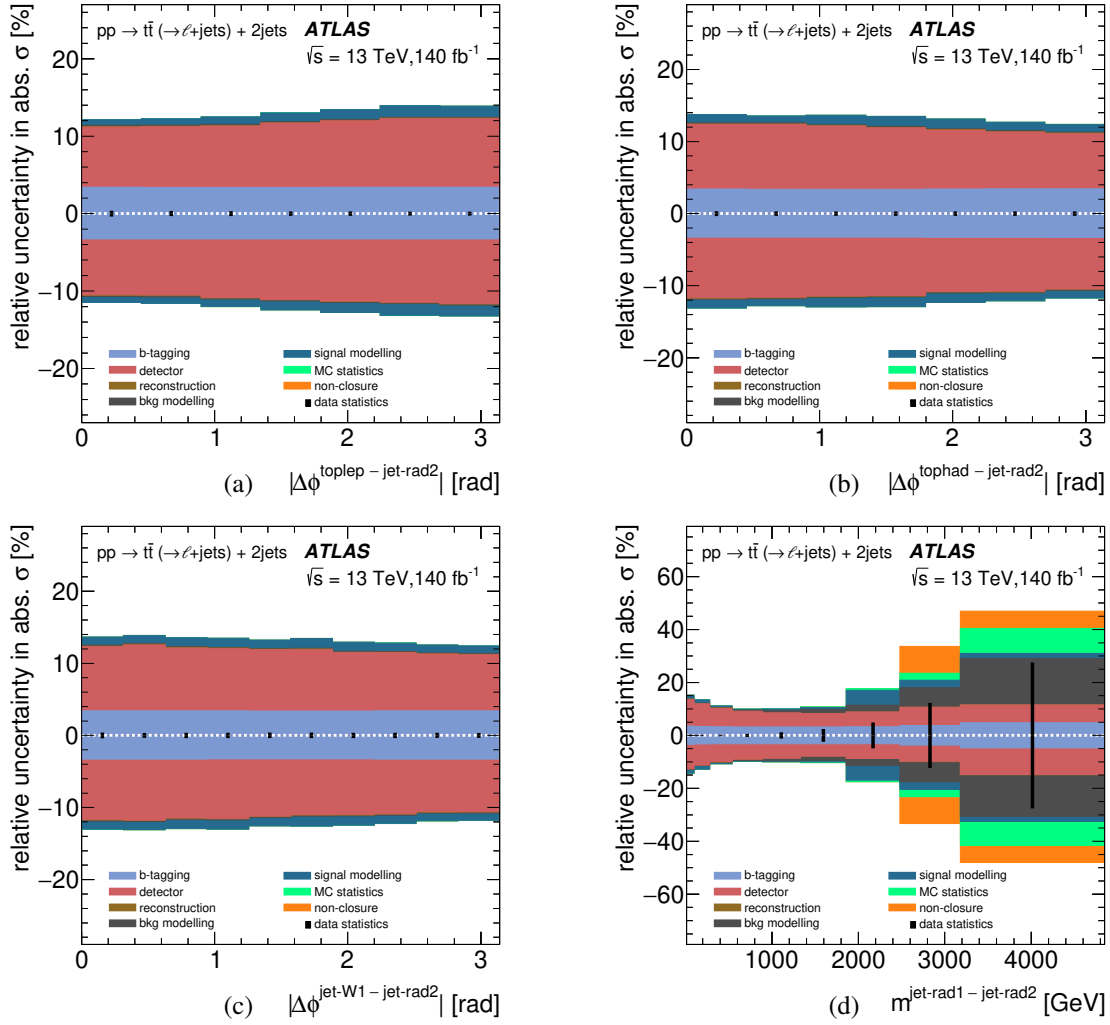


Figure 9: Total relative systematic uncertainties in the measured cross-sections in percentages for (a) $|\Delta\phi^{\text{toplep}} - \text{jet-rad2}|$, (b) $|\Delta\phi^{\text{tophad}} - \text{jet-rad2}|$, (c) $|\Delta\phi^{\text{jet-W1}} - \text{jet-rad2}|$ and (d) $m^{\text{jet-rad1} - \text{jet-rad2}}$ in the $t\bar{t}+2\text{jets}$ channel. The individual sources of systematic uncertainty (plotted in stacked form) and the statistical uncertainty in the data are also included.

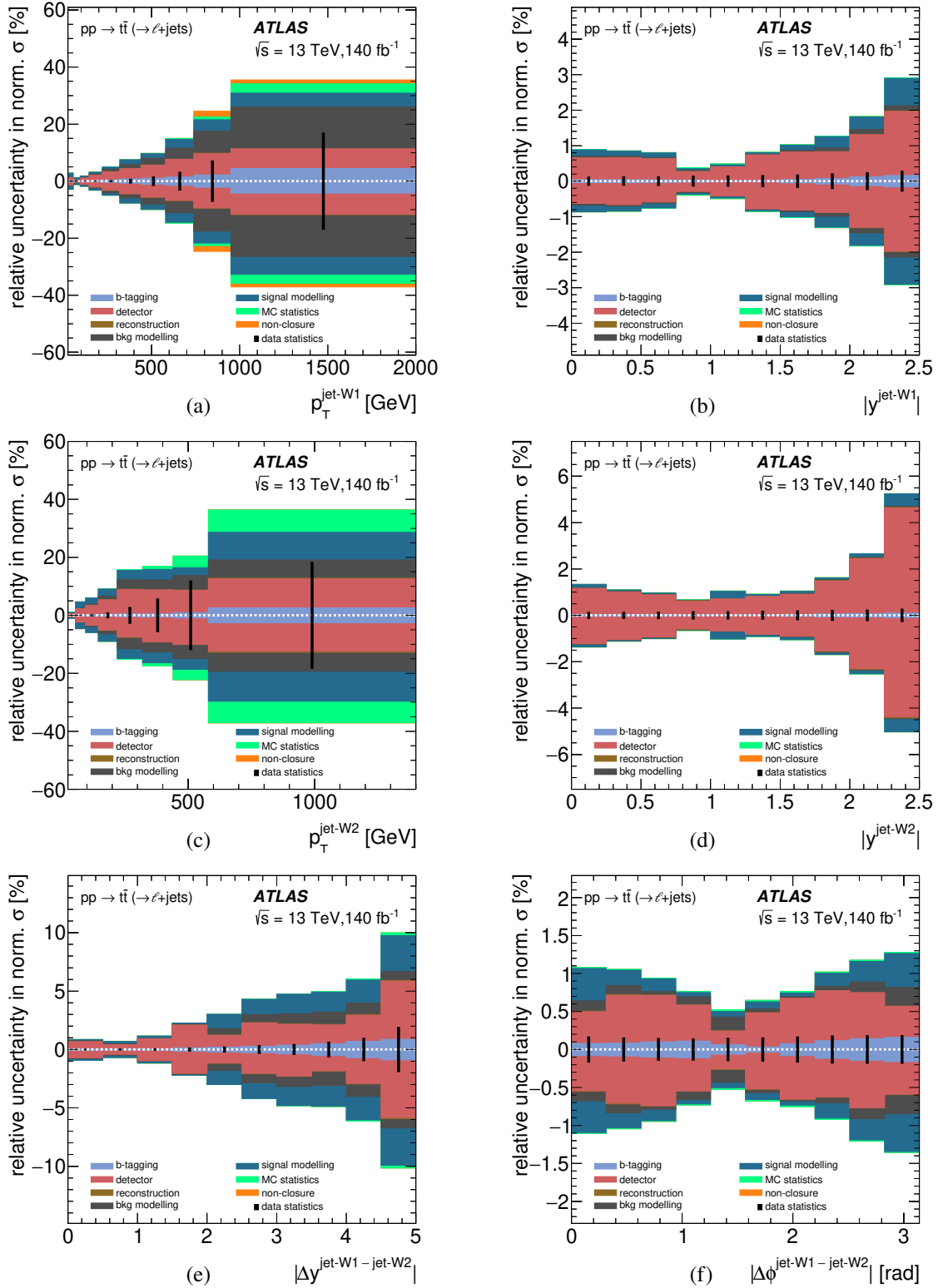


Figure 10: Total relative systematic uncertainties in the measured normalised cross-sections in percentages for (a) $p_T^{\text{jet-W1}}$, (b) $|y^{\text{jet-W1}}|$, (c) $p_T^{\text{jet-W2}}$, (d) $|y^{\text{jet-W2}}|$, (e) $|\Delta y^{\text{jet-W1} - \text{jet-W2}}|$ and (f) $|\Delta\phi^{\text{jet-W1} - \text{jet-W2}}|$ in the $t\bar{t}$ inclusive channel. The individual sources of systematic uncertainty (plotted in stacked form) and the statistical uncertainty in the data are also included.

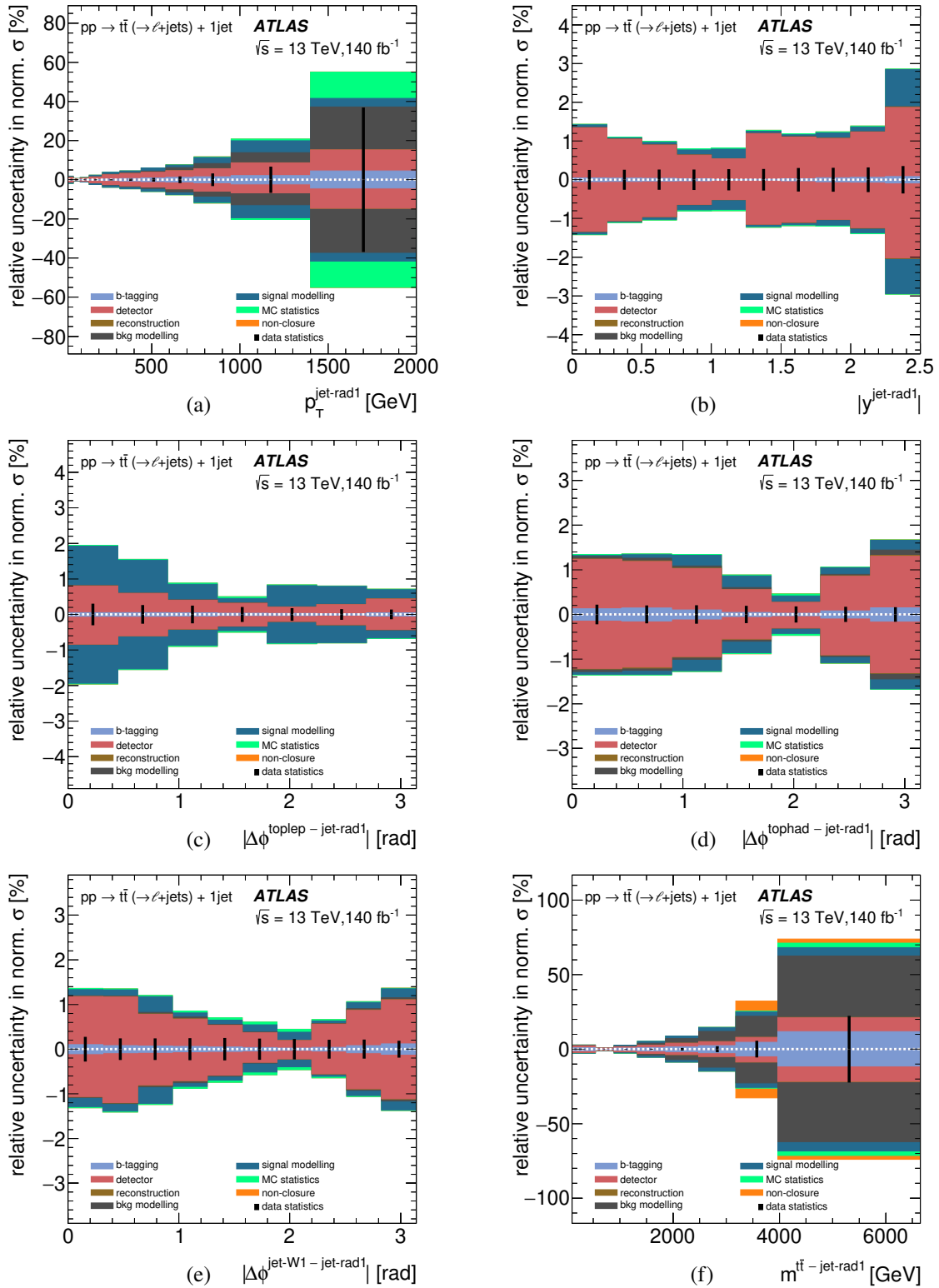


Figure 11: Total relative systematic uncertainties in the measured normalised cross-sections in percentages for (a) $p_T^{\text{jet-rad1}}$, (b) $|y^{\text{jet-rad1}}|$, (c) $|\Delta\phi^{\text{toplep-jet-rad1}}|$, (d) $|\Delta\phi^{\text{tophad-jet-rad1}}|$, (e) $|\Delta\phi^{\text{jet-W1-jet-rad1}}|$ and (f) $m^{t\bar{t}-jet-rad1}$ in the $t\bar{t}+1\text{jet}$ channel. The individual sources of systematic uncertainty (plotted in stacked form) and the statistical uncertainty in the data are also included.

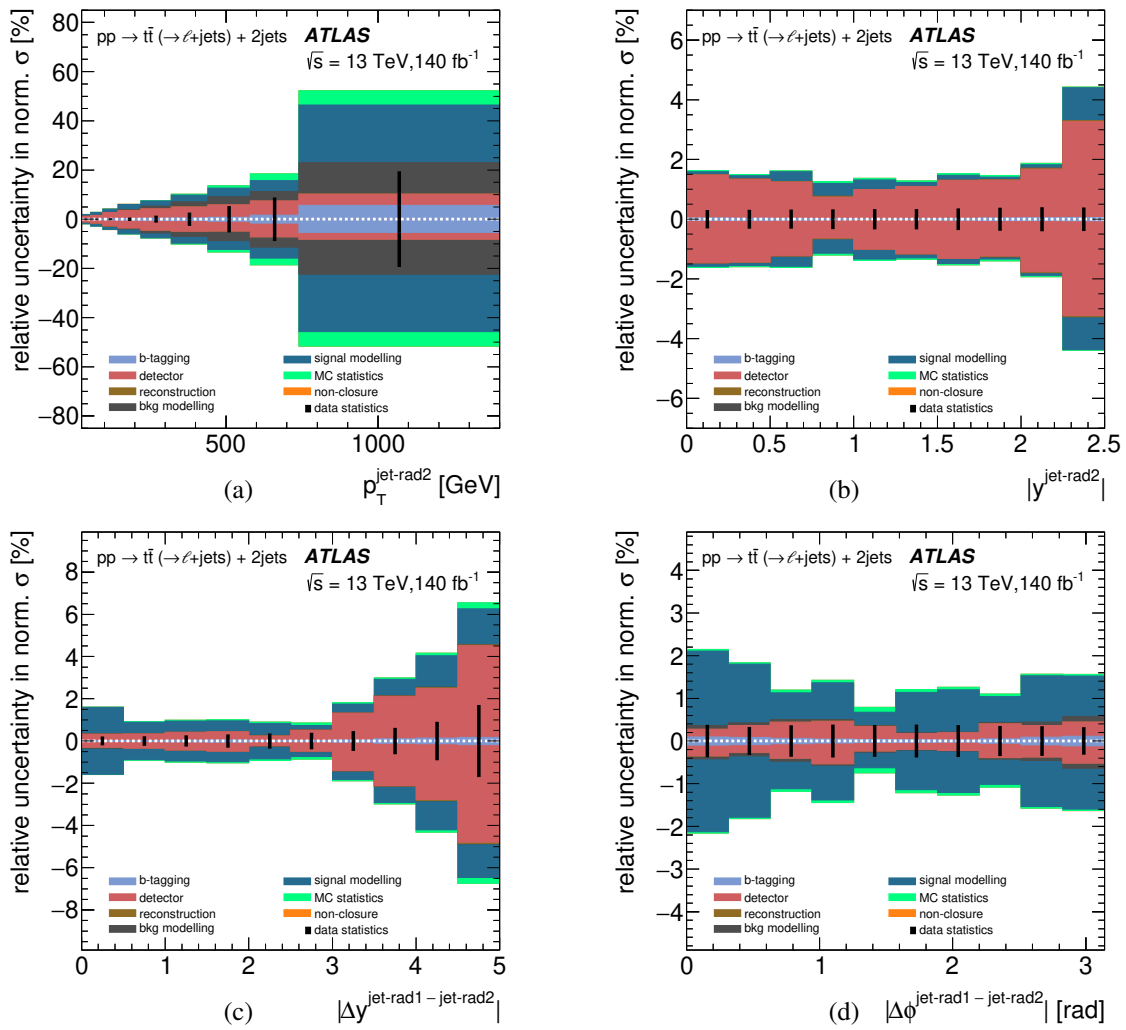


Figure 12: Total relative systematic uncertainties in the measured normalised cross-sections in percentages for (a) $p_T^{\text{jet-rad2}}$, (b) $|y^{\text{jet-rad2}}|$, (c) $|\Delta y^{\text{jet-rad1} - \text{jet-rad2}}|$ and (d) $|\Delta\phi^{\text{jet-rad1} - \text{jet-rad2}}|$ in the $t\bar{t}+2\text{jets}$ channel. The individual sources of systematic uncertainty (plotted in stacked form) and the statistical uncertainty in the data are also included.

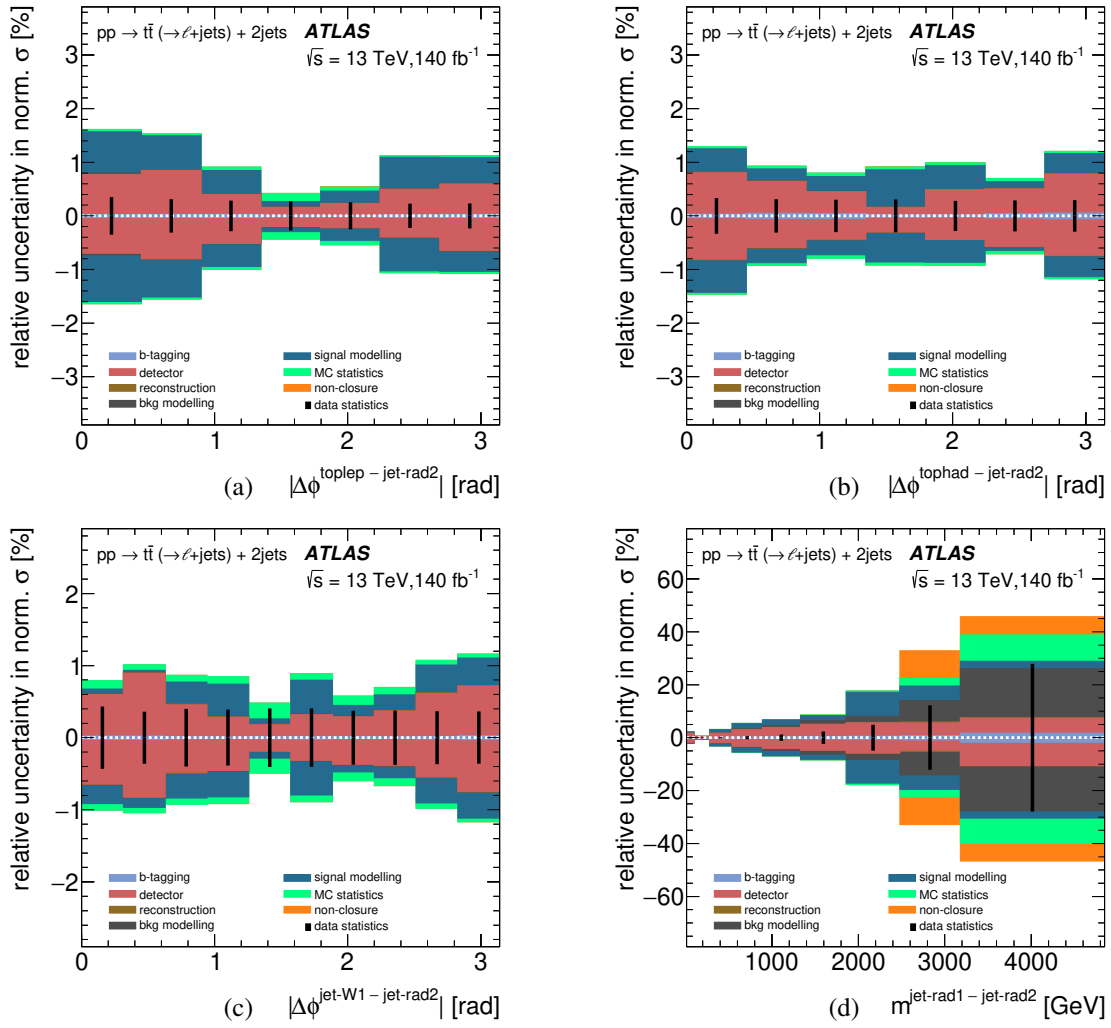


Figure 13: Total relative systematic uncertainties in the measured normalised cross-sections in percentages for (a) $|\Delta\phi^{\text{toplep}} - \text{jet-rad2}|$, (b) $|\Delta\phi^{\text{tophad}} - \text{jet-rad2}|$, (c) $|\Delta\phi^{\text{jet-W1}} - \text{jet-rad2}|$ and (d) $m^{\text{jet-rad1}} - \text{jet-rad2}$ in the $t\bar{t} + 2\text{jets}$ channel. The individual sources of systematic uncertainty (plotted in stacked form) and the statistical uncertainty in the data are also included.

11 Results

The measured absolute and normalised differential cross-sections for $t\bar{t}$ production at particle level in the $t\bar{t}$ inclusive, the $t\bar{t}+1\text{jet}$ and the $t\bar{t}+2\text{jets}$ channels are presented in Sections 11.1, 11.2 and 11.3, respectively. Next-to-leading-order QCD predictions from PwG+PY8, PwG+Hw7, aMC@NLO+Hw7 and SHERPA 2.2.12 and NNLO QCD predictions from PwG+PY8 MiNNLOPS are compared with the measurements. The level of agreement between the measured differential cross-section as a function of each observable and the different theoretical predictions is quantified by the χ^2 and p -values (see Section 11.4).

11.1 Differential cross-sections for the $t\bar{t}$ inclusive channel

Figures 14 and 15 show the absolute and normalised differential $t\bar{t}$ cross-sections in the ℓ +jets decay mode for the $t\bar{t}$ inclusive channel as functions of $p_T^{\text{jet-W1}}$, $|y^{\text{jet-W1}}|$, $p_T^{\text{jet-W2}}$, $|y^{\text{jet-W2}}|$, $|\Delta y^{\text{jet-W1} - \text{jet-W2}}|$ and $|\Delta\phi^{\text{jet-W1} - \text{jet-W2}}|$. Values of $p_T^{\text{jet-W1}}$ and $p_T^{\text{jet-W2}}$ up to ~ 1.5 TeV and ~ 1.1 TeV, respectively, are measured. The measured cross-section as a function of $p_T^{\text{jet-W1}}$ ($p_T^{\text{jet-W2}}$) decreases by more than five (six) orders of magnitude within the measured range. The measured cross-section as function of $p_T^{\text{jet-W1}}$ has a harder spectrum than that of $p_T^{\text{jet-W2}}$, which decreases more rapidly with increasing $p_T^{\text{jet-W2}}$. The measured cross-sections as functions of $|y^{\text{jet-W1}}|$ and $|y^{\text{jet-W2}}|$ decrease as the rapidity increases and have very similar shape and normalisation. The measured cross-section as a function of $|\Delta y^{\text{jet-W1} - \text{jet-W2}}|$ ($|\Delta\phi^{\text{jet-W1} - \text{jet-W2}}|$) exhibits a peak around $|\Delta y^{\text{jet-W1} - \text{jet-W2}}| = 0$ ($|\Delta\phi^{\text{jet-W1} - \text{jet-W2}}| = 1$ rad).

The predictions of PwG+PY8, aMC@NLO+Hw7, PwG+Hw7 and SHERPA 2.2.12 are compared to the measurements in Figure 14. As explained in Section 4.1, these predictions are calculated at NLO, however, the normalisation is performed at $\mathcal{O}(\text{NNLO}+\text{NNLL})$. The $|y^{\text{jet-W1}}|$, $|y^{\text{jet-W2}}|$, $|\Delta y^{\text{jet-W1} - \text{jet-W2}}|$ and $|\Delta\phi^{\text{jet-W1} - \text{jet-W2}}|$ measured cross-sections are well described in shape and normalisation by all the predictions, except for the prediction from aMC@NLO+Hw7 which has a tendency to be above the data for $|\Delta y^{\text{jet-W1} - \text{jet-W2}}| > 2$. The measured cross-section as a function of $p_T^{\text{jet-W1}}$ is described by the predictions of PwG+PY8 and PwG+Hw7 only for $p_T^{\text{jet-W1}} < 500$ GeV, whereas aMC@NLO+Hw7 and SHERPA 2.2.12 provide a good description of the data in the whole measured range. The measured cross-section as a function of $p_T^{\text{jet-W2}}$ is well described by the NLO predictions; the differences between the measurement and the prediction from aMC@NLO+Hw7 are within the theoretical and experimental uncertainties. From the comparison of the normalised differential predictions to the measurements (see Figure 15), the same conclusions are drawn.

The NNLO predictions of PwG+PY8 MiNNLOPS are compared with the measured absolute and normalised differential cross-sections in Figures 16 and 17, respectively. For comparison, the predictions of PwG+PY8 are also included in these figures. For all observables, the theoretical uncertainty in the NNLO calculations is smaller than for the NLO predictions. The angular observables are well described by the NNLO predictions within the experimental and theoretical uncertainties, though there is a tendency for the NNLO predictions to be below the data for $|\Delta y^{\text{jet-W1} - \text{jet-W2}}| > 3$, which is clearly observed in the comparison of the normalised cross-section (Figure 17(e)). For the NNLO prediction, a significant improvement in the description of the shape and normalisation of the measured differential cross-section as a function of $p_T^{\text{jet-W1}}$ is observed.

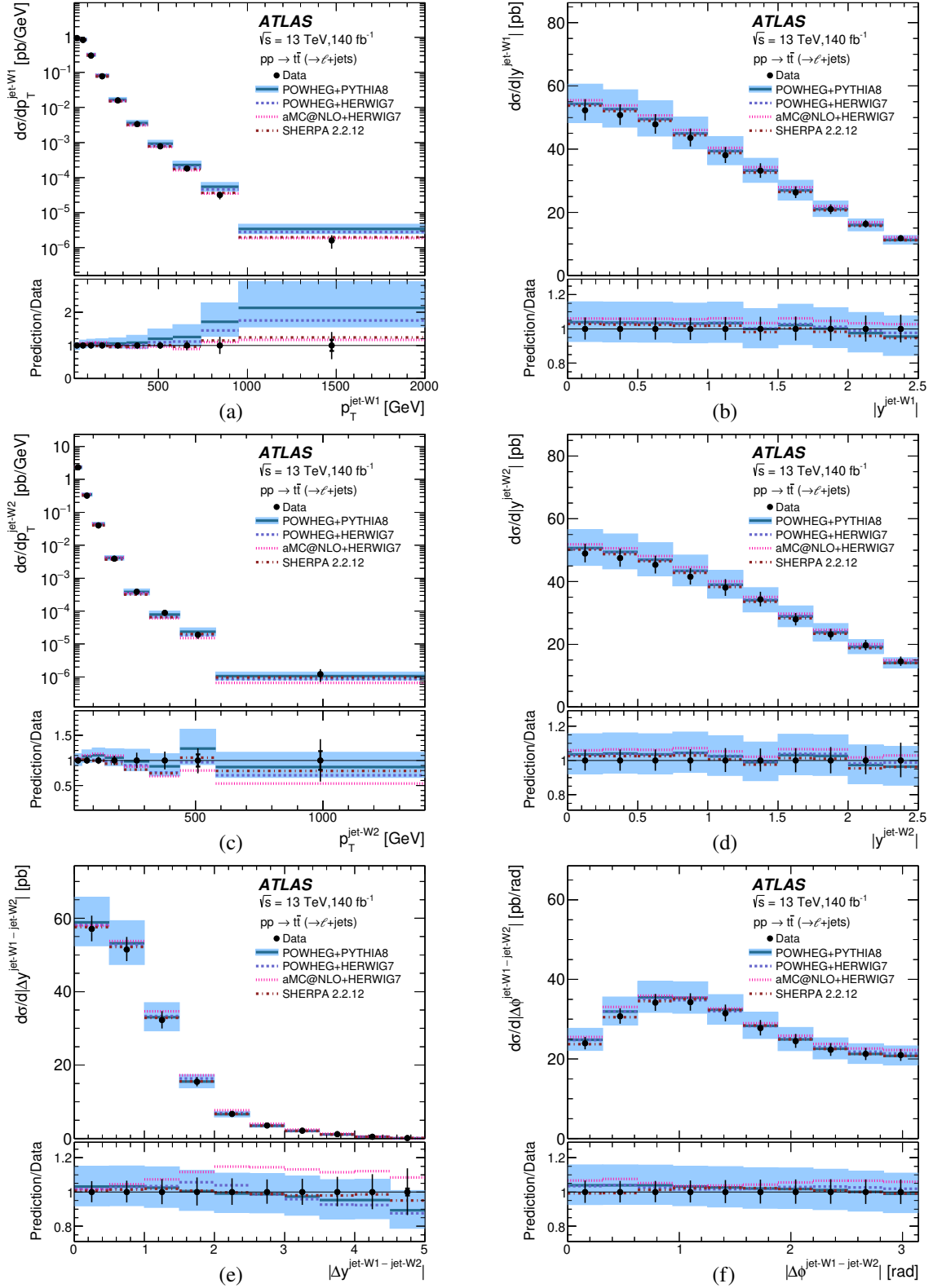


Figure 14: The measured differential cross-sections for $t\bar{t}$ production in the ℓ +jets decay mode as functions of (a) $p_T^{\text{jet-W1}}$, (b) $|y^{\text{jet-W1}}|$, (c) $p_T^{\text{jet-W2}}$, (d) $|y^{\text{jet-W2}}|$, (e) $|\Delta y^{\text{jet-W1} - \text{jet-W2}}|$ and (f) $|\Delta\phi^{\text{jet-W1} - \text{jet-W2}}|$ (dots) in the $t\bar{t}$ inclusive channel. The NLO QCD predictions from PwG+Py8 (solid lines), PwG+Hw7 (dashed lines), aMC@NLO+Hw7 (dotted lines) and SHERPA 2.2.12 (dot-dashed lines) normalised to $O(\text{NNLO}+\text{NNLL})$ are also shown. The inner (outer) error bars represent the statistical uncertainties (the statistical and systematic uncertainties added in quadrature). For most of the points, the inner error bars are smaller than the marker size and, thus, not visible. The shaded bands represent the theoretical uncertainty in the PwG+Py8 prediction. The lower panels of the figures show the ratios of the predicted and the measured cross-sections.

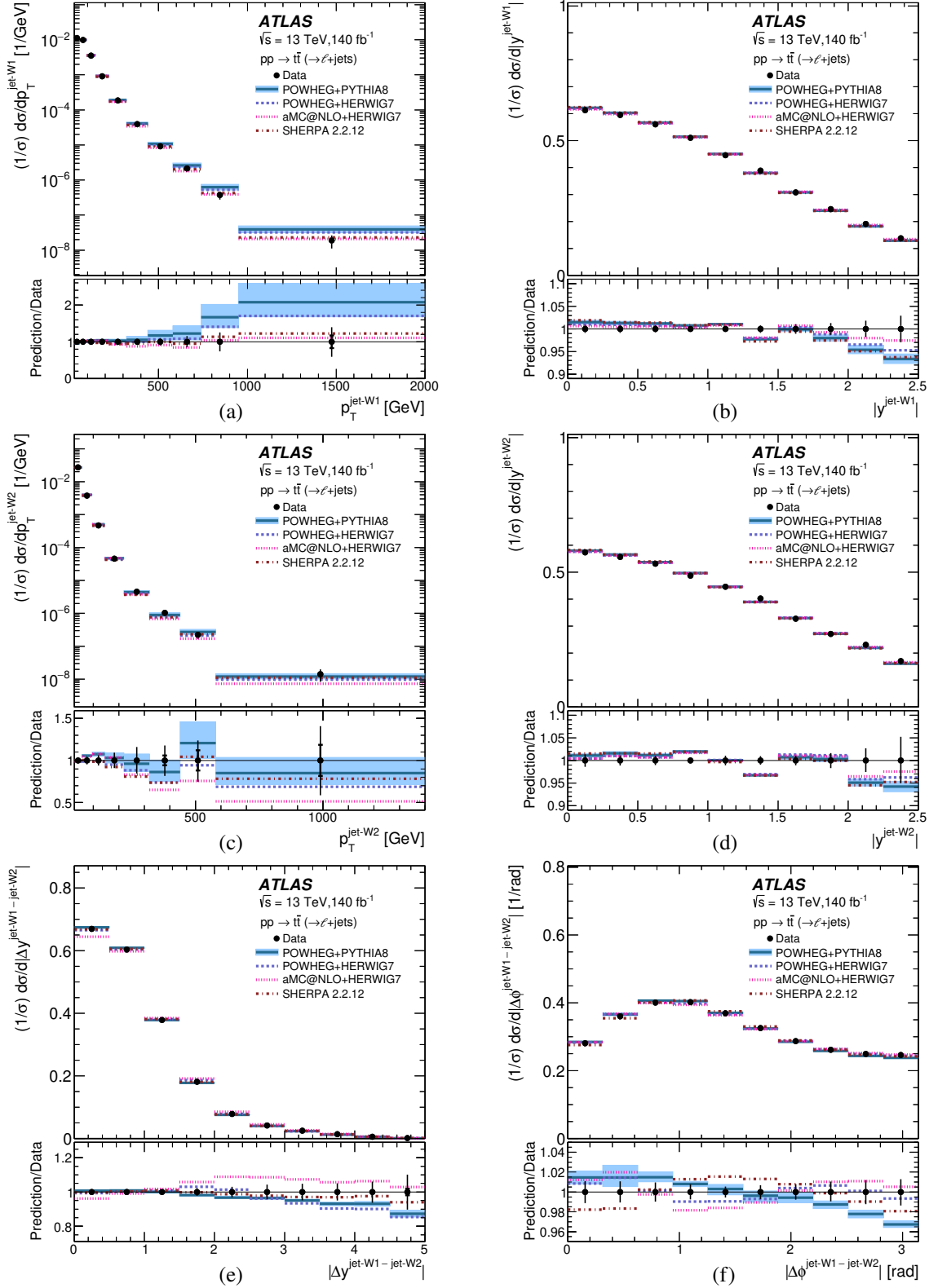


Figure 15: The measured normalised differential cross-sections for $t\bar{t}$ production in the ℓ +jets channel as functions of (a) $p_T^{\text{jet-W1}}$, (b) $|y^{\text{jet-W1}}|$, (c) $p_T^{\text{jet-W2}}$, (d) $|y^{\text{jet-W2}}|$, (e) $|\Delta y^{\text{jet-W1} - \text{jet-W2}}|$ and (f) $|\Delta\phi^{\text{jet-W1} - \text{jet-W2}}|$ (dots) in the $t\bar{t}$ inclusive channel. The NLO QCD predictions from PwG+Py8 (solid lines), PwG+Hw7 (dashed lines), aMC@NLO+Hw7 (dotted lines) and SHERPA 2.2.12 (dot-dashed lines) are also shown. The inner (outer) error bars represent the statistical uncertainties (the statistical and systematic uncertainties added in quadrature). For most of the points, the inner error bars are smaller than the marker size and, thus, not visible. The shaded bands represent the theoretical uncertainty in the PwG+Py8 prediction. The lower panels of the figures show the ratios of the predicted and the measured cross-sections.

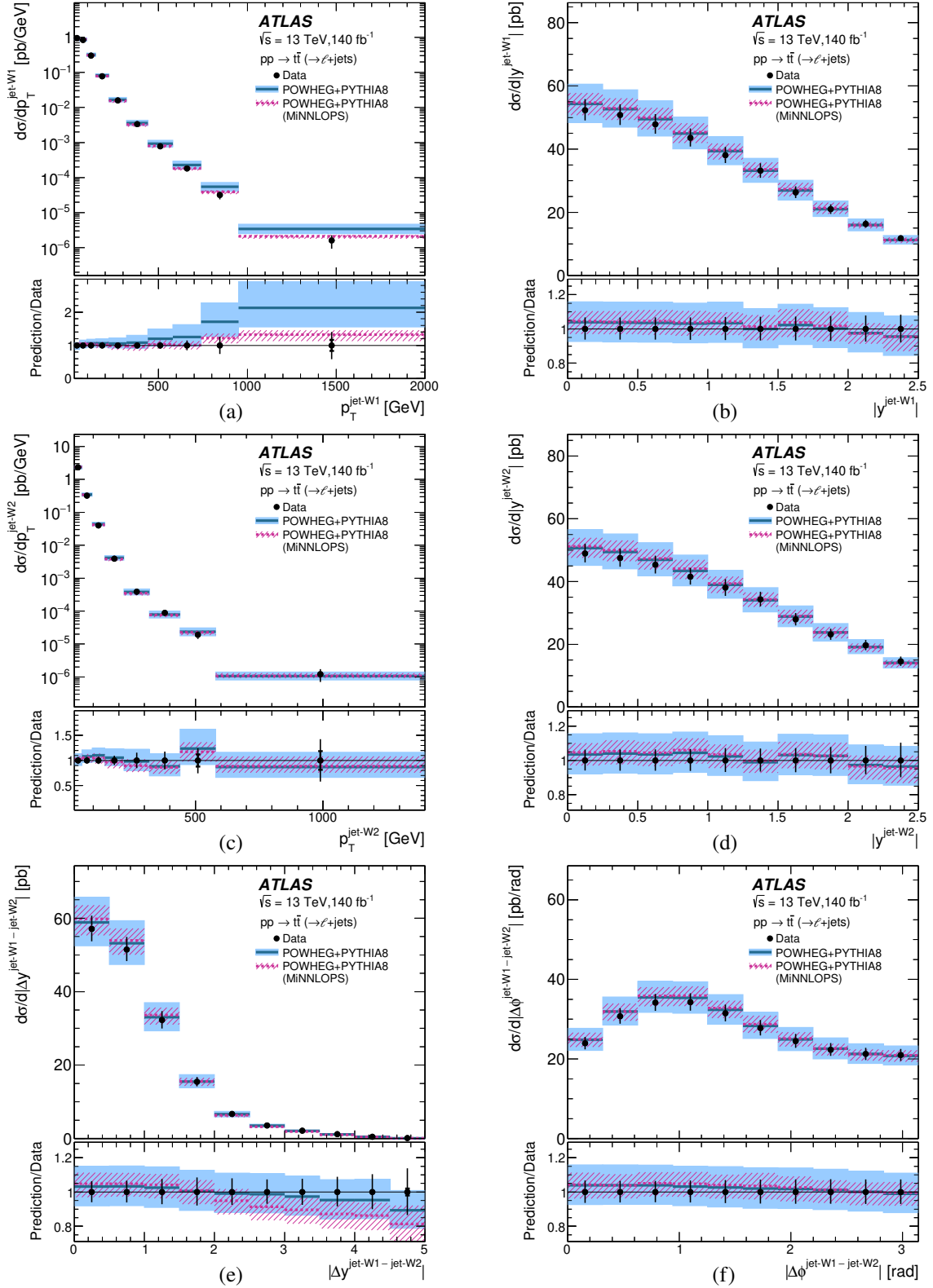


Figure 16: The measured differential cross-sections for $t\bar{t}$ production in the ℓ +jets decay mode as functions of (a) $p_T^{\text{jet-W1}}$, (b) $|y^{\text{jet-W1}}|$, (c) $p_T^{\text{jet-W2}}$, (d) $|y^{\text{jet-W2}}|$, (e) $|\Delta y^{\text{jet-W1} - \text{jet-W2}}|$ and (f) $|\Delta\phi^{\text{jet-W1} - \text{jet-W2}}|$ (dots) in the $t\bar{t}$ inclusive channel. The NLO QCD predictions from PwG+Py8 (solid lines) and the NNLO QCD predictions from PwG+Py8 MinnLOPS (dashed lines) are also shown. Both predictions are normalised to the $O(\text{NNLO}+\text{NNLL})$ total cross-section. The inner (outer) error bars represent the statistical uncertainties (the statistical and systematic uncertainties added in quadrature). For most of the points, the inner error bars are smaller than the marker size and, thus, not visible. The shaded (hatched) bands represent the theoretical uncertainty in the PwG+Py8 (PwG+Py8 MinnLOPS) prediction. The lower panels of the figures show the ratios of the predicted and the measured cross-sections.

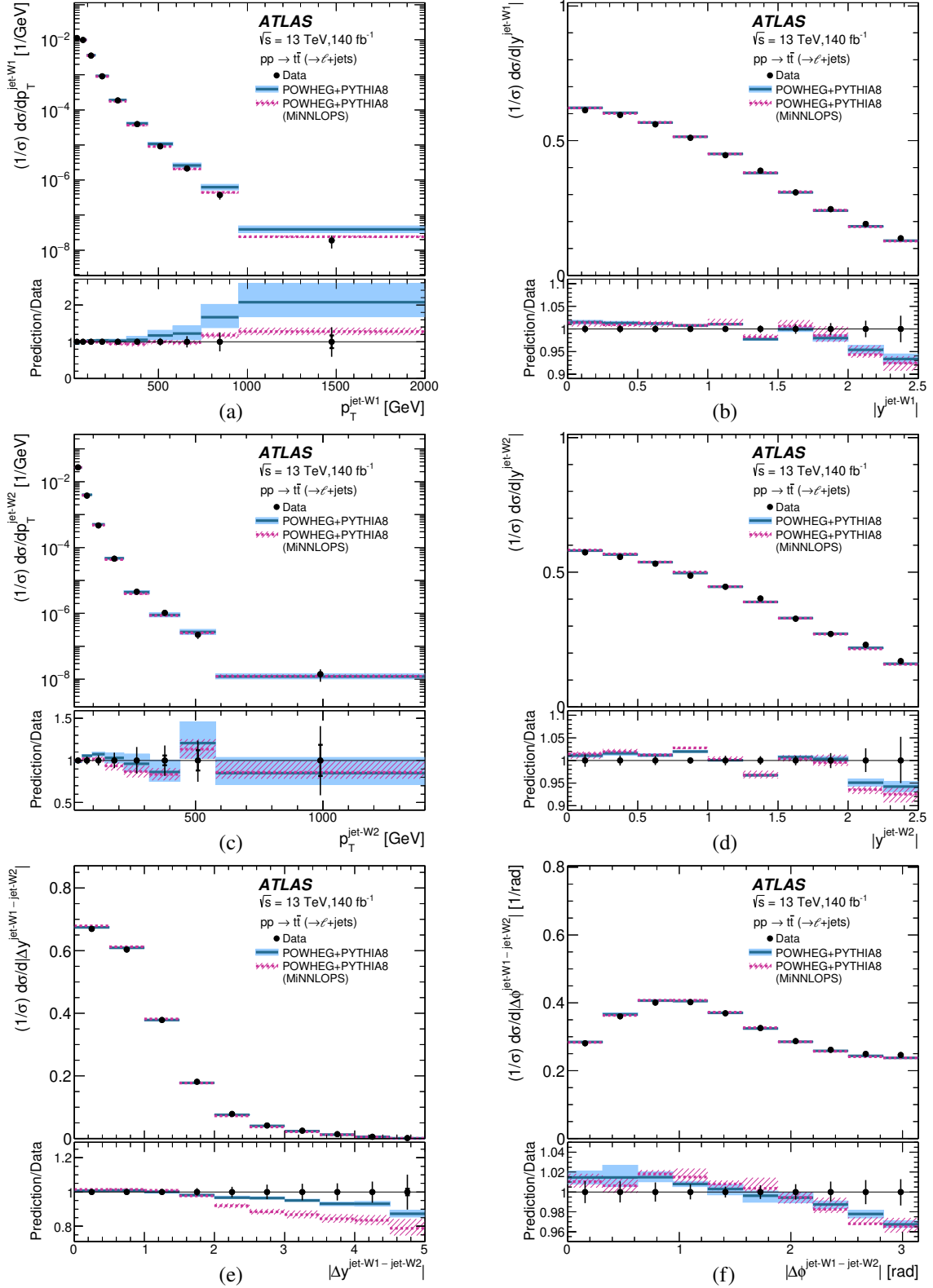


Figure 17: The measured normalised differential cross-sections for $t\bar{t}$ production in the ℓ +jets decay mode as functions of (a) $p_T^{\text{jet-W1}}$, (b) $|y^{\text{jet-W1}}|$, (c) $p_T^{\text{jet-W2}}$, (d) $|y^{\text{jet-W2}}|$, (e) $|\Delta y^{\text{jet-W1-jet-W2}}|$ and (f) $|\Delta\phi^{\text{jet-W1-jet-W2}}|$ (dots) in the $t\bar{t}$ inclusive channel. The NLO QCD predictions from PwG+Py8 (solid lines) and the NNLO QCD predictions from PwG+Py8 MINNLOPS (dashed lines) are also shown. The inner (outer) error bars represent the statistical uncertainties (the statistical and systematic uncertainties added in quadrature). For most of the points, the inner error bars are smaller than the marker size and, thus, not visible. The shaded (hatched) bands represent the theoretical uncertainty in the PwG+Py8 (PwG+Py8 MINNLOPS) prediction. The lower panels of the figures show the ratios of the predicted and the measured cross-sections.

11.2 Differential cross-sections for the $t\bar{t}+1\text{jet}$ channel

Figures 18 and 19 show the absolute and normalised differential $t\bar{t}$ cross-sections in the $\ell+1\text{jet}$ decay mode for the $t\bar{t}+1\text{jet}$ channel as functions of $p_T^{\text{jet-rad1}}$, $|y^{\text{jet-rad1}}|$, $|\Delta\phi^{\text{toplep-jet-rad1}}|$, $|\Delta\phi^{\text{tophad-jet-rad1}}|$, $|\Delta\phi^{\text{jet-W1-jet-rad1}}|$ and $m^{t\bar{t}-\text{jet-rad1}}$. Values of $p_T^{\text{jet-rad1}}$ and $m^{t\bar{t}-\text{jet-rad1}}$ up to ~ 1.7 TeV and ~ 5.3 TeV, respectively, are measured. The measured cross-section as a function of $p_T^{\text{jet-rad1}}$ ($m^{t\bar{t}-\text{jet-rad1}}$) decreases by more than six (five) orders of magnitude within the measured range. The measured cross-section as a function of $m^{t\bar{t}-\text{jet-rad1}}$ decreases for $m^{t\bar{t}-\text{jet-rad1}} < 0.5$ TeV due to the kinematic constraints. The shape of the measured cross-section as a function of $|y^{\text{jet-rad1}}|$ is different from that of $|y^{\text{jet-W1}}|$: the value of the cross-section at a rapidity of 2.5 relative to the value at 0 is higher for $|y^{\text{jet-rad1}}|$ than for $|y^{\text{jet-W1}}|$, which indicates that the first gluon emission tends to be more isotropic in rapidity than the jets forming the hadronically decaying top quark. This is investigated further by measuring the cross-sections as functions of $|\Delta\phi^{\text{toplep-jet-rad1}}|$ and $|\Delta\phi^{\text{tophad-jet-rad1}}|$: the measured cross-sections have very different shapes, which indicates that the first gluon emission has a higher probability of arising at larger angles from the leptonically decaying top quark. In addition, the measured cross-section as a function of $|\Delta\phi^{\text{jet-W1-jet-rad1}}|$ shows a peak at $|\Delta\phi^{\text{jet-W1-jet-rad1}}| \approx 0.5$ rad and at π rad, which indicates that there are more events with a gluon emission back-to-back with jet-W1, though a fraction of the events has a gluon emission close to jet-W1.

The NLO QCD predictions describe the measurements as functions of $|y^{\text{jet-rad1}}|$, $|\Delta\phi^{\text{toplep-jet-rad1}}|$, $|\Delta\phi^{\text{tophad-jet-rad1}}|$ and $|\Delta\phi^{\text{jet-W1-jet-rad1}}|$ well. As is the case for the measurements in the $t\bar{t}$ inclusive channel, the cross-section as a function of $p_T^{\text{jet-rad1}}$ is described by the predictions from PWG+PY8 and PWG+Hw7 only for $p_T^{\text{jet-rad1}} < 500$ GeV, whereas the predictions from aMC@NLO+Hw7 and SHERPA 2.2.12 provide a good description of the data over the whole measured range. The cross-section as a function of $m^{t\bar{t}-\text{jet-rad1}}$ is well described by all predictions for $m^{t\bar{t}-\text{jet-rad1}} < 3$ TeV. The same conclusions can be drawn from the normalised differential cross-sections in Figure 19.

A significant improvement by the NNLO predictions of PWG+PY8 MINNLOPS is observed for the description of the measured differential cross-sections as functions of $p_T^{\text{jet-rad1}}$ and $m^{t\bar{t}-\text{jet-rad1}}$ relative to the predictions of PWG+PY8, as seen in Figures 20 and 21.

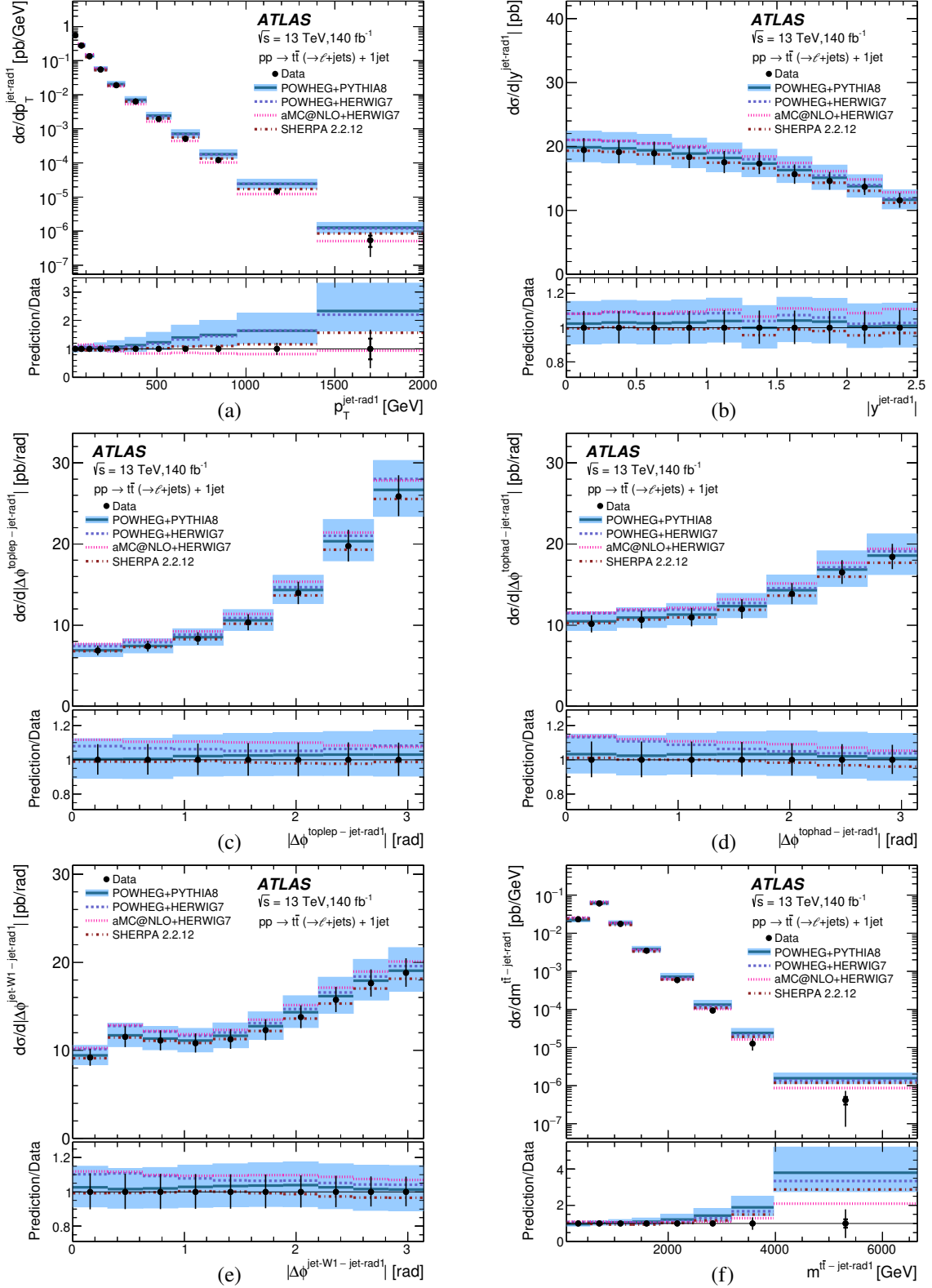


Figure 18: The measured differential cross-sections for $t\bar{t}$ production in the ℓ +jets decay mode as functions of (a) $p_T^{\text{jet-rad1}}$, (b) $|y^{\text{jet-rad1}}|$, (c) $|\Delta\phi^{\text{toplep-jet-rad1}}|$, (d) $|\Delta\phi^{\text{tophad-jet-rad1}}|$, (e) $|\Delta\phi^{\text{jet-W1-jet-rad1}}|$ and (f) $m^{\text{tt-jet-rad1}}$ (dots) in the $t\bar{t}$ +1jet channel. The NLO QCD predictions from PwG+Py8 (solid lines), PwG+Hw7 (dashed lines), aMC@NLO+Hw7 (dotted lines) and SHERPA 2.2.12 (dot-dashed lines) normalised to $O(\text{NNLO+NNLL})$ are also shown. The inner (outer) error bars represent the statistical uncertainties (the statistical and systematic uncertainties added in quadrature). For most of the points, the inner error bars are smaller than the marker size and, thus, not visible. The shaded bands represent the theoretical uncertainty in the PwG+Py8 prediction. The lower panels of the figures show the ratios of the predicted and the measured cross-sections.

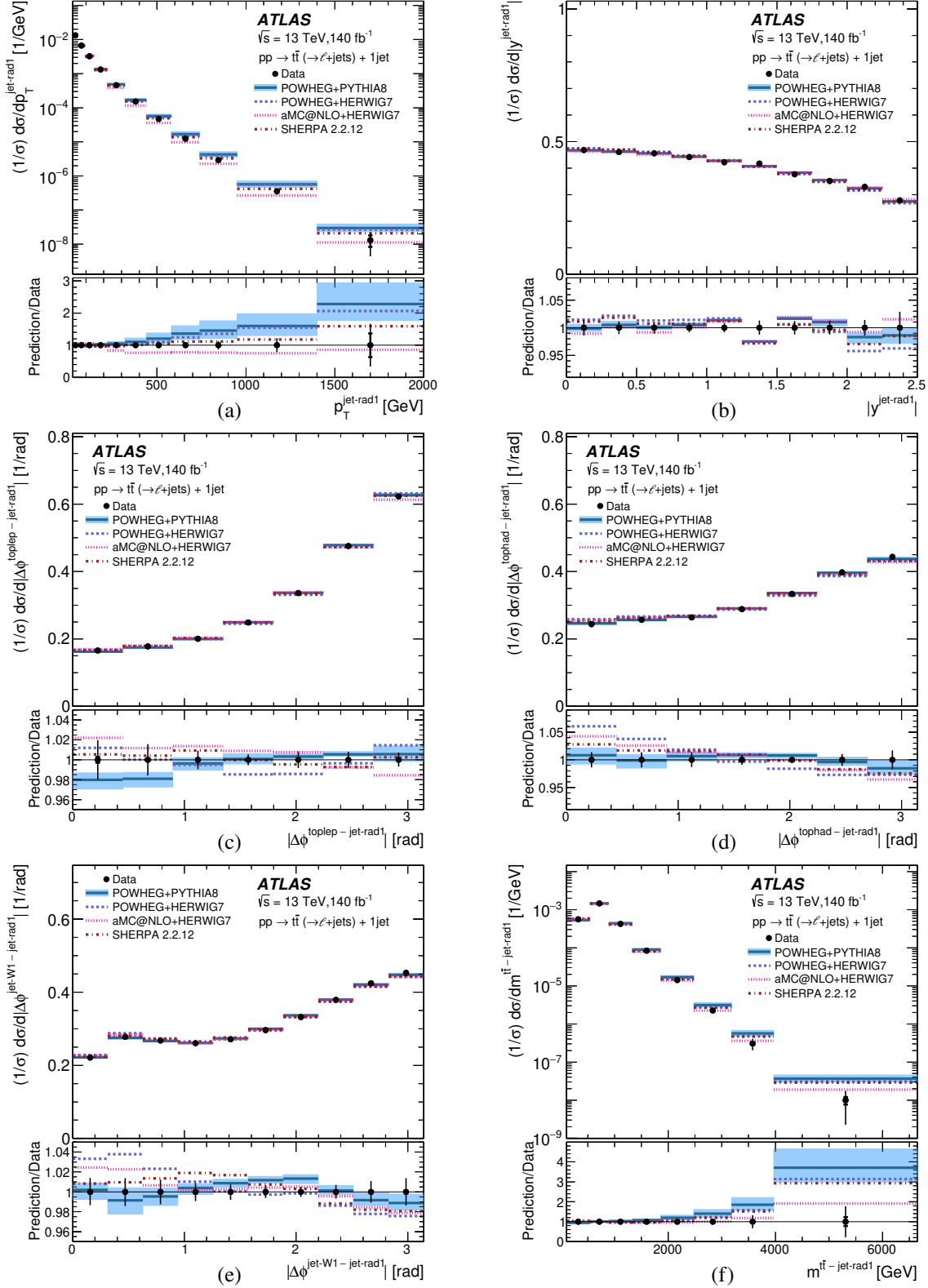


Figure 19: The measured normalised differential cross-sections for $t\bar{t}$ production in the ℓ +jets decay mode as functions of (a) $p_T^{\text{jet-rad1}}$, (b) $|y^{\text{jet-rad1}}|$, (c) $|\Delta\phi^{\text{toplep-jet-rad1}}|$, (d) $|\Delta\phi^{\text{tophad-jet-rad1}}|$, (e) $|\Delta\phi^{\text{jet-W1-jet-rad1}}|$ and (f) $m^{\text{tt-jet-rad1}}$ (dots) in the $t\bar{t}$ +1jet channel. The NLO QCD predictions from PwG+Py8 (solid lines), PwG+Hw7 (dashed lines), aMC@NLO+Hw7 (dotted lines) and SHERPA 2.2.12 (dot-dashed lines) are also shown. The inner (outer) error bars represent the statistical uncertainties (the statistical and systematic uncertainties added in quadrature). For most of the points, the inner error bars are smaller than the marker size and, thus, not visible. The shaded bands represent the theoretical uncertainty in the PwG+Py8 prediction. The lower panels of the figures show the ratios of the predicted and the measured cross-sections.

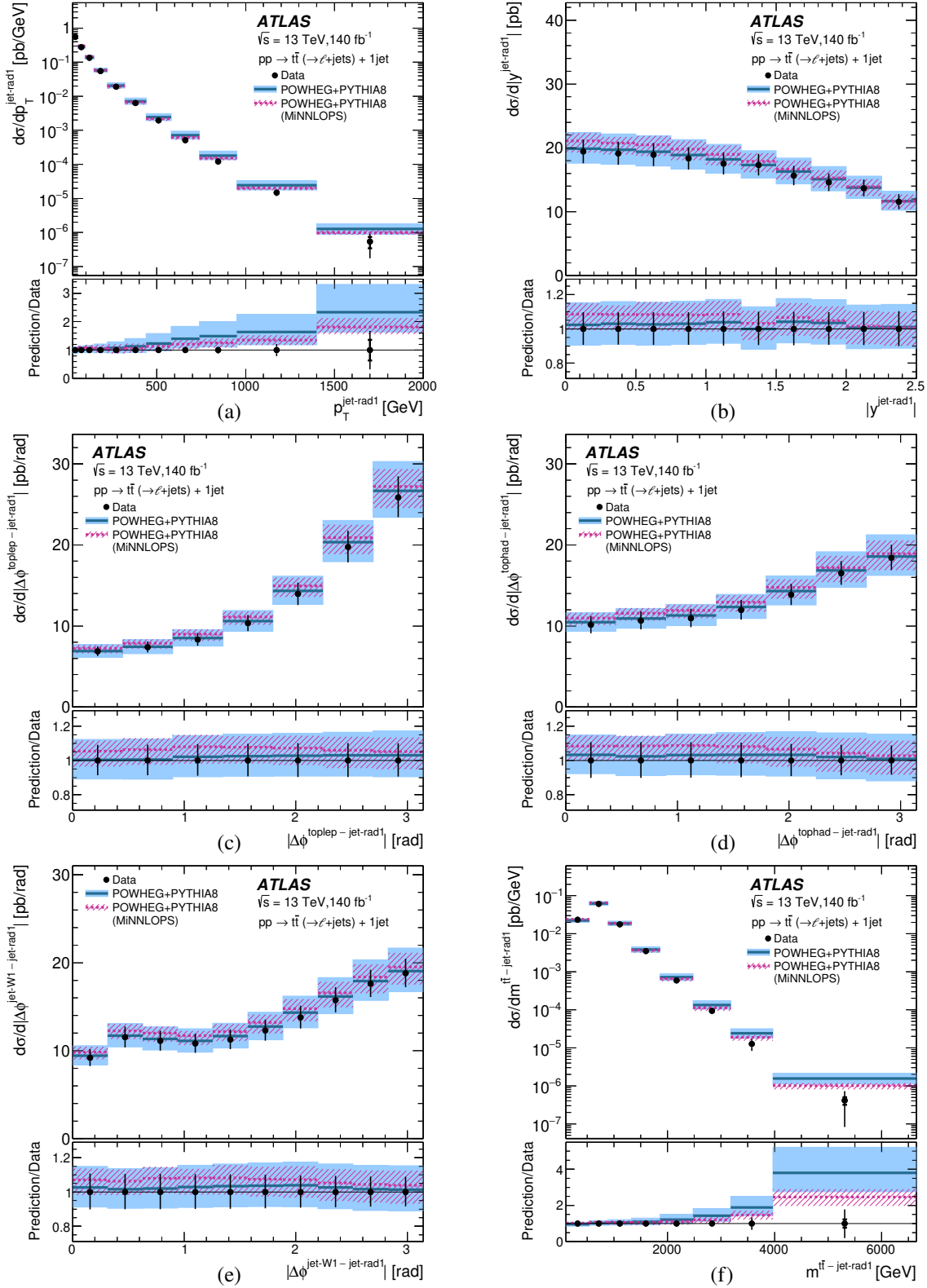


Figure 20: The measured differential cross-sections for $t\bar{t}$ production in the ℓ +jets decay mode as functions of (a) $p_T^{\text{jet-rad1}}$, (b) $|y^{\text{jet-rad1}}|$, (c) $|\Delta\phi^{\text{toplep-jet-rad1}}|$, (d) $|\Delta\phi^{\text{tophad-jet-rad1}}|$, (e) $|\Delta\phi^{\text{jet-W1-jet-rad1}}|$ and (f) $m^{\text{t}\bar{\text{t}}-\text{jet-rad1}}$ (dots) in the $t\bar{t}$ +1jet channel. The NLO QCD predictions from PwG+Py8 (solid lines) and the NNLO QCD predictions from PwG+Py8 MINNLOPS (dashed lines) are also shown. Both predictions are normalised to the $O(\text{NNLO}+\text{NNLL})$ total cross-section. The inner (outer) error bars represent the statistical uncertainties (the statistical and systematic uncertainties added in quadrature). For most of the points, the inner error bars are smaller than the marker size and, thus, not visible. The shaded (hatched) bands represent the theoretical uncertainty in the PwG+Py8 (PwG+Py8 MINNLOPS) prediction. The lower panels of the figures show the ratios of the predicted and the measured cross-sections.

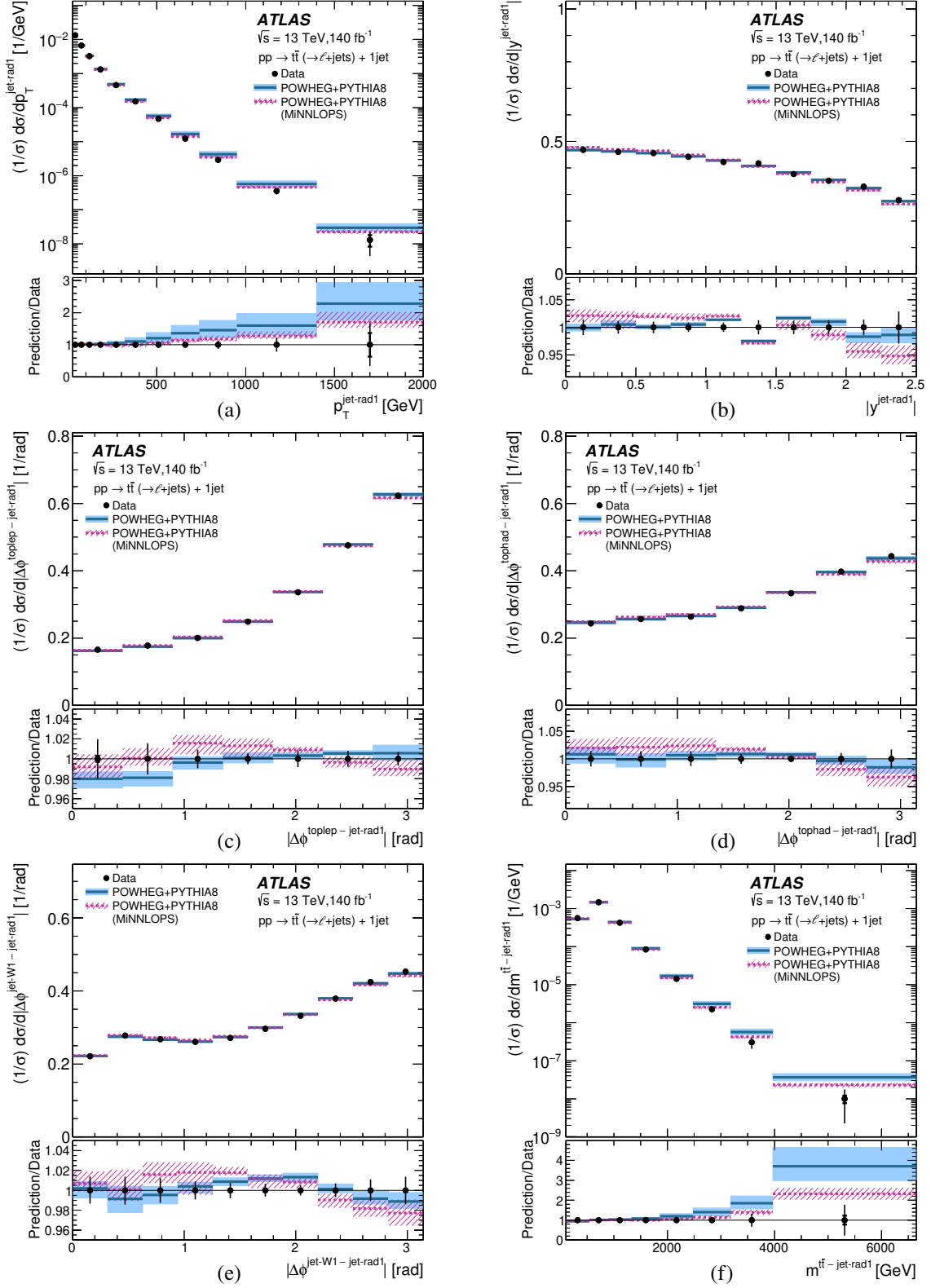


Figure 21: The measured normalised differential cross-sections for $t\bar{t}$ production in the ℓ +jets decay mode as functions of (a) $p_T^{\text{jet-rad1}}$, (b) $|y^{\text{jet-rad1}}|$, (c) $|\Delta\phi^{\text{toplep-jet-rad1}}|$, (d) $|\Delta\phi^{\text{tophad-jet-rad1}}|$, (e) $|\Delta\phi^{\text{jet-W1-jet-rad1}}|$ and (f) $m^{t\bar{t}-\text{jet-rad1}}$ (dots) in the $t\bar{t}$ +1jet channel. The NLO QCD predictions from PwG+P γ 8 (solid lines) and the NNLO QCD predictions from PwG+P γ 8 MINNLOPS (dashed lines) are also shown. The inner (outer) error bars represent the statistical uncertainties (the statistical and systematic uncertainties added in quadrature). For most of the points, the inner error bars are smaller than the marker size and, thus, not visible. The shaded (hatched) bands represent the theoretical uncertainty in the PwG+P γ 8 (PwG+P γ 8 MINNLOPS) prediction. The lower panels of the figures show the ratios of the predicted and the measured cross-sections.

11.3 Differential cross-sections for the $t\bar{t}+2$ jets channel

Figures 22 and 23 (Figures 24 and 25) show the absolute (normalised) differential $t\bar{t}$ cross-sections in the ℓ +jets decay mode for the $t\bar{t}+2$ jets channel as functions of $p_T^{\text{jet-rad2}}$, $|y^{\text{jet-rad2}}|$, $|\Delta y^{\text{jet-rad1-jet-rad2}}|$, $|\Delta\phi^{\text{jet-rad1-jet-rad2}}|$, $|\Delta\phi^{\text{tolep-jet-rad2}}|$, $|\Delta\phi^{\text{tophad-jet-rad2}}|$, $|\Delta\phi^{\text{jet-W1-jet-rad2}}|$ and $m^{\text{jet-rad1-jet-rad2}}$. Values of $p_T^{\text{jet-rad2}}$ and $m^{\text{jet-rad1-jet-rad2}}$ up to ~ 1.2 TeV and ~ 4 TeV, respectively, are measured. The measured cross-sections as functions of $p_T^{\text{jet-rad2}}$ and $m^{\text{jet-rad1-jet-rad2}}$ decrease by more than five orders of magnitude within the measured range. The measured cross-section as a function of $|y^{\text{jet-rad2}}|$ decreases as the rapidity increases and has a very similar shape to the one for $|y^{\text{jet-rad1}}|$. The measured cross-section as a function of $|\Delta y^{\text{jet-rad1-jet-rad2}}|$ decreases rapidly with increasing $|\Delta y^{\text{jet-rad1-jet-rad2}}|$ and the $|\Delta\phi^{\text{jet-rad1-jet-rad2}}|$ distribution exhibits peaks at 0.5 rad and π rad, with approximately the same rate; these features indicate that the second gluon emission tends to be close in rapidity to the first gluon emission and that there is a weak dependence on the difference in ϕ between the first and second gluon emissions. The decrease of the cross-section at $|\Delta\phi^{\text{jet-rad1-jet-rad2}}| \approx 0$ is due to the fact that since the jets are reconstructed with $R = 0.4$, they cannot be closer than that value in ϕ if they have the same rapidity. The measured cross-sections as functions of $|\Delta\phi^{\text{tolep-jet-rad2}}|$, $|\Delta\phi^{\text{tophad-jet-rad2}}|$ and $|\Delta\phi^{\text{jet-W1-jet-rad2}}|$ show similar features to those measured for jet-rad1; therefore, the second gluon emission also has a higher probability of arising at larger angles from the leptonically decaying top quark.

The NLO QCD predictions describe the measurements as functions of $|y^{\text{jet-rad2}}|$, $|\Delta y^{\text{jet-rad1-jet-rad2}}|$, $|\Delta\phi^{\text{jet-rad1-jet-rad2}}|$, $|\Delta\phi^{\text{tolep-jet-rad2}}|$, $|\Delta\phi^{\text{tophad-jet-rad2}}|$ and $|\Delta\phi^{\text{jet-W1-jet-rad2}}|$ well, however the prediction from aMC@NLO+Hw7 has a different shape than the data for the normalised $|\Delta y^{\text{jet-rad1-jet-rad2}}|$ distribution (see 24(c)). The measurement as a function of $p_T^{\text{jet-rad2}}$ is described adequately by the predictions of PWG+PY8, PWG+Hw7 and SHERPA 2.2.12, whereas the prediction from aMC@NLO+Hw7 disagrees with the data for $p_T^{\text{jet-rad2}} > 200$ GeV. For $m^{\text{jet-rad1-jet-rad2}}$, the predictions describe the data only for $m^{\text{jet-rad1-jet-rad2}} < 1$ TeV; for larger $m^{\text{jet-rad1-jet-rad2}}$ values, the predictions of PWG+PY8, PWG+Hw7 and SHERPA 2.2.12 (aMC@NLO+Hw7) overestimate (underestimate) the data.

The comparison of the NNLO predictions with the measurements in the $t\bar{t}+2$ jets channel is shown in Figures 26 to 29. The central value of the NNLO predictions for the angular variables in this channel has a tendency to be above the data, though the PWG+PY8 MiNNLOPS predictions are compatible with the measurements within the experimental and theoretical uncertainties, except for the normalised cross-section as a function of $|\Delta y^{\text{jet-rad1-jet-rad2}}|$, for which the PWG+PY8 MiNNLOPS prediction is below the data for $|\Delta y^{\text{jet-rad1-jet-rad2}}| > 3$. The description of the data by the NNLO prediction is somewhat worse than that at NLO for the $p_T^{\text{jet-rad2}}$ observable (see Figures 26(a) and 28(a)), especially at high $p_T^{\text{jet-rad2}}$ values. This effect might be attributed to the fact that these calculations are only at lowest order in QCD for the second gluon emission, with higher-order corrections being modelled by the PS, hence further tuning of the parameters might be necessary.

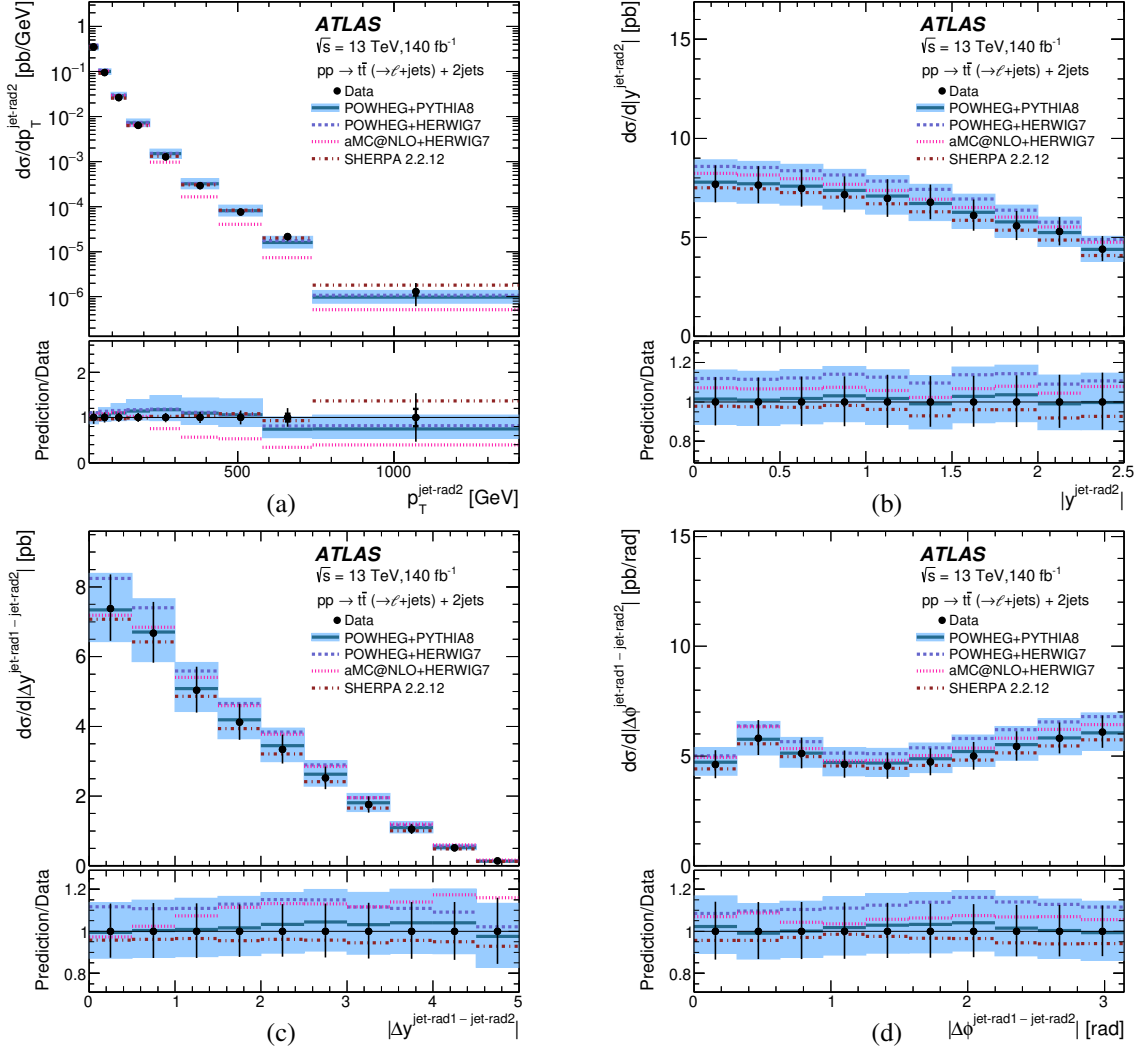


Figure 22: The measured differential cross-sections for $t\bar{t}$ production in the ℓ +jets decay mode as functions of (a) $p_T^{\text{jet-rad2}}$, (b) $|y^{\text{jet-rad2}}|$, (c) $|\Delta y^{\text{jet-rad1} - \text{jet-rad2}}|$ and (d) $|\Delta\phi^{\text{jet-rad1} - \text{jet-rad2}}|$ (dots) in the $t\bar{t}+2\text{jets}$ channel. The NLO QCD predictions from PWG+PY8 (solid lines), PWG+Hw7 (dashed lines), aMC@NLO+Hw7 (dotted lines) and SHERPA 2.2.12 (dot-dashed lines) normalised to $\mathcal{O}(\text{NNLO}+\text{NNLL})$ are also shown. The inner (outer) error bars represent the statistical uncertainties (the statistical and systematic uncertainties added in quadrature). For most of the points, the inner error bars are smaller than the marker size and, thus, not visible. The shaded bands represent the theoretical uncertainty in the PWG+PY8 prediction. The lower panels of the figures show the ratios of the predicted and the measured cross-sections.

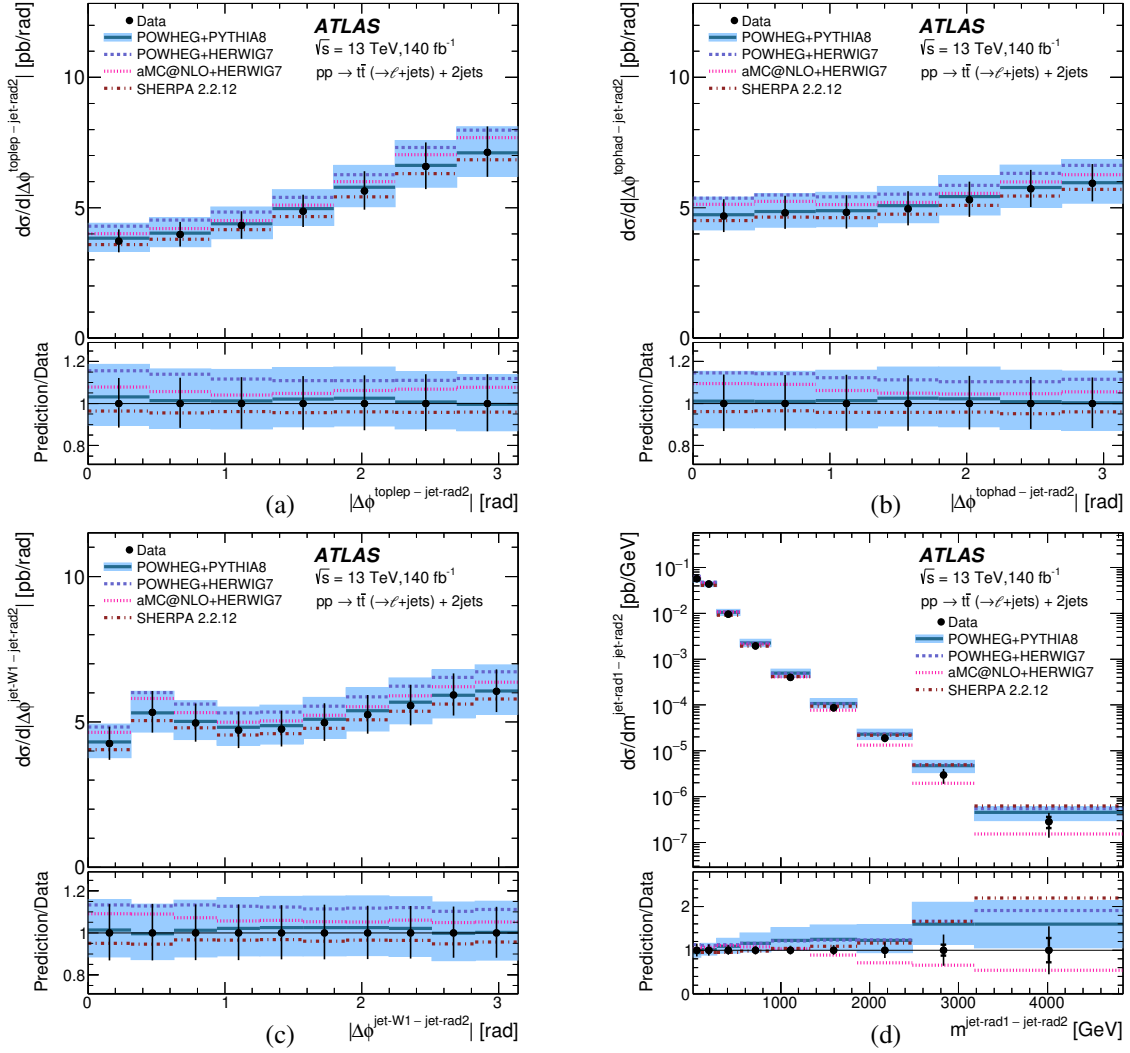


Figure 23: The measured differential cross-sections for $t\bar{t}$ production in the ℓ +jets decay mode as functions of (a) $|\Delta\phi^{\text{toplep-jet-rad2}}|$, (b) $|\Delta\phi^{\text{tophad-jet-rad2}}|$, (c) $|\Delta\phi^{\text{jet-W1-jet-rad2}}|$ and (d) $m^{\text{jet-rad1-jet-rad2}}$ (dots) in the $t\bar{t}+2\text{jets}$ channel. The NLO QCD predictions from PwG+Py8 (solid lines), PwG+Hw7 (dashed lines), aMC@NLO+Hw7 (dotted lines) and SHERPA 2.2.12 (dot-dashed lines) normalised to $O(\text{NNLO}+\text{NNLL})$ are also shown. The inner (outer) error bars represent the statistical uncertainties (the statistical and systematic uncertainties added in quadrature). For most of the points, the inner error bars are smaller than the marker size and, thus, not visible. The shaded bands represent the theoretical uncertainty in the PwG+Py8 prediction. The lower panels of the figures show the ratios of the predicted and the measured cross-sections.

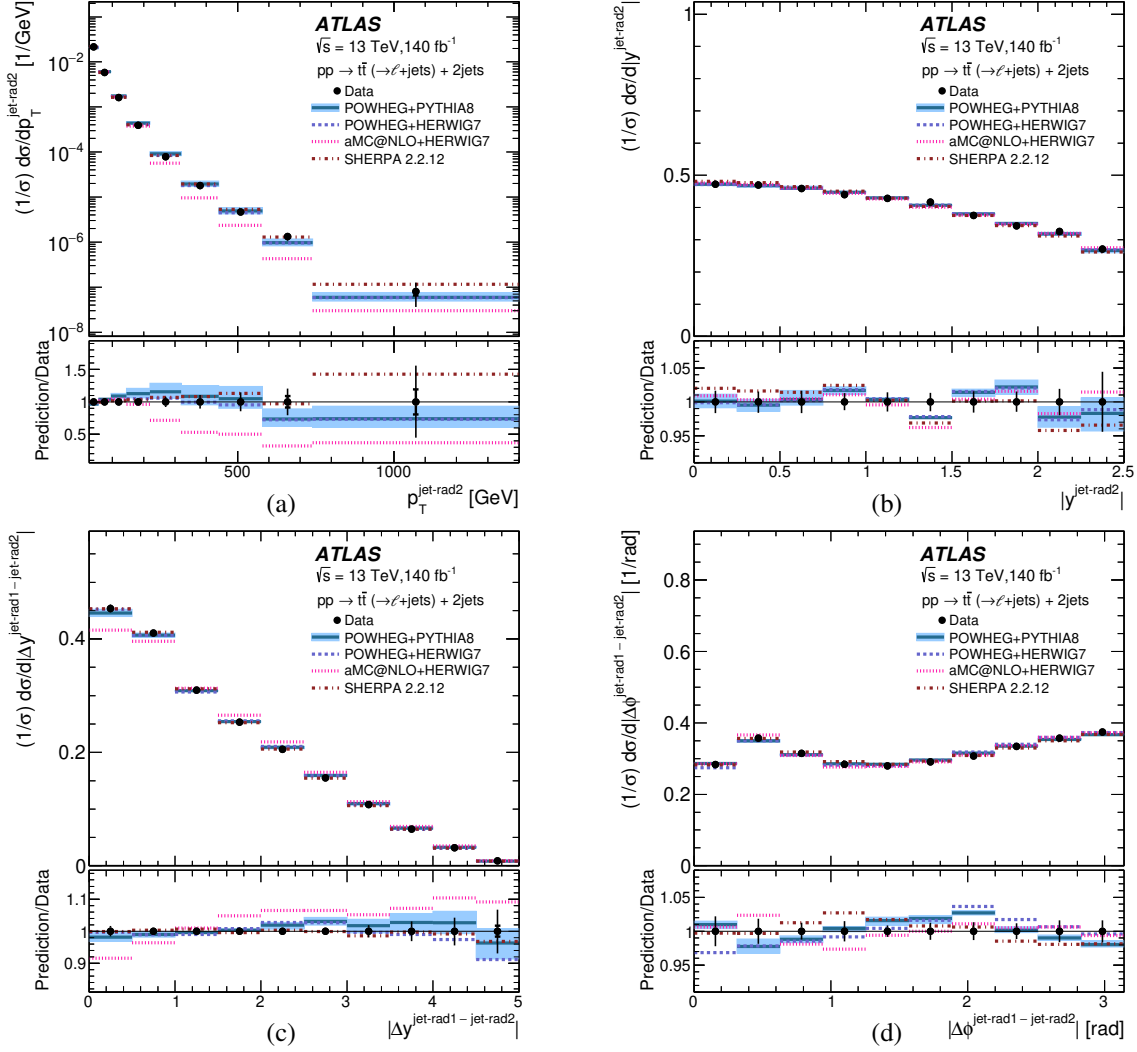


Figure 24: The measured normalised differential cross-sections for $t\bar{t}$ production in the ℓ +jets decay mode as functions of (a) $p_T^{\text{jet-rad2}}$, (b) $|y|^{\text{jet-rad2}}$, (c) $|\Delta y|^{\text{jet-rad1-jet-rad2}}$ and (d) $|\Delta\phi|^{\text{jet-rad1-jet-rad2}}$ (dots) in the $t\bar{t}$ +2jets channel. The NLO QCD predictions from PwG+Py8 (solid lines), PwG+Hw7 (dashed lines), aMC@NLO+Hw7 (dotted lines) and SHERPA 2.2.12 (dot-dashed lines) are also shown. The inner (outer) error bars represent the statistical uncertainties (the statistical and systematic uncertainties added in quadrature). For most of the points, the inner error bars are smaller than the marker size and, thus, not visible. The shaded bands represent the theoretical uncertainty in the PwG+Py8 prediction. The lower panels of the figures show the ratios of the predicted and the measured cross-sections.

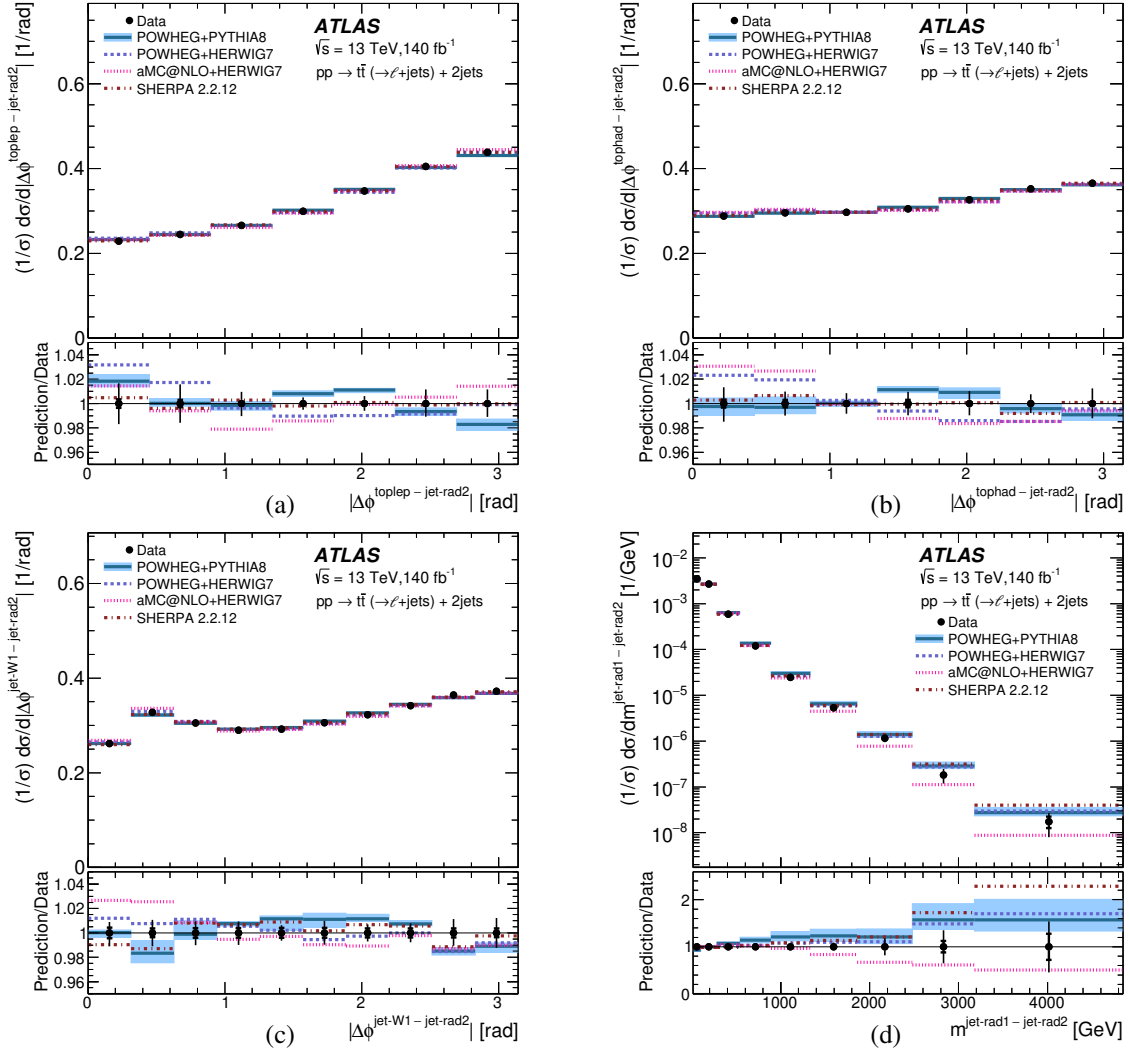


Figure 25: The measured normalised differential cross-sections for $t\bar{t}$ production in the ℓ +jets decay mode as functions of (a) $|\Delta\phi^{\text{toplep-jet-rad2}}|$, (b) $|\Delta\phi^{\text{tophad-jet-rad2}}|$, (c) $|\Delta\phi^{\text{jet-W1-jet-rad2}}|$ and (d) $m^{\text{jet-rad1-jet-rad2}}$ (dots) in the $t\bar{t}+2\text{jets}$ channel. The NLO QCD predictions from PwG+Py8 (solid lines), PwG+Hw7 (dashed lines), aMC@NLO+Hw7 (dotted lines) and SHERPA 2.2.12 (dot-dashed lines) are also shown. The inner (outer) error bars represent the statistical uncertainties (the statistical and systematic uncertainties added in quadrature). For most of the points, the inner error bars are smaller than the marker size and, thus, not visible. The shaded bands represent the theoretical uncertainty in the PwG+Py8 prediction. The lower panels of the figures show the ratios of the predicted and the measured cross-sections.

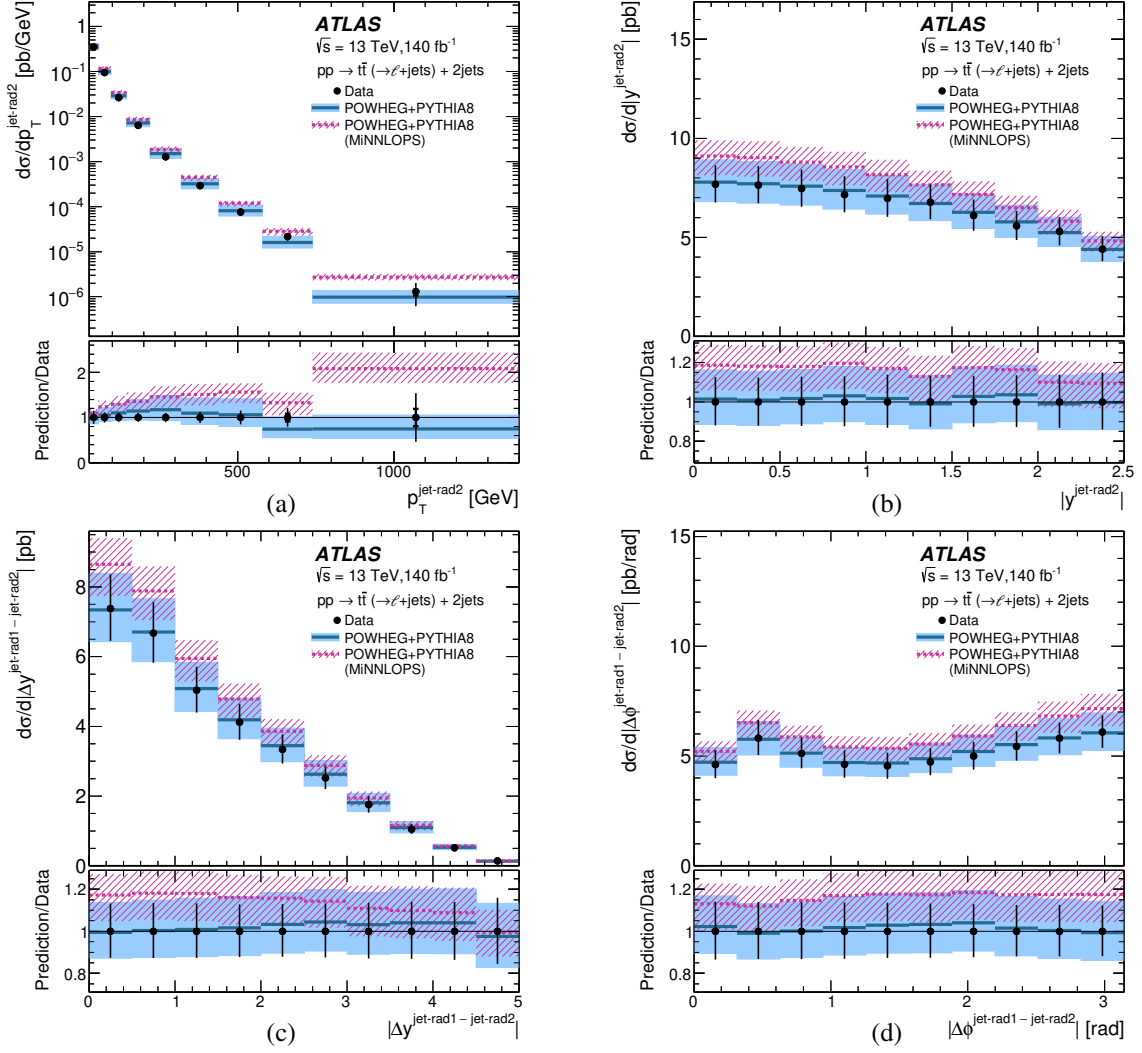


Figure 26: The measured differential cross-sections for $t\bar{t}$ production in the ℓ +jets decay mode as functions of (a) $p_T^{\text{jet-rad2}}$, (b) $|y^{\text{jet-rad2}}|$, (c) $|\Delta y^{\text{jet-rad1} - \text{jet-rad2}}|$ and (d) $|\Delta\phi^{\text{jet-rad1} - \text{jet-rad2}}|$ (dots) in the $t\bar{t}$ +2jets channel. The NLO QCD predictions from PwG+Py8 (solid lines) and the NNLO QCD predictions from PwG+Py8 MiNNLOPS (dashed lines) are also shown. Both predictions are normalised to the $\mathcal{O}(\text{NNLO}+\text{NNLL})$ total cross-section. The inner (outer) error bars represent the statistical uncertainties (the statistical and systematic uncertainties added in quadrature). For most of the points, the inner error bars are smaller than the marker size and, thus, not visible. The shaded (hatched) bands represent the theoretical uncertainty in the PwG+Py8 (PwG+Py8 MiNNLOPS) prediction. The lower panels of the figures show the ratios of the predicted and the measured cross-sections.

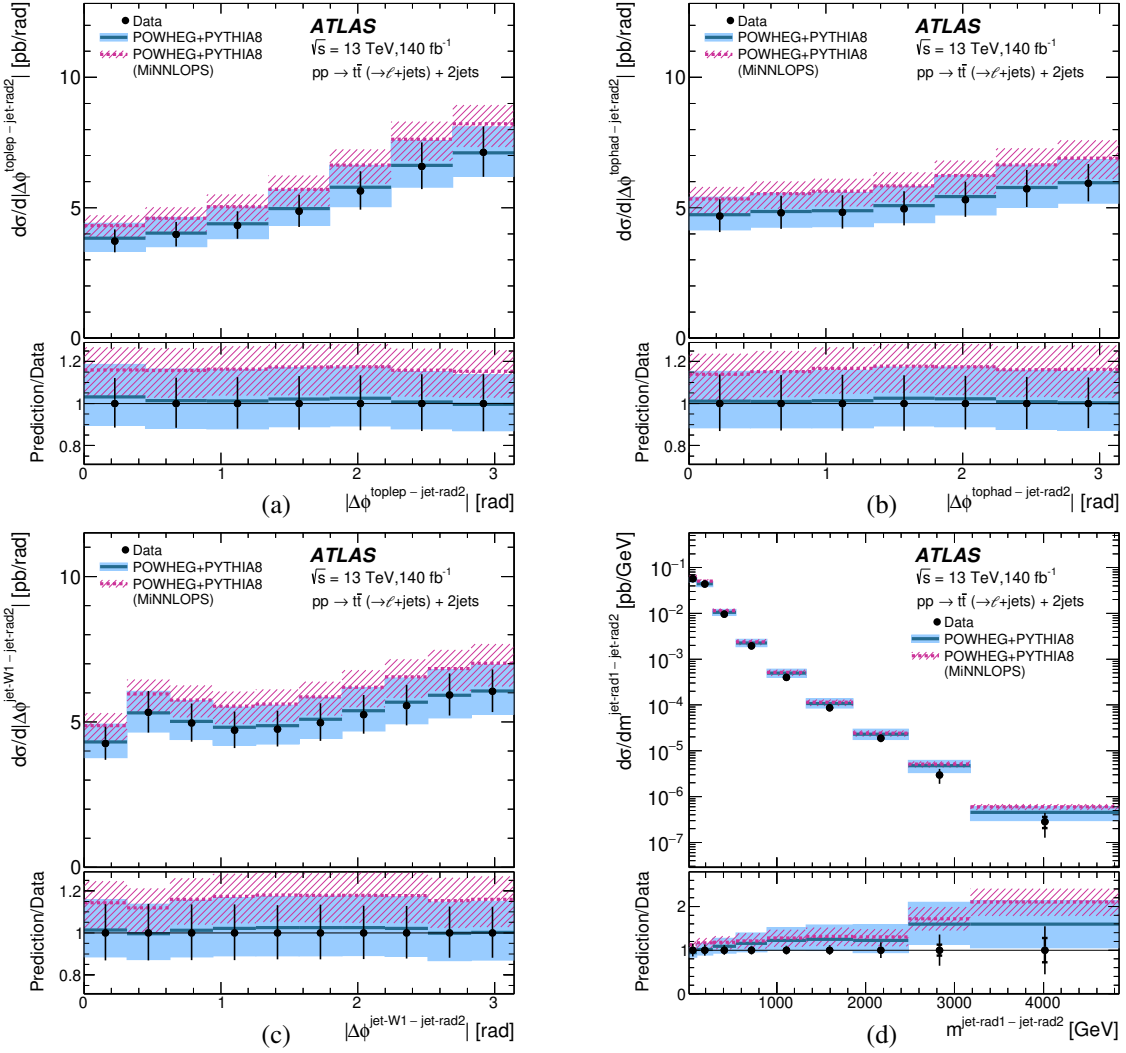


Figure 27: The measured differential cross-sections for $t\bar{t}$ production in the ℓ +jets decay mode as functions of (a) $|\Delta\phi^{\text{toplep}} - \text{jet-rad2}|$, (b) $|\Delta\phi^{\text{tophad}} - \text{jet-rad2}|$, (c) $|\Delta\phi^{\text{jet-W1}} - \text{jet-rad2}|$ and (d) $m^{\text{jet-rad1}} - \text{jet-rad2}$ (dots) in the $t\bar{t}+2jets$ channel. The NLO QCD predictions from PwG+Py8 (solid lines) and the NNLO QCD predictions from PwG+Py8 MiNNLOPS (dashed lines) are also shown. Both predictions are normalised to the $O(\text{NNLO}+\text{NNLL})$ total cross-section. The inner (outer) error bars represent the statistical uncertainties (the statistical and systematic uncertainties added in quadrature). For most of the points, the inner error bars are smaller than the marker size and, thus, not visible. The shaded (hatched) bands represent the theoretical uncertainty in the PwG+Py8 (PwG+Py8 MiNNLOPS) prediction. The lower panels of the figures show the ratios of the predicted and the measured cross-sections.

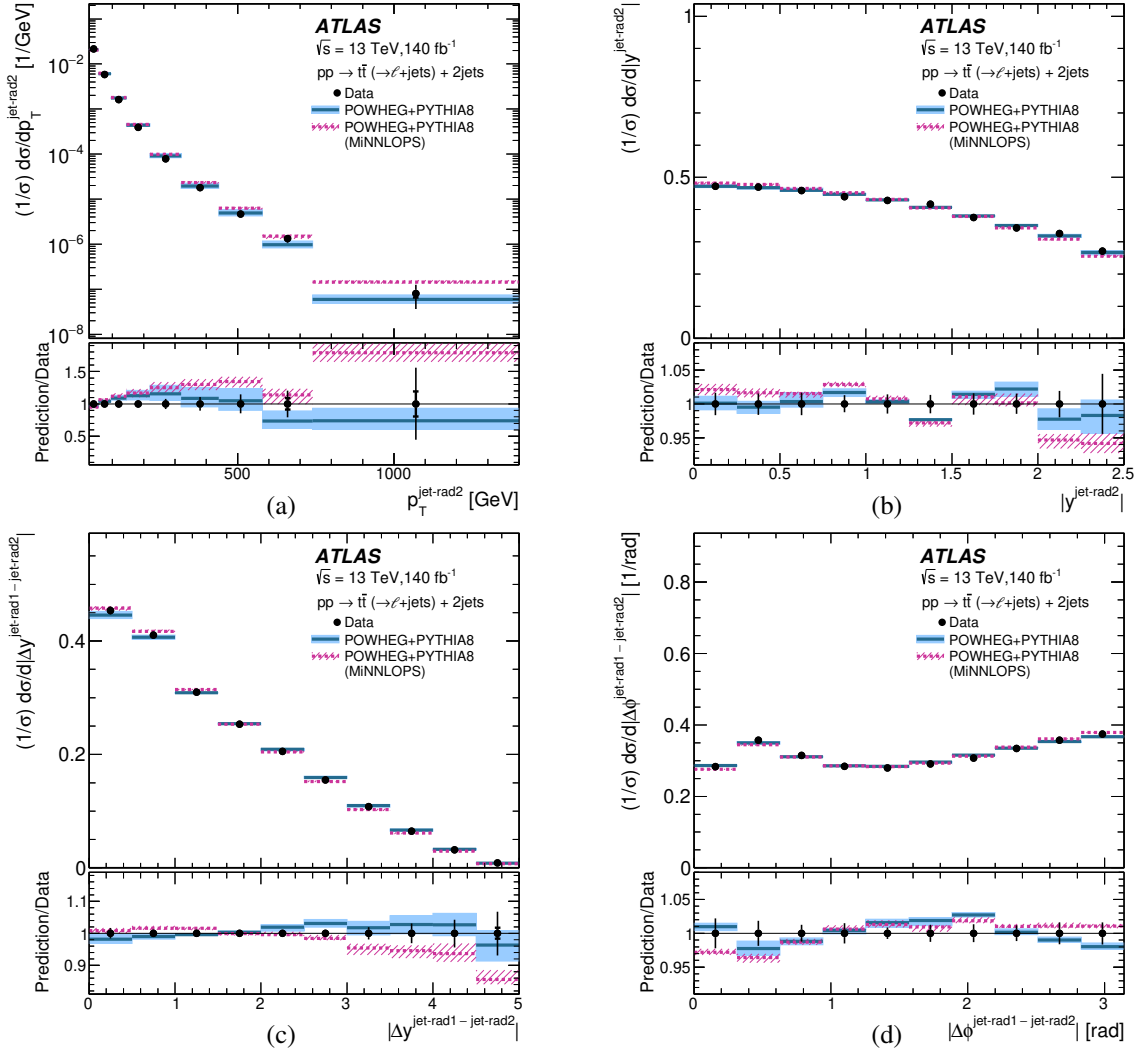


Figure 28: The measured normalised differential cross-sections for $t\bar{t}$ production in the ℓ +jets decay mode as functions of (a) $p_T^{\text{jet-rad2}}$, (b) $|y|^{\text{jet-rad2}}$, (c) $|\Delta y|^{\text{jet-rad1} - \text{jet-rad2}}$ and (d) $|\Delta\phi|^{\text{jet-rad1} - \text{jet-rad2}}$ (dots) in the $t\bar{t}$ +2jets channel. The NLO QCD predictions from PwG+Py8 (solid lines) and the NNLO QCD predictions from PwG+Py8 MINNLOPS (dashed lines) are also shown. The inner (outer) error bars represent the statistical uncertainties (the statistical and systematic uncertainties added in quadrature). For most of the points, the inner error bars are smaller than the marker size and, thus, not visible. The shaded (hatched) bands represent the theoretical uncertainty in the PwG+Py8 (PwG+Py8 MINNLOPS) prediction. The lower panels of the figures show the ratios of the predicted and the measured cross-sections.

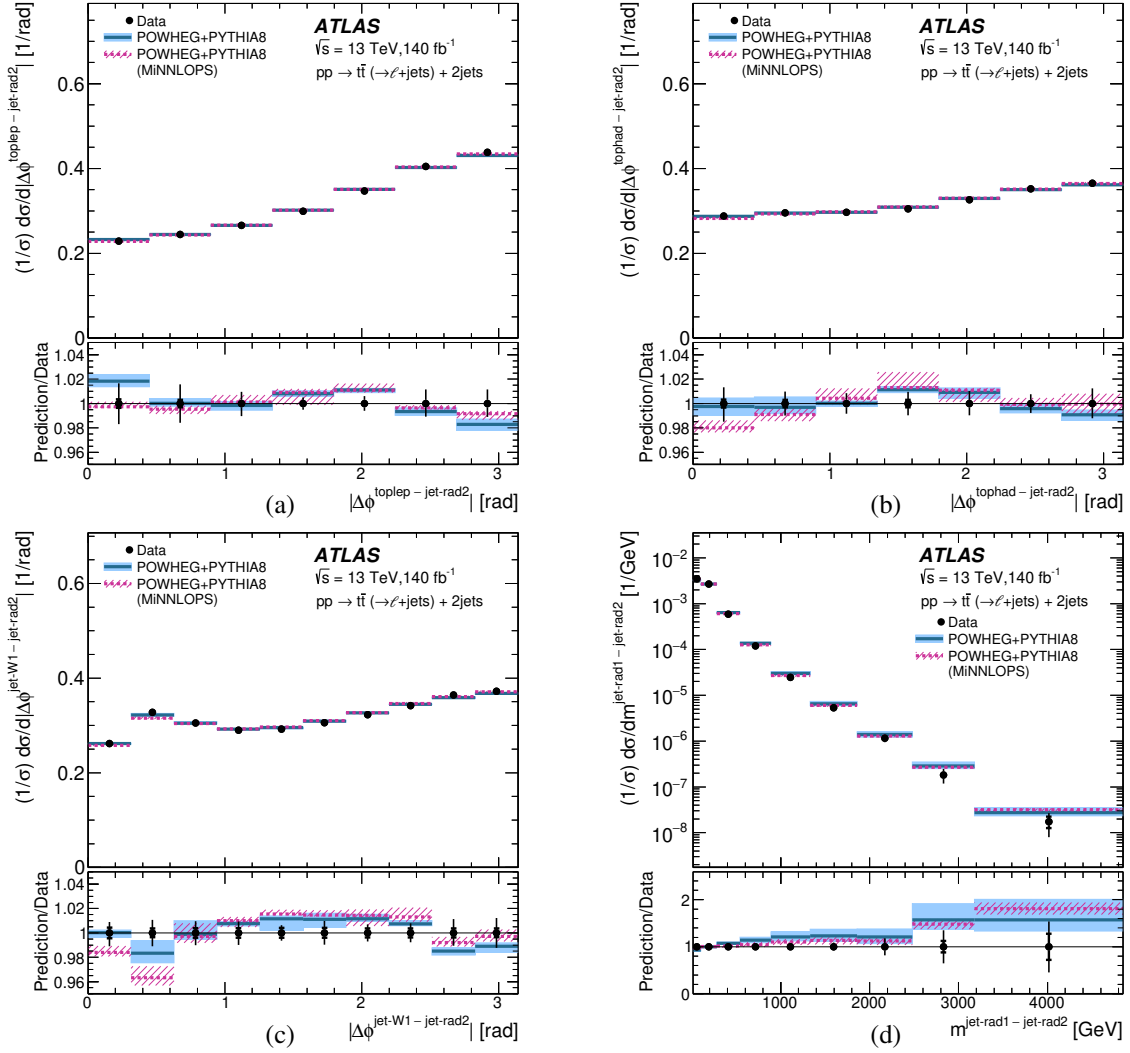


Figure 29: The measured normalised differential cross-sections for $t\bar{t}$ production in the ℓ +jets decay mode as functions of (a) $|\Delta\phi^{\text{toplep}} - \text{jet-rad2}|$, (b) $|\Delta\phi^{\text{tophad}} - \text{jet-rad2}|$, (c) $|\Delta\phi^{\text{jet-W1}} - \text{jet-rad2}|$ and (d) $m^{\text{jet-rad1} - \text{jet-rad2}}$ (dots) in the $t\bar{t}+2jets$ channel. The NLO QCD predictions from PWG+PY8 (solid lines) and the NNLO QCD predictions from PWG+PY8 MiNNLOPS (dashed lines) are also shown. The inner (outer) error bars represent the statistical uncertainties (the statistical and systematic uncertainties added in quadrature). For most of the points, the inner error bars are smaller than the marker size and, thus, not visible. The shaded (hatched) bands represent the theoretical uncertainty in the PWG+PY8 (PWG+PY8 MiNNLOPS) prediction. The lower panels of the figures show the ratios of the predicted and the measured cross-sections.

11.4 χ^2 and p -values

To quantify the level of agreement between the measured differential cross-sections and the theoretical predictions, χ^2 values are evaluated using the following equation [111]

$$\begin{aligned} \chi^2 = & \sum_{i,k} \left(D_i - T_i \left(1 - \sum_j \gamma_{ij} b_j \right) \right) C_{\text{stat,uncor},ik}^{-1} \left(D_k - T_k \left(1 - \sum_j \gamma_{kj} b_j \right) \right) \\ & + \sum_i \log \frac{\delta_{i,\text{uncor}}^2 T_i^2 + \delta_{i,\text{stat}}^2 D_i T_i}{\delta_{i,\text{uncor}}^2 D_i^2 + \delta_{i,\text{stat}}^2 T_i^2} \\ & + \sum_j b_j^2, \end{aligned} \quad (1)$$

known as the Hessian method [112].

In Eq. 1, indices i and k represent different bins in a differential cross-section and index j represents each source of uncertainty. The symbol D represents the measured differential cross-section in a given bin as a function of each observable. The statistical uncertainties are incorporated in the covariance matrix $C_{\text{stat,uncor}}$. This matrix also contains the systematic uncertainty due to non-closure (see Section 10), which is the only experimental uncertainty considered uncorrelated between bins. All the other systematic uncertainties, denoted by the symbol γ in Eq. 1, are considered as correlated between bins and are accounted for by using nuisance parameters (symbols b in Eq. 1). The parameters b are obtained from a minimisation using the MINUIT [113] program.

The symbol T represents the theoretical prediction in each bin of each differential cross-section. The uncertainties that affect the theoretical predictions (see Section 4.3) are taken into account: the uncertainties arising from μ_R , μ_F and the amount of initial- and final-state radiation in the PS are considered as uncorrelated whereas those arising from the PDFs and the value of α_s are considered as correlated bin to bin.

The first term in Eq. 1 gives the main contribution to the χ^2 and the second term is a small bias correction term, referred to as the *log penalty* [112], which arises because the diagonal term of $C_{\text{stat,uncor}}$ is given by $C_{\text{stat,uncor},ii} = \delta_{i,\text{uncor}}^2 T_i^2 + \delta_{i,\text{stat}}^2 D_i T_i$, with different weights for the statistical ($\delta_{i,\text{stat}}$) and uncorrelated ($\delta_{i,\text{uncor}}$) uncertainties. The third term is the sum in quadrature of the nuisance parameters and gives the contribution to the χ^2 arising from the correlated sources of systematic uncertainty.

Table 3 shows the χ^2 and p -values for each differential cross-section and for each theoretical prediction tested separately. Table 4 shows the χ^2 and p -values for the normalised differential cross-sections.³ The p -values obtained confirm the qualitative conclusions discussed in the previous sections. For SHERPA 2.2.12, the p -values are much larger than for the other predictions because the theoretical uncertainties for this prediction are larger.

³ The normalisation constraint used to derive the normalised differential cross-sections lowers the number of degrees of freedom and the rank of the covariance matrix by one unit.

Table 3: χ^2 values, number of degrees of freedom (NDF) and p -values for each observable and each prediction for the absolute differential cross-sections.

Prediction	PwG+PY8			PwG+Hw7		aMC@NLO+Hw7		SHERPA 2.2.12		PwG+PY8 MiNNLOPS	
	Observable	NDF	χ^2	p -value	χ^2	p -value	χ^2	p -value	χ^2	p -value	χ^2
$p_T^{\text{jet-W1}}$	10	6.2	0.79	4.1	0.94	2.7	0.99	1.8	1.0	3.4	0.97
$ y^{\text{jet-W1}} $	10	1.8	1.0	1.6	1.0	2.3	0.99	1.1	1.0	2.7	0.99
$p_T^{\text{jet-W2}}$	8	2.3	0.97	0.45	1.0	2.8	0.94	0.53	1.0	2.6	0.96
$ y^{\text{jet-W2}} $	10	1.9	1.0	1.7	1.0	2.4	0.99	1.1	1.0	2.7	0.99
$ \Delta y^{\text{jet-W1} - \text{jet-W2}} $	10	1.6	1.0	2.7	0.99	4.3	0.93	0.90	1.0	6.0	0.81
$ \Delta\phi^{\text{jet-W1} - \text{jet-W2}} $	10	1.7	1.0	1.6	1.0	2.5	0.99	1.2	1.0	2.1	1.0
$p_T^{\text{jet-rad1}}$	11	7.7	0.74	7.1	0.79	3.3	0.99	2.6	1.0	6.4	0.85
$ y^{\text{jet-rad1}} $	10	1.6	1.0	2.8	0.99	3.4	0.97	0.69	1.0	3.0	0.98
$ \Delta\phi^{\text{toplep} - \text{jet-rad1}} $	7	1.4	0.99	2.2	0.95	2.9	0.89	0.81	1.0	2.3	0.94
$ \Delta\phi^{\text{tophad} - \text{jet-rad1}} $	7	1.4	0.98	2.6	0.92	2.9	0.89	0.85	1.0	2.4	0.93
$ \Delta\phi^{\text{jet-W1} - \text{jet-rad1}} $	10	1.6	1.0	2.9	0.98	3.4	0.97	0.77	1.0	2.7	0.99
$m^{t\bar{t} - \text{jet-rad1}}$	8	7.7	0.46	6.5	0.59	4.4	0.81	4.4	0.82	5.5	0.71
$p_T^{\text{jet-rad2}}$	9	3.2	0.96	4.0	0.91	37.0	< 0.01	1.7	1.0	11.0	0.28
$ y^{\text{jet-rad2}} $	10	1.4	1.0	3.9	0.95	2.4	0.99	0.20	1.0	5.3	0.87
$ \Delta y^{\text{jet-rad1} - \text{jet-rad2}} $	10	1.6	1.0	4.0	0.95	4.0	0.95	0.13	1.0	5.4	0.86
$ \Delta\phi^{\text{jet-rad1} - \text{jet-rad2}} $	10	1.4	1.0	4.0	0.95	2.4	0.99	0.25	1.0	5.2	0.88
$ \Delta\phi^{\text{toplep} - \text{jet-rad2}} $	7	1.3	0.99	3.2	0.86	2.0	0.96	0.46	1.0	4.1	0.77
$ \Delta\phi^{\text{tophad} - \text{jet-rad2}} $	7	1.2	0.99	3.2	0.87	2.1	0.96	0.46	1.0	4.1	0.77
$ \Delta\phi^{\text{jet-W1} - \text{jet-rad2}} $	10	1.3	1.0	3.8	0.95	2.4	0.99	0.22	1.0	5.1	0.88
$m^{\text{jet-rad1} - \text{jet-rad2}}$	9	6.2	0.72	6.7	0.66	2.6	0.98	4.2	0.90	8.8	0.45

Table 4: χ^2 values, number of degrees of freedom (NDF) and p -values for each observable and each prediction for the normalised differential cross-sections.

Prediction	PwG+PY8			PwG+Hw7		aMC@NLO+Hw7		SHERPA 2.2.12		PwG+PY8 MiNNLOPS	
	Observable	NDF	χ^2	p -value	χ^2	p -value	χ^2	p -value	χ^2	p -value	χ^2
$p_T^{\text{jet-W1}}$	9	12.0	0.21	16.0	0.074	13.0	0.19	19.0	0.024	14.0	0.13
$ y^{\text{jet-W1}} $	9	63.0	< 0.01	76.0	< 0.01	65.0	< 0.01	56.0	< 0.01	13.0	0.17
$p_T^{\text{jet-W2}}$	7	7.9	0.34	9.8	0.20	8.0	0.33	13.0	0.064	8.2	0.31
$ y^{\text{jet-W2}} $	9	134.0	< 0.01	220.0	< 0.01	219.0	< 0.01	103.0	< 0.01	25.0	< 0.01
$ \Delta y^{\text{jet-W1} - \text{jet-W2}} $	9	7.0	0.63	8.2	0.52	7.9	0.54	6.1	0.73	5.2	0.81
$ \Delta \phi^{\text{jet-W1} - \text{jet-W2}} $	9	9.5	0.39	12.0	0.21	13.0	0.17	11.0	0.25	8.7	0.47
$p_T^{\text{jet-rad1}}$	10	9.4	0.50	9.5	0.48	8.5	0.58	10.3	0.42	12.0	0.29
$ y^{\text{jet-rad1}} $	9	49.0	< 0.01	80.0	< 0.01	68.0	< 0.01	42.0	< 0.01	21.0	0.011
$ \Delta \phi^{\text{toplep} - \text{jet-rad1}} $	6	2.8	0.83	3.0	0.80	2.7	0.85	2.9	0.82	2.5	0.87
$ \Delta \phi^{\text{tophad} - \text{jet-rad1}} $	6	2.6	0.86	2.9	0.82	2.2	0.90	2.6	0.85	2.1	0.91
$ \Delta \phi^{\text{jet-W1} - \text{jet-rad1}} $	9	7.7	0.56	11.0	0.27	6.3	0.71	8.6	0.47	5.6	0.78
$m^{\text{t}\bar{\text{t}}} - \text{jet-rad1}$	7	9.1	0.24	9.8	0.20	7.9	0.35	7.8	0.35	8.2	0.31
$p_T^{\text{jet-rad2}}$	8	12.0	0.13	13.0	0.11	11.0	0.22	10.5	0.23	14.0	0.072
$ y^{\text{jet-rad2}} $	9	24.0	< 0.01	45.0	< 0.01	38.0	< 0.01	30.0	< 0.01	16.0	0.069
$ \Delta y^{\text{jet-rad1} - \text{jet-rad2}} $	9	5.6	0.78	15.0	0.090	7.7	0.57	5.9	0.75	6.4	0.70
$ \Delta \phi^{\text{jet-rad1} - \text{jet-rad2}} $	9	25.0	< 0.01	69.0	< 0.01	33.0	< 0.01	15.0	0.084	26.0	< 0.01
$ \Delta \phi^{\text{toplep} - \text{jet-rad2}} $	6	12.0	0.072	15.0	0.018	12.0	0.062	13.0	0.036	8.5	0.21
$ \Delta \phi^{\text{tophad} - \text{jet-rad2}} $	6	4.7	0.59	5.5	0.49	4.8	0.57	4.6	0.59	2.6	0.86
$ \Delta \phi^{\text{jet-W1} - \text{jet-rad2}} $	9	12.0	0.23	22.0	< 0.01	18.0	0.040	14.0	0.13	11.0	0.26
$m^{\text{jet-rad1} - \text{jet-rad2}}$	8	14.0	0.094	16.0	0.042	12.0	0.15	10.0	0.26	14.0	0.085

12 Summary and Conclusions

Measurements are presented of differential cross-sections at particle level for $t\bar{t}$ production in pp collisions at $\sqrt{s} = 13$ TeV using the ATLAS detector at the LHC with an integrated luminosity of 140 fb^{-1} of 2015–2018 data. The $t\bar{t}$ events are selected in the ℓ +jets final state. The measurements presented benefit from the large number of events available from the full Run 2 sample and a reduction of the systematic uncertainties compared to previous analyses.

Absolute and normalised differential cross-sections as functions of jet observables, including jet transverse momenta and rapidities, angular correlations and invariant masses, are measured in three channels: $t\bar{t}$ inclusive with $N^{\text{jets}} \geq 4$, $t\bar{t}+1\text{jet}$ with $N^{\text{jets}} \geq 5$ and $t\bar{t}+2\text{jets}$ with $N^{\text{jets}} \geq 6$. The observables, either constructed from the jets forming the $t\bar{t}$ system or arising from hard QCD radiation, are measured to characterise the kinematics, topology and dynamics of the $t\bar{t}$ system; they also prove to be sensitive to initial- and final-state QCD radiation effects, represented by the production of additional jets. Angular correlations between the top quarks and the additional jets, as well as between the jets, are measured for the first time.

The measured cross-section as a function of $p_{\text{T}}^{\text{jet-W1}}$ has a harder spectrum than that of $p_{\text{T}}^{\text{jet-W2}}$. The measured cross-sections as functions of $|y^{\text{jet-W1}}|$ and $|y^{\text{jet-W2}}|$ have very similar shape and normalisation. The measured cross-section as a function of $|\Delta y^{\text{jet-W1-jet-W2}}|$ ($|\Delta\phi^{\text{jet-W1-jet-W2}}|$) exhibits a peak around $|\Delta y^{\text{jet-W1-jet-W2}}| = 0$ ($|\Delta\phi^{\text{jet-W1-jet-W2}}| = 1$ rad). These observables characterise the kinematics of the two light jets forming the hadronically decaying top quark.

Values of $m^{t\bar{t}-\text{jet-rad1}}$ ($m^{\text{jet-rad1-jet-rad2}}$) up to ~ 5.3 TeV (~ 4 TeV) are measured. The measured cross-sections as functions of $m^{t\bar{t}-\text{jet-rad1}}$ and $m^{\text{jet-rad1-jet-rad2}}$ decrease by more than five orders of magnitude within the measured range. These observables characterise the dynamics of the first and second gluon emissions.

From the event topology point of view, differences between the shapes of the measured cross-sections as functions of the rapidities and angular correlations for the $t\bar{t}+1\text{jet}$ and $t\bar{t}+2\text{jets}$ channels and those measured in the $t\bar{t}$ inclusive channel indicate that the first and second gluon emissions tend to be more isotropic in rapidity than the jets forming the hadronically decaying top quark. This is supported by the measurements as functions of $|\Delta\phi^{\text{toplep-jet-rad1}}|$, $|\Delta\phi^{\text{tophad-jet-rad1}}|$, $|\Delta\phi^{\text{toplep-jet-rad2}}|$ and $|\Delta\phi^{\text{tophad-jet-rad2}}|$, which show that the first and second gluon emissions have a higher probability of arising at larger angles from the leptonically decaying top quark and that there are more events with a gluon emission back-to-back with the jets forming the leptonically decaying top. In addition, the measured features indicate that the second gluon emission tends to be close in rapidity to the first gluon emission and that there is a weak dependence on the difference in ϕ between the first and second gluon emissions.

Next-to-leading-order QCD predictions normalised to $\mathcal{O}(\text{NNLO+NNLL})$ describe well the shape and normalisation of the measured absolute differential cross-sections as functions of angular observables, but the transverse momentum and invariant mass observables are described well only at low values. For $p_{\text{T}}^{\text{jet-W1}}$, $p_{\text{T}}^{\text{jet-W2}}$ and $m^{\text{jet-rad1-jet-rad2}}$ ($p_{\text{T}}^{\text{jet-rad1}}$ and $p_{\text{T}}^{\text{jet-rad2}}$), the predictions from PWG+Hw7 (SHERPA 2.2.12) are closest to the data, whereas the prediction from aMC@NLO+Hw7 gives the best description of the measured cross-section as a function of $m^{t\bar{t}-\text{jet-rad1}}$. The same conclusions hold for the normalised differential cross-sections.

Recently, predictions for $t\bar{t}$ production at NNLO QCD have become available and the interface with the PS provided by PYTHIA via the MiNNLOPS matching scheme allows the computation of differential

cross-sections for jet observables such as those presented here. The NNLO predictions are compared with the measured cross-sections for the first time and provide a good description of the angular observables, though there is a tendency for the NNLO predictions to be below the data for $|\Delta y^{\text{jet-W1} - \text{jet-W2}}| > 3$. The description of the data by the NNLO prediction is somewhat worse than that at NLO for $p_T^{\text{jet-rad2}}$. For the transverse momentum and invariant mass observables, the NNLO QCD predictions provide a significant improvement in the description of the $p_T^{\text{jet-W1}}$, $p_T^{\text{jet-W2}}$, $p_T^{\text{jet-rad1}}$, $m^{t\bar{t} - \text{jet-rad1}}$ and $m^{\text{jet-rad1} - \text{jet-rad2}}$ observables relative to that of the NLO predictions.

The χ^2 and p -values calculated for each differential cross-section and each theoretical prediction confirm the qualitative conclusions.

Acknowledgements

We thank CERN for the very successful operation of the LHC and its injectors, as well as the support staff at CERN and at our institutions worldwide without whom ATLAS could not be operated efficiently.

The crucial computing support from all WLCG partners is acknowledged gratefully, in particular from CERN, the ATLAS Tier-1 facilities at TRIUMF/SFU (Canada), NDGF (Denmark, Norway, Sweden), CC-IN2P3 (France), KIT/GridKA (Germany), INFN-CNAF (Italy), NL-T1 (Netherlands), PIC (Spain), RAL (UK) and BNL (USA), the Tier-2 facilities worldwide and large non-WLCG resource providers. Major contributors of computing resources are listed in Ref. [114].

We gratefully acknowledge the support of ANPCyT, Argentina; YerPhI, Armenia; ARC, Australia; BMWFW and FWF, Austria; ANAS, Azerbaijan; CNPq and FAPESP, Brazil; NSERC, NRC and CFI, Canada; CERN; ANID, Chile; CAS, MOST and NSFC, China; Minciencias, Colombia; MEYS CR, Czech Republic; DNRF and DNSRC, Denmark; IN2P3-CNRS and CEA-DRF/IRFU, France; SRNSFG, Georgia; BMBF, HGF and MPG, Germany; GSRI, Greece; RGC and Hong Kong SAR, China; ISF and Benoziyo Center, Israel; INFN, Italy; MEXT and JSPS, Japan; CNRST, Morocco; NWO, Netherlands; RCN, Norway; MEiN, Poland; FCT, Portugal; MNE/IFA, Romania; MESTD, Serbia; MSSR, Slovakia; ARRS and MIZŠ, Slovenia; DSI/NRF, South Africa; MICINN, Spain; SRC and Wallenberg Foundation, Sweden; SERI, SNSF and Cantons of Bern and Geneva, Switzerland; MOST, Taipei; TENMAK, Türkiye; STFC, United Kingdom; DOE and NSF, United States of America.

Individual groups and members have received support from BCKDF, CANARIE, CRC and DRAC, Canada; CERN-CZ, PRIMUS 21/SCI/017 and UNCE SCI/013, Czech Republic; COST, ERC, ERDF, Horizon 2020, ICSC-NextGenerationEU and Marie Skłodowska-Curie Actions, European Union; Investissements d’Avenir Labex, Investissements d’Avenir Idex and ANR, France; DFG and AvH Foundation, Germany; Herakleitos, Thales and Aristeia programmes co-financed by EU-ESF and the Greek NSRF, Greece; BSF-NSF and MINERVA, Israel; Norwegian Financial Mechanism 2014-2021, Norway; NCN and NAWA, Poland; La Caixa Banking Foundation, CERCA Programme Generalitat de Catalunya and PROMETEO and GenT Programmes Generalitat Valenciana, Spain; Göran Gustafssons Stiftelse, Sweden; The Royal Society and Leverhulme Trust, United Kingdom.

In addition, individual members wish to acknowledge support from CERN: European Organization for Nuclear Research (CERN PJA5); Chile: Agencia Nacional de Investigación y Desarrollo (FONDECYT 1190886, FONDECYT 1210400, FONDECYT 1230812, FONDECYT 1230987); China: National Natural Science Foundation of China (NSFC - 12175119, NSFC 12275265, NSFC-12075060); Czech Republic: PRIMUS Research Programme (PRIMUS/21/SCI/017); EU: H2020 European Research Council (ERC -

101002463); European Union: European Research Council (ERC - 948254), Horizon 2020 Framework Programme (MUCCA - CHIST-ERA-19-XAI-00), European Union, Future Artificial Intelligence Research (FAIR-NextGenerationEU PE00000013), Italian Center for High Performance Computing, Big Data and Quantum Computing (ICSC, NextGenerationEU), Marie Skłodowska-Curie Actions (EU H2020 MSC IF GRANT NO 101033496); France: Agence Nationale de la Recherche (ANR-20-CE31-0013, ANR-21-CE31-0013, ANR-21-CE31-0022), Investissements d’Avenir Idex (ANR-11-LABX-0012), Investissements d’Avenir Labex (ANR-11-LABX-0012); Germany: Baden-Württemberg Stiftung (BW Stiftung-Postdoc Eliteprogramme), Deutsche Forschungsgemeinschaft (DFG - 469666862, DFG - CR 312/5-1); Italy: Istituto Nazionale di Fisica Nucleare (FELLINI G.A. n. 754496, ICSC, NextGenerationEU); Japan: Japan Society for the Promotion of Science (JSPS KAKENHI JP21H05085, JSPS KAKENHI JP22H01227, JSPS KAKENHI JP22H04944, JSPS KAKENHI JP22KK0227); Netherlands: Netherlands Organisation for Scientific Research (NWO Veni 2020 - VI.Veni.202.179); Norway: Research Council of Norway (RCN-314472); Poland: Polish National Agency for Academic Exchange (PPN/PPO/2020/1/00002/U/00001), Polish National Science Centre (NCN 2021/42/E/ST2/00350, NCN OPUS nr 2022/47/B/ST2/03059, NCN UMO-2019/34/E/ST2/00393, UMO-2020/37/B/ST2/01043, UMO-2021/40/C/ST2/00187); Slovenia: Slovenian Research Agency (ARIS grant J1-3010); Spain: BBVA Foundation (LEO22-1-603), Generalitat Valenciana (Artemisa, FEDER, IDIFEDER/2018/048), La Caixa Banking Foundation (LCF/BQ/PI20/11760025), Ministry of Science and Innovation (MCIN & NextGenEU PCI2022-135018-2, MICIN & FEDER PID2021-125273NB, RYC2019-028510-I, RYC2020-030254-I, RYC2021-031273-I, RYC2022-038164-I), PROMETEO and GenT Programmes Generalitat Valenciana (CIDEAGENT/2019/023, CIDEAGENT/2019/027); Sweden: Swedish Research Council (VR 2018-00482, VR 2022-03845, VR 2022-04683, VR grant 2021-03651), Knut and Alice Wallenberg Foundation (KAW 2017.0100, KAW 2018.0157, KAW 2018.0458, KAW 2019.0447); Switzerland: Swiss National Science Foundation (SNSF - PCEFP2_194658); United Kingdom: Leverhulme Trust (Leverhulme Trust RPG-2020-004); United States of America: U.S. Department of Energy (ECA DE-AC02-76SF00515), Neubauer Family Foundation.

References

- [1] ATLAS Collaboration, *Measurement of the top-quark mass using a leptonic invariant mass in pp collisions at $\sqrt{s} = 13$ TeV with the ATLAS detector*, [JHEP **06** \(2023\) 019](#), arXiv: [2209.00583 \[hep-ex\]](#).
- [2] CMS Collaboration, *Measurement of the top quark mass using a profile likelihood approach with the lepton+jets final states in proton-proton collisions at $\sqrt{s} = 13$ TeV*, [Eur. Phys. J. C **83** \(2023\) 963](#), arXiv: [2302.01967 \[hep-ex\]](#).
- [3] CMS Collaboration, *Measurement of $t\bar{t}$ normalised multi-differential cross sections in pp collisions at $\sqrt{s} = 13$ TeV, and simultaneous determination of the strong coupling strength, top quark pole mass, and parton distribution functions*, [Eur. Phys. J. C **80** \(2020\) 658](#), arXiv: [1904.05237 \[hep-ex\]](#).
- [4] ATLAS Collaboration, *Measurements of differential cross-sections in top-quark pair events with a high transverse momentum top quark and limits on beyond the Standard Model contributions to top-quark pair production with the ATLAS detector at $\sqrt{s} = 13$ TeV*, [JHEP **06** \(2022\) 063](#), arXiv: [2202.12134 \[hep-ex\]](#).

- [5] CMS Collaboration, *Search for physics beyond the standard model in top quark production with additional leptons in the context of effective field theory*, **JHEP** **12** (2023) 068, arXiv: [2307.15761 \[hep-ex\]](#).
- [6] ATLAS Collaboration, *Measurements of top quark pair relative differential cross-sections with ATLAS in pp collisions at $\sqrt{s} = 7$ TeV*, **Eur. Phys. J. C** **73** (2013) 2261, arXiv: [1207.5644 \[hep-ex\]](#).
- [7] ATLAS Collaboration, *Measurements of normalized differential cross sections for $t\bar{t}$ production in pp collisions at $\sqrt{s} = 7$ TeV using the ATLAS detector*, **Phys. Rev. D** **90** (2014) 072004, arXiv: [1407.0371 \[hep-ex\]](#).
- [8] ATLAS Collaboration, *Differential top-antitop cross-section measurements as a function of observables constructed from final-state particles using pp collisions at $\sqrt{s} = 7$ TeV in the ATLAS detector*, **JHEP** **06** (2015) 100, arXiv: [1502.05923 \[hep-ex\]](#).
- [9] ATLAS Collaboration, *Measurement of the differential cross-section of highly boosted top quarks as a function of their transverse momentum in $\sqrt{s} = 8$ TeV proton-proton collisions using the ATLAS detector*, **Phys. Rev. D** **93** (2016) 032009, arXiv: [1510.03818 \[hep-ex\]](#).
- [10] ATLAS Collaboration, *Measurements of top-quark pair differential cross-sections in the lepton+jets channel in pp collisions at $\sqrt{s} = 8$ TeV using the ATLAS detector*, **Eur. Phys. J. C** **76** (2016) 538, arXiv: [1511.04716 \[hep-ex\]](#).
- [11] ATLAS Collaboration, *Measurement of top quark pair differential cross sections in the dilepton channel in pp collisions at $\sqrt{s} = 7$ and 8 TeV with ATLAS*, **Phys. Rev. D** **94** (2016) 092003, arXiv: [1607.07281 \[hep-ex\]](#), Erratum: **Phys. Rev. D** **101** (2020) 119901.
- [12] ATLAS Collaboration, *Measurements of top-quark pair differential cross-sections in the $e\mu$ channel in pp collisions at $\sqrt{s} = 13$ TeV using the ATLAS detector*, **Eur. Phys. J. C** **77** (2017) 292, arXiv: [1612.05220 \[hep-ex\]](#).
- [13] ATLAS Collaboration, *Measurements of top-quark pair differential cross-sections in the lepton+jets channel in pp collisions at $\sqrt{s} = 13$ TeV using the ATLAS detector*, **JHEP** **11** (2017) 191, arXiv: [1708.00727 \[hep-ex\]](#).
- [14] ATLAS Collaboration, *Measurements of differential cross sections of top quark pair production in association with jets in pp collisions at $\sqrt{s} = 13$ TeV using the ATLAS detector*, **JHEP** **10** (2018) 159, arXiv: [1802.06572 \[hep-ex\]](#).
- [15] ATLAS Collaboration, *Measurements of inclusive and differential fiducial cross-sections of $t\bar{t}$ production with additional heavy-flavour jets in proton-proton collisions at $\sqrt{s} = 13$ TeV with the ATLAS detector*, **JHEP** **04** (2019) 046, arXiv: [1811.12113 \[hep-ex\]](#).
- [16] ATLAS Collaboration, *Measurements of top-quark pair single- and double-differential cross-sections in the all-hadronic channel in pp collisions at $\sqrt{s} = 13$ TeV using the ATLAS detector*, **JHEP** **01** (2021) 033, arXiv: [2006.09274 \[hep-ex\]](#).

- [17] ATLAS Collaboration, *Measurements of top-quark pair differential and double-differential cross-sections in the ℓ +jets channel with pp collisions at $\sqrt{s} = 13$ TeV using the ATLAS detector*, *Eur. Phys. J. C* **79** (2019) 1028, arXiv: [1908.07305 \[hep-ex\]](#),
Erratum: *Eur. Phys. J. C* **80** (2020) 1092.
- [18] CMS Collaboration, *Measurement of differential top-quark-pair production cross sections in pp collisions at $\sqrt{s} = 7$ TeV*, *Eur. Phys. J. C* **73** (2013) 2339, arXiv: [1211.2220 \[hep-ex\]](#).
- [19] CMS Collaboration, *Measurement of the differential cross section for top quark pair production in pp collisions at $\sqrt{s} = 8$ TeV*, *Eur. Phys. J. C* **75** (2015) 542, arXiv: [1505.04480 \[hep-ex\]](#).
- [20] CMS Collaboration, *Measurement of the differential cross sections for top quark pair production as a function of kinematic event variables in pp collisions at $\sqrt{s} = 7$ and 8 TeV*, *Phys. Rev. D* **94** (2016) 052006, arXiv: [1607.00837 \[hep-ex\]](#).
- [21] CMS Collaboration, *Measurement of the integrated and differential $t\bar{t}$ production cross sections for high- p_T top quarks in pp collisions at $\sqrt{s} = 8$ TeV*, *Phys. Rev. D* **94** (2016) 072002, arXiv: [1605.00116 \[hep-ex\]](#).
- [22] CMS Collaboration, *Measurement of double-differential cross sections for top quark pair production in pp collisions at $\sqrt{s} = 8$ TeV and impact on parton distribution functions*, *Eur. Phys. J. C* **77** (2017) 459, arXiv: [1703.01630 \[hep-ex\]](#).
- [23] CMS Collaboration, *Measurement of normalized differential $t\bar{t}$ cross sections in the dilepton channel from pp collisions at $\sqrt{s} = 13$ TeV*, *JHEP* **04** (2018) 060, arXiv: [1708.07638 \[hep-ex\]](#).
- [24] CMS Collaboration, *Measurement of differential cross sections for top quark pair production using the lepton+jets final state in proton–proton collisions at 13 TeV*, *Phys. Rev. D* **95** (2017) 092001, arXiv: [1610.04191 \[hep-ex\]](#).
- [25] CMS Collaboration, *Measurements of differential cross sections of top quark pair production as a function of kinematic event variables in proton–proton collisions at $\sqrt{s} = 13$ TeV*, *JHEP* **06** (2018) 002, arXiv: [1803.03991 \[hep-ex\]](#).
- [26] CMS Collaboration, *Measurement of differential cross sections for the production of top quark pairs and of additional jets in lepton+jets events from pp collisions at $\sqrt{s} = 13$ TeV*, *Phys. Rev. D* **97** (2018) 112003, arXiv: [1803.08856 \[hep-ex\]](#).
- [27] CMS Collaboration, *Measurements of $t\bar{t}$ differential cross sections in proton–proton collisions at $\sqrt{s} = 13$ TeV using events containing two leptons*, *JHEP* **02** (2019) 149, arXiv: [1811.06625 \[hep-ex\]](#).
- [28] CMS Collaboration, *Measurement of differential $t\bar{t}$ production cross sections using top quarks at large transverse momenta in pp collisions at $\sqrt{s} = 13$ TeV*, *Phys. Rev. D* **103** (2021) 052008, arXiv: [2008.07860 \[hep-ex\]](#).
- [29] L. Evans and P. Bryant, *LHC Machine*, *JINST* **3** (2008) S08001.
- [30] ATLAS Collaboration, *Further studies on simulation of top-quark production for the ATLAS experiment at $\sqrt{s} = 13$ TeV*, ATL-PHYS-PUB-2016-016, 2016, URL: <https://cds.cern.ch/record/2205262>.
- [31] ATLAS Collaboration, *Studies on top-quark Monte Carlo modelling for Top2016*, ATL-PHYS-PUB-2016-020, 2016, URL: <https://cds.cern.ch/record/2216168>.
- [32] ATLAS Collaboration, *Studies on top-quark Monte Carlo modelling with Sherpa and MG5_aMC@NLO*, ATL-PHYS-PUB-2017-007, 2017, URL: <https://cds.cern.ch/record/2261938>.

- [33] ATLAS Collaboration, *Improvements in $t\bar{t}$ modelling using NLO+PS Monte Carlo generators for Run 2*, ATL-PHYS-PUB-2018-009, 2018, URL: <https://cds.cern.ch/record/2630327>.
- [34] CMS Collaboration, *Extraction and validation of a new set of CMS PYTHIA8 tunes from underlying-event measurements*, *Eur. Phys. J. C* **80** (2020) 4, arXiv: [1903.12179](https://arxiv.org/abs/1903.12179) [[hep-ex](#)].
- [35] NNPDF Collaboration, R. D. Ball et al., *Parton distributions for the LHC run II*, *JHEP* **04** (2015) 040, arXiv: [1410.8849](https://arxiv.org/abs/1410.8849) [[hep-ph](#)].
- [36] ATLAS Collaboration, *The ATLAS Experiment at the CERN Large Hadron Collider*, *JINST* **3** (2008) S08003.
- [37] ATLAS Collaboration, *ATLAS Insertable B-Layer: Technical Design Report*, ATLAS-TDR-19, CERN-LHCC-2010-013, 2010, URL: <https://cds.cern.ch/record/1291633>, Addendum: ATLAS-TDR-19-ADD-1, CERN-LHCC-2012-009, 2012, URL: <https://cds.cern.ch/record/1451888>, 2019.
- [38] B. Abbott et al., *Production and integration of the ATLAS Insertable B-Layer*, *JINST* **13** (2018) T05008, arXiv: [1803.00844](https://arxiv.org/abs/1803.00844) [[physics.ins-det](#)].
- [39] ATLAS Collaboration, *Performance of the ATLAS trigger system in 2015*, *Eur. Phys. J. C* **77** (2017) 317, arXiv: [1611.09661](https://arxiv.org/abs/1611.09661) [[hep-ex](#)].
- [40] ATLAS Collaboration, *Software and computing for Run 3 of the ATLAS experiment at the LHC*, 2024, arXiv: [2404.06335](https://arxiv.org/abs/2404.06335) [[hep-ex](#)].
- [41] ATLAS Collaboration, *ATLAS data quality operations and performance for 2015–2018 data-taking*, *JINST* **15** (2020) P04003, arXiv: [1911.04632](https://arxiv.org/abs/1911.04632) [[physics.ins-det](#)].
- [42] ATLAS Collaboration, *Luminosity determination in pp collisions at $\sqrt{s} = 13$ TeV using the ATLAS detector at the LHC*, *Eur. Phys. J. C* **83** (2023) 982, arXiv: [2212.09379](https://arxiv.org/abs/2212.09379) [[hep-ex](#)].
- [43] G. Avoni et al., *The new LUCID-2 detector for luminosity measurement and monitoring in ATLAS*, *JINST* **13** (2018) P07017.
- [44] ATLAS Collaboration, *The ATLAS Simulation Infrastructure*, *Eur. Phys. J. C* **70** (2010) 823, arXiv: [1005.4568](https://arxiv.org/abs/1005.4568) [[physics.ins-det](#)].
- [45] S. Agostinelli et al., *GEANT4—a simulation toolkit*, *Nucl. Instrum. Meth. A* **506** (2003) 250.
- [46] T. Sjöstrand, S. Mrenna and P. Skands, *A brief introduction to PYTHIA 8.1*, *Comput. Phys. Commun.* **178** (2008) 852, arXiv: [0710.3820](https://arxiv.org/abs/0710.3820) [[hep-ph](#)].
- [47] ATLAS Collaboration, *The Pythia 8 A3 tune description of ATLAS minimum bias and inelastic measurements incorporating the Donnachie-Landshoff diffractive model*, ATL-PHYS-PUB-2016-017, 2016, URL: <https://cds.cern.ch/record/2206965>.
- [48] J. Gao, C. S. Li and H. X. Zhu, *Top-Quark Decay at Next-to-Next-to-Leading Order in QCD*, *Phys. Rev. Lett.* **110** (2013) 042001, arXiv: [1210.2808](https://arxiv.org/abs/1210.2808) [[hep-ph](#)].
- [49] S. Frixione, G. Ridolfi and P. Nason, *A positive-weight next-to-leading-order Monte Carlo for heavy flavour hadroproduction*, *JHEP* **09** (2007) 126, arXiv: [0707.3088](https://arxiv.org/abs/0707.3088) [[hep-ph](#)].

- [50] P. Nason, *A new method for combining NLO QCD with shower Monte Carlo algorithms*, *JHEP* **11** (2004) 040, arXiv: [hep-ph/0409146](#).
- [51] S. Frixione, P. Nason and C. Oleari, *Matching NLO QCD computations with parton shower simulations: the POWHEG method*, *JHEP* **11** (2007) 070, arXiv: [0709.2092 \[hep-ph\]](#).
- [52] S. Alioli, P. Nason, C. Oleari and E. Re, *A general framework for implementing NLO calculations in shower Monte Carlo programs: the POWHEG BOX*, *JHEP* **06** (2010) 043, arXiv: [1002.2581 \[hep-ph\]](#).
- [53] T. Sjöstrand et al., *An introduction to PYTHIA 8.2*, *Comput. Phys. Commun.* **191** (2015) 159, arXiv: [1410.3012 \[hep-ph\]](#).
- [54] NNPDF Collaboration, R. D. Ball et al., *Parton distributions with LHC data*, *Nucl. Phys. B* **867** (2013) 244, arXiv: [1207.1303 \[hep-ph\]](#).
- [55] ATLAS Collaboration, *ATLAS Pythia 8 tunes to 7 TeV data*, ATL-PHYS-PUB-2014-021, 2014, URL: <https://cds.cern.ch/record/1966419>.
- [56] J. Bellm et al., *Herwig 7.0/Herwig++ 3.0 release note*, *Eur. Phys. J. C* **76** (2016) 196, arXiv: [1512.01178 \[hep-ph\]](#).
- [57] M. Bähr et al., *Herwig++ physics and manual*, *Eur. Phys. J. C* **58** (2008) 639, arXiv: [0803.0883 \[hep-ph\]](#).
- [58] M. H. Seymour and A. Siódmok, *Constraining MPI models using σ_{eff} and recent Tevatron and LHC Underlying Event data*, *JHEP* **10** (2013) 113, arXiv: [1307.5015 \[hep-ph\]](#).
- [59] L. A. Harland-Lang, A. D. Martin, P. Motylinski and R. S. Thorne, *Parton distributions in the LHC era: MMHT 2014 PDFs*, *Eur. Phys. J. C* **75** (2015) 204, arXiv: [1412.3989 \[hep-ph\]](#).
- [60] J. Alwall et al., *The automated computation of tree-level and next-to-leading order differential cross sections, and their matching to parton shower simulations*, *JHEP* **07** (2014) 079, arXiv: [1405.0301 \[hep-ph\]](#).
- [61] E. Bothmann et al., *Event generation with Sherpa 2.2*, *SciPost Phys.* **7** (2019) 034, arXiv: [1905.09127 \[hep-ph\]](#).
- [62] S. Höche, F. Krauss, M. Schönherr and F. Siegert, *QCD matrix elements + parton showers. The NLO case*, *JHEP* **04** (2013) 027, arXiv: [1207.5030 \[hep-ph\]](#).
- [63] T. Gleisberg and S. Höche, *Comix, a new matrix element generator*, *JHEP* **12** (2008) 039, arXiv: [0808.3674 \[hep-ph\]](#).
- [64] F. Buccioni et al., *OpenLoops 2*, *Eur. Phys. J. C* **79** (2019) 866, arXiv: [1907.13071 \[hep-ph\]](#).
- [65] F. Cascioli, P. Maierhöfer and S. Pozzorini, *Scattering Amplitudes with Open Loops*, *Phys. Rev. Lett.* **108** (2012) 111601, arXiv: [1111.5206 \[hep-ph\]](#).
- [66] A. Denner, S. Dittmaier and L. Hofer, *COLLIER: A fortran-based complex one-loop library in extended regularizations*, *Comput. Phys. Commun.* **212** (2017) 220, arXiv: [1604.06792 \[hep-ph\]](#).

- [67] S. Schumann and F. Krauss,
A parton shower algorithm based on Catani-Seymour dipole factorisation, *JHEP* **03** (2008) 038,
arXiv: [0709.1027 \[hep-ph\]](#).
- [68] M. Czakon and A. Mitov,
Top++: A program for the calculation of the top-pair cross-section at hadron colliders,
Comput. Phys. Commun. **185** (2014) 2930, arXiv: [1112.5675 \[hep-ph\]](#).
- [69] M. Beneke, P. Falgari, S. Klein and C. Schwinn,
Hadronic top-quark pair production with NNLL threshold resummation,
Nucl. Phys. B **855** (2012) 695, arXiv: [1109.1536 \[hep-ph\]](#).
- [70] M. Cacciari, M. Czakon, M. Mangano, A. Mitov and P. Nason, *Top-pair production at hadron colliders with next-to-next-to-leading logarithmic soft-gluon resummation*,
Phys. Lett. B **710** (2012) 612, arXiv: [1111.5869 \[hep-ph\]](#).
- [71] P. Bärnreuther, M. Czakon and A. Mitov, *Percent-Level-Precision Physics at the Tevatron: Next-to-Next-to-Leading Order QCD Corrections to $q\bar{q} \rightarrow t\bar{t}+X$* ,
Phys. Rev. Lett. **109** (2012) 132001, arXiv: [1204.5201 \[hep-ph\]](#).
- [72] M. Czakon and A. Mitov, *NNLO corrections to top-pair production at hadron colliders: the all-fermionic scattering channels*, *JHEP* **12** (2012) 054, arXiv: [1207.0236 \[hep-ph\]](#).
- [73] M. Czakon and A. Mitov,
NNLO corrections to top pair production at hadron colliders: the quark-gluon reaction,
JHEP **01** (2013) 080, arXiv: [1210.6832 \[hep-ph\]](#).
- [74] M. Czakon, P. Fiedler and A. Mitov,
Total Top-Quark Pair-Production Cross Section at Hadron Colliders Through $O(\alpha_s^4)$,
Phys. Rev. Lett. **110** (2013) 252004, arXiv: [1303.6254 \[hep-ph\]](#).
- [75] J. Butterworth et al., *PDF4LHC recommendations for LHC Run II*, *J. Phys. G* **43** (2016) 023001,
arXiv: [1510.03865 \[hep-ph\]](#).
- [76] A. D. Martin, W. J. Stirling, R. S. Thorne and G. Watt,
Uncertainties on α_s in global PDF analyses and implications for predicted hadronic cross sections,
Eur. Phys. J. C **64** (2009) 653, arXiv: [0905.3531 \[hep-ph\]](#).
- [77] H.-L. Lai et al., *New parton distributions for collider physics*, *Phys. Rev. D* **82** (2010) 074024,
arXiv: [1007.2241 \[hep-ph\]](#).
- [78] J. Mazzitelli et al.,
Next-to-Next-to-Leading Order Event Generation for Top-Quark Pair Production,
Phys. Rev. Lett. **127** (2021) 062001, arXiv: [2012.14267 \[hep-ph\]](#).
- [79] A. Ablat et al., *Exploring the impact of high-precision top-quark pair production data on the structure of the proton at the LHC*, *Phys. Rev. D* **109** (2024) 054027,
arXiv: [2307.11153 \[hep-ph\]](#).
- [80] S. Frixione, E. Laenen, P. Motylinski, C. White and B. R. Webber,
Single-top hadroproduction in association with a W boson, *JHEP* **07** (2008) 029,
arXiv: [0805.3067 \[hep-ph\]](#).
- [81] N. Kidonakis, *Next-to-next-to-leading-order collinear and soft gluon corrections for t-channel single top quark production*, *Phys. Rev. D* **83** (2011) 091503, arXiv: [1103.2792 \[hep-ph\]](#).

- [82] N. Kidonakis, *Two-loop soft anomalous dimensions for single top quark associated production with a W^- or H^-* , *Phys. Rev. D* **82** (2010) 054018, arXiv: [1005.4451 \[hep-ph\]](#).
- [83] N. Kidonakis, *Next-to-next-to-leading logarithm resummation for s-channel single top quark production*, *Phys. Rev. D* **81** (2010) 054028, arXiv: [1001.5034 \[hep-ph\]](#).
- [84] M. Aliev et al., *HATHOR - HAdronic Top and Heavy quarks crOss section calculatoR*, *Comput. Phys. Commun.* **182** (2011) 1034, arXiv: [1007.1327 \[hep-ph\]](#).
- [85] P. Kant et al., *HatHor for single top-quark production: Updated predictions and uncertainty estimates for single top-quark production in hadronic collisions*, *Comput. Phys. Commun.* **191** (2015) 74, arXiv: [1406.4403 \[hep-ph\]](#).
- [86] E. Re, *Single-top Wt -channel production matched with parton showers using the POWHEG method*, *Eur. Phys. J. C* **71** (2011) 1547, arXiv: [1009.2450 \[hep-ph\]](#).
- [87] C. Anastasiou, L. Dixon, K. Melnikov and F. Petriello, *High-precision QCD at hadron colliders: Electroweak gauge boson rapidity distributions at next-to-next-to leading order*, *Phys. Rev. D* **69** (2004) 094008, arXiv: [hep-ph/0312266](#).
- [88] D. de Florian et al., *Handbook of LHC Higgs Cross Sections: 4. Deciphering the Nature of the Higgs Sector*, 2016, arXiv: [1610.07922 \[hep-ph\]](#).
- [89] ATLAS Collaboration, *Vertex Reconstruction Performance of the ATLAS Detector at $\sqrt{s} = 13$ TeV*, ATL-PHYS-PUB-2015-026, 2015, URL: <https://cds.cern.ch/record/2037717>.
- [90] ATLAS Collaboration, *Electron and photon performance measurements with the ATLAS detector using the 2015–2017 LHC proton–proton collision data*, *JINST* **14** (2019) P12006, arXiv: [1908.00005 \[hep-ex\]](#).
- [91] ATLAS Collaboration, *Muon reconstruction and identification efficiency in ATLAS using the full Run 2 pp collision data set at $\sqrt{s} = 13$ TeV*, *Eur. Phys. J. C* **81** (2021) 578, arXiv: [2012.00578 \[hep-ex\]](#).
- [92] M. Cacciari, G. P. Salam and G. Soyez, *The anti- k_t jet clustering algorithm*, *JHEP* **04** (2008) 063, arXiv: [0802.1189 \[hep-ph\]](#).
- [93] M. Cacciari, G. P. Salam and G. Soyez, *FastJet user manual*, *Eur. Phys. J. C* **72** (2012) 1896, arXiv: [1111.6097 \[hep-ph\]](#).
- [94] ATLAS Collaboration, *Jet reconstruction and performance using particle flow with the ATLAS Detector*, *Eur. Phys. J. C* **77** (2017) 466, arXiv: [1703.10485 \[hep-ex\]](#).
- [95] M. Cacciari, G. P. Salam and G. Soyez, *The catchment area of jets*, *JHEP* **04** (2008) 005, arXiv: [0802.1188 \[hep-ph\]](#).
- [96] ATLAS Collaboration, *Performance of pile-up mitigation techniques for jets in pp collisions at $\sqrt{s} = 8$ TeV using the ATLAS detector*, *Eur. Phys. J. C* **76** (2016) 581, arXiv: [1510.03823 \[hep-ex\]](#).
- [97] ATLAS Collaboration, *Jet energy scale and resolution measured in proton–proton collisions at $\sqrt{s} = 13$ TeV with the ATLAS detector*, *Eur. Phys. J. C* **81** (2021) 689, arXiv: [2007.02645 \[hep-ex\]](#).

- [98] ATLAS Collaboration, *Optimisation and performance studies of the ATLAS b-tagging algorithms for the 2017-18 LHC run*, ATL-PHYS-PUB-2017-013, 2017, URL: <https://cds.cern.ch/record/2273281>.
- [99] ATLAS Collaboration, *The performance of missing transverse momentum reconstruction and its significance with the ATLAS detector using 140 fb^{-1} of $\sqrt{s} = 13\text{ TeV}$ pp collisions*, 2024, arXiv: [2402.05858](https://arxiv.org/abs/2402.05858) [hep-ex].
- [100] ATLAS Collaboration, *Performance of electron and photon triggers in ATLAS during LHC Run 2*, *Eur. Phys. J. C* **80** (2020) 47, arXiv: [1909.00761](https://arxiv.org/abs/1909.00761) [hep-ex].
- [101] ATLAS Collaboration, *Performance of the ATLAS muon triggers in Run 2*, *JINST* **15** (2020) P09015, arXiv: [2004.13447](https://arxiv.org/abs/2004.13447) [physics.ins-det].
- [102] ATLAS Collaboration, *Tools for estimating fake/non-prompt lepton backgrounds with the ATLAS detector at the LHC*, *JINST* **18** (2023) T11004, arXiv: [2211.16178](https://arxiv.org/abs/2211.16178) [hep-ex].
- [103] G. D'Agostini, *A multidimensional unfolding method based on Bayes' theorem*, *Nucl. Instrum. Meth. A* **362** (1995) 487.
- [104] T. Adye, *Unfolding algorithms and tests using RooUnfold*, 2011, arXiv: [1105.1160](https://arxiv.org/abs/1105.1160) [physics.data-an].
- [105] ATLAS Collaboration, *ATLAS b-jet identification performance and efficiency measurement with $t\bar{t}$ events in pp collisions at $\sqrt{s} = 13\text{ TeV}$* , *Eur. Phys. J. C* **79** (2019) 970, arXiv: [1907.05120](https://arxiv.org/abs/1907.05120) [hep-ex].
- [106] ATLAS Collaboration, *Measurement of the c-jet mistagging efficiency in $t\bar{t}$ events using pp collision data at $\sqrt{s} = 13\text{ TeV}$ collected with the ATLAS detector*, *Eur. Phys. J. C* **82** (2022) 95, arXiv: [2109.10627](https://arxiv.org/abs/2109.10627) [hep-ex].
- [107] ATLAS Collaboration, *Calibration of the light-flavour jet mistagging efficiency of the b-tagging algorithms with Z+jets events using 139 fb^{-1} of ATLAS proton-proton collision data at $\sqrt{s} = 13\text{ TeV}$* , *Eur. Phys. J. C* **83** (2023) 728, arXiv: [2301.06319](https://arxiv.org/abs/2301.06319) [hep-ex].
- [108] ATLAS Collaboration, *Electron and photon energy calibration with the ATLAS detector using LHC Run 2 data*, *JINST* **19** (2023) P02009, arXiv: [2309.05471](https://arxiv.org/abs/2309.05471) [hep-ex].
- [109] ATLAS Collaboration, *Studies of the muon momentum calibration and performance of the ATLAS detector with pp collisions at $\sqrt{s} = 13\text{ TeV}$* , *Eur. Phys. J. C* **83** (2023) 686, arXiv: [2212.07338](https://arxiv.org/abs/2212.07338) [hep-ex].
- [110] ATLAS Collaboration, *Electron and photon efficiencies in LHC Run 2 with the ATLAS experiment*, *JHEP* **05** (2024) 162, arXiv: [2308.13362](https://arxiv.org/abs/2308.13362) [hep-ex].
- [111] ATLAS Collaboration, *Determination of the parton distribution functions of the proton using diverse ATLAS data from pp collisions at $\sqrt{s} = 7, 8$ and 13 TeV* , *Eur. Phys. J. C* **82** (2022) 438, arXiv: [2112.11266](https://arxiv.org/abs/2112.11266) [hep-ex].
- [112] J. Pumplin et al., *Uncertainties of predictions from parton distribution functions. II. The Hessian method*, *Phys. Rev. D* **65** (2001) 014013, arXiv: [hep-ph/0101032](https://arxiv.org/abs/hep-ph/0101032).

- [113] F. James and M. Roos,
Minuit - a system for function minimization and analysis of the parameter errors and correlations,
Comput. Phys. Commun. **10** (1975) 343.
- [114] ATLAS Collaboration, *ATLAS Computing Acknowledgements*, ATL-SOFT-PUB-2023-001, 2023,
URL: <https://cds.cern.ch/record/2869272>.

The ATLAS Collaboration

G. Aad ¹⁰², B. Abbott ¹²⁰, K. Abeling ⁵⁵, N.J. Abicht ⁴⁹, S.H. Abidi ²⁹, A. Aboulhorma ^{35e}, H. Abramowicz ¹⁵¹, H. Abreu ¹⁵⁰, Y. Abulaiti ¹¹⁷, B.S. Acharya ^{69a,69b,m}, C. Adam Bourdarios ⁴, L. Adamczyk ^{86a}, S.V. Addepalli ²⁶, M.J. Addison ¹⁰¹, J. Adelman ¹¹⁵, A. Adiguzel ^{21c}, T. Adye ¹³⁴, A.A. Affolder ¹³⁶, Y. Afik ³⁹, M.N. Agaras ¹³, J. Agarwala ^{73a,73b}, A. Aggarwal ¹⁰⁰, C. Agheorghiesei ^{27c}, A. Ahmad ³⁶, F. Ahmadov ^{38,z}, W.S. Ahmed ¹⁰⁴, S. Ahuja ⁹⁵, X. Ai ^{62e}, G. Aielli ^{76a,76b}, A. Aikot ¹⁶³, M. Ait Tamlihat ^{35e}, B. Aitbenchikh ^{35a}, I. Aizenberg ¹⁶⁹, M. Akbiyik ¹⁰⁰, T.P.A. Åkesson ⁹⁸, A.V. Akimov ³⁷, D. Akiyama ¹⁶⁸, N.N. Akolkar ²⁴, S. Aktas ^{21a}, K. Al Houry ⁴¹, G.L. Alberghi ^{23b}, J. Albert ¹⁶⁵, P. Albicocco ⁵³, G.L. Albouy ⁶⁰, S. Alderweireldt ⁵², Z.L. Alegria ¹²¹, M. Aleksa ³⁶, I.N. Aleksandrov ³⁸, C. Alexa ^{27b}, T. Alexopoulos ¹⁰, F. Alfonsi ^{23b}, M. Algren ⁵⁶, M. Alhroob ¹²⁰, B. Ali ¹³², H.M.J. Ali ⁹¹, S. Ali ¹⁴⁸, S.W. Alibocus ⁹², M. Aliev ^{33c}, G. Alimonti ^{71a}, W. Alkakhki ⁵⁵, C. Allaire ⁶⁶, B.M.M. Allbrooke ¹⁴⁶, J.F. Allen ⁵², C.A. Allendes Flores ^{137f}, P.P. Allport ²⁰, A. Aloisio ^{72a,72b}, F. Alonso ⁹⁰, C. Alpigiani ¹³⁸, M. Alvarez Estevez ⁹⁹, A. Alvarez Fernandez ¹⁰⁰, M. Alves Cardoso ⁵⁶, M.G. Alviggi ^{72a,72b}, M. Aly ¹⁰¹, Y. Amaral Coutinho ^{83b}, A. Ambler ¹⁰⁴, C. Amelung ³⁶, M. Amerl ¹⁰¹, C.G. Ames ¹⁰⁹, D. Amidei ¹⁰⁶, S.P. Amor Dos Santos ^{130a}, K.R. Amos ¹⁶³, V. Ananiev ¹²⁵, C. Anastopoulos ¹³⁹, T. Andeen ¹¹, J.K. Anders ³⁶, S.Y. Andreev ^{47a,47b}, A. Andreatta ^{71a,71b}, S. Angelidakis ⁹, A. Angerami ^{41,ac}, A.V. Anisenkov ³⁷, A. Annovi ^{74a}, C. Antel ⁵⁶, M.T. Anthony ¹³⁹, E. Antipov ¹⁴⁵, M. Antonelli ⁵³, F. Anulli ^{75a}, M. Aoki ⁸⁴, T. Aoki ¹⁵³, J.A. Aparisi Pozo ¹⁶³, M.A. Aparo ¹⁴⁶, L. Aperio Bella ⁴⁸, C. Appelt ¹⁸, A. Apyan ²⁶, S.J. Arbiol Val ⁸⁷, C. Arcangeletti ⁵³, A.T.H. Arce ⁵¹, E. Arena ⁹², J-F. Arguin ¹⁰⁸, S. Argyropoulos ⁵⁴, J.-H. Arling ⁴⁸, O. Arnaez ⁴, H. Arnold ¹¹⁴, G. Artoni ^{75a,75b}, H. Asada ¹¹¹, K. Asai ¹¹⁸, S. Asai ¹⁵³, N.A. Asbah ⁶¹, K. Assamagan ²⁹, R. Astalos ^{28a}, S. Atashi ¹⁵⁹, R.J. Atkin ^{33a}, M. Atkinson ¹⁶², H. Atmani ^{35f}, P.A. Atmasiddha ¹²⁸, K. Augsten ¹³², S. Auricchio ^{72a,72b}, A.D. Auriol ²⁰, V.A. Austrup ¹⁰¹, G. Avolio ³⁶, K. Axiotis ⁵⁶, G. Azuelos ^{108,ag}, D. Babal ^{28b}, H. Bachacou ¹³⁵, K. Bachas ^{152,q}, A. Bachiu ³⁴, F. Backman ^{47a,47b}, A. Badea ³⁹, T.M. Baer ¹⁰⁶, P. Bagnaia ^{75a,75b}, M. Bahmani ¹⁸, D. Bahner ⁵⁴, A.J. Bailey ¹⁶³, V.R. Bailey ¹⁶², J.T. Baines ¹³⁴, L. Baines ⁹⁴, O.K. Baker ¹⁷², E. Bakos ¹⁵, D. Bakshi Gupta ⁸, V. Balakrishnan ¹²⁰, R. Balasubramanian ¹¹⁴, E.M. Baldin ³⁷, P. Balek ^{86a}, E. Ballabene ^{23b,23a}, F. Balli ¹³⁵, L.M. Baltes ^{63a}, W.K. Balunas ³², J. Balz ¹⁰⁰, E. Banas ⁸⁷, M. Bandieramonte ¹²⁹, A. Bandyopadhyay ²⁴, S. Bansal ²⁴, L. Barak ¹⁵¹, M. Barakat ⁴⁸, E.L. Barberio ¹⁰⁵, D. Barberis ^{57b,57a}, M. Barbero ¹⁰², M.Z. Barel ¹¹⁴, K.N. Barends ^{33a}, T. Barillari ¹¹⁰, M-S. Barisits ³⁶, T. Barklow ¹⁴³, P. Baron ¹²², D.A. Baron Moreno ¹⁰¹, A. Baroncelli ^{62a}, G. Barone ²⁹, A.J. Barr ¹²⁶, J.D. Barr ⁹⁶, F. Barreiro ⁹⁹, J. Barreiro Guimarães da Costa ^{14a}, U. Barron ¹⁵¹, M.G. Barros Teixeira ^{130a}, S. Barsov ³⁷, F. Bartels ^{63a}, R. Bartoldus ¹⁴³, A.E. Barton ⁹¹, P. Bartos ^{28a}, A. Basan ¹⁰⁰, M. Baselga ⁴⁹, A. Bassalat ^{66,b}, M.J. Basso ^{156a}, C.R. Basson ¹⁰¹, R.L. Bates ⁵⁹, S. Batlamous ^{35e}, J.R. Batley ³², B. Batool ¹⁴¹, M. Battaglia ¹³⁶, D. Battulga ¹⁸, M. Bause ^{75a,75b}, M. Bauer ³⁶, P. Bauer ²⁴, L.T. Bazzano Hurrell ³⁰, J.B. Beacham ⁵¹, T. Beau ¹²⁷, J.Y. Beaucamp ⁹⁰, P.H. Beauchemin ¹⁵⁸, P. Bechtel ²⁴, H.P. Beck ^{19,p}, K. Becker ¹⁶⁷, A.J. Beddall ⁸², V.A. Bednyakov ³⁸, C.P. Bee ¹⁴⁵, L.J. Beemster ¹⁵, T.A. Beermann ³⁶, M. Begalli ^{83d}, M. Begel ²⁹, A. Behera ¹⁴⁵, J.K. Behr ⁴⁸, J.F. Beirer ³⁶, F. Beisiegel ²⁴, M. Belfkir ^{116b}, G. Bella ¹⁵¹, L. Bellagamba ^{23b}, A. Bellerive ³⁴, P. Bellos ²⁰, K. Beloborodov ³⁷, D. Bencheikroun ^{35a}, F. Bendebba ^{35a}, Y. Benhammou ¹⁵¹, S. Bentvelsen ¹¹⁴, L. Beresford ⁴⁸, M. Beretta ⁵³, E. Bergeas Kuutmann ¹⁶¹, N. Berger ⁴, B. Bergmann ¹³², J. Beringer ^{17a},

G. Bernardi ⁵, C. Bernius ¹⁴³, F.U. Bernlochner ²⁴, F. Bernon ^{36,102}, A. Berrocal Guardia ¹³, T. Berry ⁹⁵, P. Berta ¹³³, A. Berthold ⁵⁰, I.A. Bertram ⁹¹, S. Bethke ¹¹⁰, A. Betti ^{75a,75b}, A.J. Bevan ⁹⁴, N.K. Bhalla ⁵⁴, M. Bhamjee ^{33c}, S. Bhatta ¹⁴⁵, D.S. Bhattacharya ¹⁶⁶, P. Bhattarai ¹⁴³, K.D. Bhide ⁵⁴, V.S. Bhopatkar ¹²¹, R.M. Bianchi ¹²⁹, G. Bianco ^{23b,23a}, O. Biebel ¹⁰⁹, R. Bielski ¹²³, M. Biglietti ^{77a}, M. Bindi ⁵⁵, A. Bingul ^{21b}, C. Bini ^{75a,75b}, A. Biondini ⁹², C.J. Birch-sykes ¹⁰¹, G.A. Bird ^{32,134}, M. Birman ¹⁶⁹, M. Biroš ¹³³, S. Biryukov ¹⁴⁶, T. Bisanz ⁴⁹, E. Bisceglie ^{43b,43a}, J.P. Biswal ¹³⁴, D. Biswas ¹⁴¹, K. Bjørke ¹²⁵, I. Bloch ⁴⁸, A. Blue ⁵⁹, U. Blumenschein ⁹⁴, J. Blumenthal ¹⁰⁰, G.J. Bobbink ¹¹⁴, V.S. Bobrovnikov ³⁷, M. Boehler ⁵⁴, B. Boehm ¹⁶⁶, D. Bogavac ³⁶, A.G. Bogdanchikov ³⁷, C. Bohm ^{47a}, V. Boisvert ⁹⁵, P. Bokan ³⁶, T. Bold ^{86a}, M. Bomben ⁵, M. Bona ⁹⁴, M. Boonekamp ¹³⁵, C.D. Booth ⁹⁵, A.G. Borbély ⁵⁹, I.S. Bordulev ³⁷, H.M. Borecka-Bielska ¹⁰⁸, G. Borissov ⁹¹, D. Bortoletto ¹²⁶, D. Boscherini ^{23b}, M. Bosman ¹³, J.D. Bossio Sola ³⁶, K. Bouaouda ^{35a}, N. Bouchhar ¹⁶³, J. Boudreau ¹²⁹, E.V. Bouhova-Thacker ⁹¹, D. Boumediene ⁴⁰, R. Bouquet ¹⁶⁵, A. Boveia ¹¹⁹, J. Boyd ³⁶, D. Boye ²⁹, I.R. Boyko ³⁸, J. Bracinik ²⁰, N. Brahimi ^{62d}, G. Brandt ¹⁷¹, O. Brandt ³², F. Braren ⁴⁸, B. Brau ¹⁰³, J.E. Brau ¹²³, R. Brenner ¹⁶⁹, L. Brenner ¹¹⁴, R. Brenner ¹⁶¹, S. Bressler ¹⁶⁹, D. Britton ⁵⁹, D. Britzger ¹¹⁰, I. Brock ²⁴, G. Brooijmans ⁴¹, W.K. Brooks ^{137f}, E. Brost ²⁹, L.M. Brown ¹⁶⁵, L.E. Bruce ⁶¹, T.L. Bruckler ¹²⁶, P.A. Bruckman de Renstrom ⁸⁷, B. Brüers ⁴⁸, A. Bruni ^{23b}, G. Bruni ^{23b}, M. Bruschi ^{23b}, N. Bruscino ^{75a,75b}, T. Buanes ¹⁶, Q. Buat ¹³⁸, D. Buchin ¹¹⁰, A.G. Buckley ⁵⁹, O. Bulekov ³⁷, B.A. Bullard ¹⁴³, S. Burdin ⁹², C.D. Burgard ⁴⁹, A.M. Burger ⁴⁰, B. Burghgrave ⁸, O. Burlayenko ⁵⁴, J.T.P. Burr ³², C.D. Burton ¹¹, J.C. Burzynski ¹⁴², E.L. Busch ⁴¹, V. Büscher ¹⁰⁰, P.J. Bussey ⁵⁹, J.M. Butler ²⁵, C.M. Buttar ⁵⁹, J.M. Butterworth ⁹⁶, W. Buttinger ¹³⁴, C.J. Buxo Vazquez ¹⁰⁷, A.R. Buzykaev ³⁷, S. Cabrera Urbán ¹⁶³, L. Cadamuro ⁶⁶, D. Caforio ⁵⁸, H. Cai ¹²⁹, Y. Cai ^{14a,14e}, Y. Cai ^{14c}, V.M.M. Cairo ³⁶, O. Cakir ^{3a}, N. Calace ³⁶, P. Calafiura ^{17a}, G. Calderini ¹²⁷, P. Calfayan ⁶⁸, G. Callea ⁵⁹, L.P. Caloba ^{83b}, D. Calvet ⁴⁰, S. Calvet ⁴⁰, M. Calvetti ^{74a,74b}, R. Camacho Toro ¹²⁷, S. Camarda ³⁶, D. Camarero Munoz ²⁶, P. Camarri ^{76a,76b}, M.T. Camerlingo ^{72a,72b}, D. Cameron ³⁶, C. Camincher ¹⁶⁵, M. Campanelli ⁹⁶, A. Camplani ⁴², V. Canale ^{72a,72b}, J. Cantero ¹⁶³, Y. Cao ¹⁶², F. Capocasa ²⁶, M. Capua ^{43b,43a}, A. Carbone ^{71a,71b}, R. Cardarelli ^{76a}, J.C.J. Cardenas ⁸, F. Cardillo ¹⁶³, G. Carducci ^{43b,43a}, T. Carli ³⁶, G. Carlino ^{72a}, J.I. Carlotto ¹³, B.T. Carlson ^{129,r}, E.M. Carlson ^{165,156a}, L. Carminati ^{71a,71b}, A. Carnelli ¹³⁵, M. Carnesale ^{75a,75b}, S. Caron ¹¹³, E. Carquin ^{137f}, S. Carrá ^{71a}, G. Carratta ^{23b,23a}, A.M. Carroll ¹²³, J.W.S. Carter ¹⁵⁵, T.M. Carter ⁵², M.P. Casado ^{13,i}, M. Caspar ⁴⁸, F.L. Castillo ⁴, L. Castillo Garcia ¹³, V. Castillo Gimenez ¹⁶³, N.F. Castro ^{130a,130e}, A. Catinaccio ³⁶, J.R. Catmore ¹²⁵, T. Cavaliere ⁴, V. Cavaliere ²⁹, N. Cavalli ^{23b,23a}, V. Cavasinni ^{74a,74b}, Y.C. Cekmecelioglu ⁴⁸, E. Celebi ^{21a}, F. Celli ¹²⁶, M.S. Centonze ^{70a,70b}, V. Cepaitis ⁵⁶, K. Cerny ¹²², A.S. Cerqueira ^{83a}, A. Cerri ¹⁴⁶, L. Cerrito ^{76a,76b}, F. Cerutti ^{17a}, B. Cervato ¹⁴¹, A. Cervelli ^{23b}, G. Cesarini ⁵³, S.A. Cetin ⁸², D. Chakraborty ¹¹⁵, J. Chan ^{17a}, W.Y. Chan ¹⁵³, J.D. Chapman ³², E. Chapon ¹³⁵, B. Chargeishvili ^{149b}, D.G. Charlton ²⁰, M. Chatterjee ¹⁹, C. Chauhan ¹³³, Y. Che ^{14c}, S. Chekanov ⁶, S.V. Chekulaev ^{156a}, G.A. Chelkov ^{38,a}, A. Chen ¹⁰⁶, B. Chen ¹⁵¹, B. Chen ¹⁶⁵, H. Chen ^{14c}, H. Chen ²⁹, J. Chen ^{62c}, J. Chen ¹⁴², M. Chen ¹²⁶, S. Chen ¹⁵³, S.J. Chen ^{14c}, X. Chen ^{62c,135}, X. Chen ^{14b,af}, Y. Chen ^{62a}, C.L. Cheng ¹⁷⁰, H.C. Cheng ^{64a}, S. Cheong ¹⁴³, A. Cheplakov ³⁸, E. Cheremushkina ⁴⁸, E. Cherepanova ¹¹⁴, R. Cherkaoui El Moursli ^{35e}, E. Cheu ⁷, K. Cheung ⁶⁵, L. Chevalier ¹³⁵, V. Chiarella ⁵³, G. Chiarelli ^{74a}, N. Chiedde ¹⁰², G. Chiodini ^{70a}, A.S. Chisholm ²⁰, A. Chitan ^{27b}, M. Chitishvili ¹⁶³, M.V. Chizhov ³⁸, K. Choi ¹¹, Y. Chou ¹³⁸, E.Y.S. Chow ¹¹³, K.L. Chu ¹⁶⁹, M.C. Chu ^{64a}, X. Chu ^{14a,14e}, J. Chudoba ¹³¹,

J.J. Chwastowski ^{id}87, D. Cieri ^{id}110, K.M. Ciesla ^{id}86a, V. Cindro ^{id}93, A. Ciocio ^{id}17a, F. Cirotto ^{id}72a,72b, Z.H. Citron ^{id}169,k, M. Citterio ^{id}71a, D.A. Ciubotaru ^{id}27b, A. Clark ^{id}56, P.J. Clark ^{id}52, C. Clarry ^{id}155, J.M. Clavijo Columbie ^{id}48, S.E. Clawson ^{id}48, C. Clement ^{id}47a,47b, J. Clercx ^{id}48, Y. Coadou ^{id}102, M. Cobal ^{id}69a,69c, A. Coccaro ^{id}57b, R.F. Coelho Barrue ^{id}130a, R. Coelho Lopes De Sa ^{id}103, S. Coelli ^{id}71a, B. Cole ^{id}41, J. Collot ^{id}60, P. Conde Muiño ^{id}130a,130g, M.P. Connell ^{id}33c, S.H. Connell ^{id}33c, I.A. Connelly ^{id}59, E.I. Conroy ^{id}126, F. Conventi ^{id}72a,ah, H.G. Cooke ^{id}20, A.M. Cooper-Sarkar ^{id}126, A. Cordeiro Oudot Choi ^{id}127, L.D. Corpe ^{id}40, M. Corradi ^{id}75a,75b, F. Corriveau ^{id}104,x, A. Cortes-Gonzalez ^{id}18, M.J. Costa ^{id}163, F. Costanza ^{id}4, D. Costanzo ^{id}139, B.M. Cote ^{id}119, G. Cowan ^{id}95, K. Cranmer ^{id}170, D. Cremonini ^{id}23b,23a, S. Crépe-Renaudin ^{id}60, F. Crescioli ^{id}127, M. Cristinziani ^{id}141, M. Cristoforetti ^{id}78a,78b, V. Croft ^{id}114, J.E. Crosby ^{id}121, G. Crosetti ^{id}43b,43a, A. Cueto ^{id}99, T. Cuhadar Donszelmann ^{id}159, H. Cui ^{id}14a,14e, Z. Cui ^{id}7, W.R. Cunningham ^{id}59, F. Curcio ^{id}43b,43a, P. Czodrowski ^{id}36, M.M. Czurylo ^{id}63b, M.J. Da Cunha Sargedas De Sousa ^{id}57b,57a, J.V. Da Fonseca Pinto ^{id}83b, C. Da Via ^{id}101, W. Dabrowski ^{id}86a, T. Dado ^{id}49, S. Dahbi ^{id}33g, T. Dai ^{id}106, D. Dal Santo ^{id}19, C. Dallapiccola ^{id}103, M. Dam ^{id}42, G. D'amen ^{id}29, V. D'Amico ^{id}109, J. Damp ^{id}100, J.R. Dandoy ^{id}34, M. Danninger ^{id}142, V. Dao ^{id}36, G. Darbo ^{id}57b, S. Darmora ^{id}6, S.J. Das ^{id}29,aj, S. D'Auria ^{id}71a,71b, C. David ^{id}33a, T. Davidek ^{id}133, B. Davis-Purcell ^{id}34, I. Dawson ^{id}94, H.A. Day-hall ^{id}132, K. De ^{id}8, R. De Asmundis ^{id}72a, N. De Biase ^{id}48, S. De Castro ^{id}23b,23a, N. De Groot ^{id}113, P. de Jong ^{id}114, H. De la Torre ^{id}115, A. De Maria ^{id}14c, A. De Salvo ^{id}75a, U. De Sanctis ^{id}76a,76b, F. De Santis ^{id}70a,70b, A. De Santo ^{id}146, J.B. De Vivie De Regie ^{id}60, D.V. Dedovich ^{id}38, J. Degens ^{id}114, A.M. Deiana ^{id}44, F. Del Corso ^{id}23b,23a, J. Del Peso ^{id}99, F. Del Rio ^{id}63a, L. Delagrangé ^{id}127, F. Deliot ^{id}135, C.M. Delitzsch ^{id}49, M. Della Pietra ^{id}72a,72b, D. Della Volpe ^{id}56, A. Dell'Acqua ^{id}36, L. Dell'Asta ^{id}71a,71b, M. Delmastro ^{id}4, P.A. Delsart ^{id}60, S. Demers ^{id}172, M. Demichev ^{id}38, S.P. Denisov ^{id}37, L. D'Eramo ^{id}40, D. Derendarz ^{id}87, F. Derue ^{id}127, P. Dervan ^{id}92, K. Desch ^{id}24, C. Deutsch ^{id}24, F.A. Di Bello ^{id}57b,57a, A. Di Ciaccio ^{id}76a,76b, L. Di Ciaccio ^{id}4, A. Di Domenico ^{id}75a,75b, C. Di Donato ^{id}72a,72b, A. Di Girolamo ^{id}36, G. Di Gregorio ^{id}36, A. Di Luca ^{id}78a,78b, B. Di Micco ^{id}77a,77b, R. Di Nardo ^{id}77a,77b, M. Diamantopoulou ^{id}34, F.A. Dias ^{id}114, T. Dias Do Vale ^{id}142, M.A. Diaz ^{id}137a,137b, F.G. Diaz Capriles ^{id}24, M. Didenko ^{id}163, E.B. Diehl ^{id}106, L. Diehl ^{id}54, S. Díez Cornell ^{id}48, C. Diez Pardos ^{id}141, C. Dimitriadi ^{id}161,24, A. Dimitrievska ^{id}17a, J. Dingfelder ^{id}24, I-M. Dinu ^{id}27b, S.J. Dittmeier ^{id}63b, F. Dittus ^{id}36, F. Djama ^{id}102, T. Djobava ^{id}149b, C. Doglioni ^{id}101,98, A. Dohnalova ^{id}28a, J. Dolejsi ^{id}133, Z. Dolezal ^{id}133, K.M. Dona ^{id}39, M. Donadelli ^{id}83c, B. Dong ^{id}107, J. Donini ^{id}40, A. D'Onofrio ^{id}72a,72b, M. D'Onofrio ^{id}92, J. Dopke ^{id}134, A. Doria ^{id}72a, N. Dos Santos Fernandes ^{id}130a, P. Dougan ^{id}101, M.T. Dova ^{id}90, A.T. Doyle ^{id}59, M.A. Draguet ^{id}126, E. Dreyer ^{id}169, I. Drivas-koulouris ^{id}10, M. Drnevich ^{id}117, M. Drozdova ^{id}56, D. Du ^{id}62a, T.A. du Pree ^{id}114, F. Dubinin ^{id}37, M. Dubovsky ^{id}28a, E. Duchovni ^{id}169, G. Duckeck ^{id}109, O.A. Ducu ^{id}27b, D. Duda ^{id}52, A. Dudarev ^{id}36, E.R. Duden ^{id}26, M. D'uffizi ^{id}101, L. Duflost ^{id}66, M. Dührssen ^{id}36, A.E. Dumitriu ^{id}27b, M. Dunford ^{id}63a, S. Dungs ^{id}49, K. Dunne ^{id}47a,47b, A. Duperrin ^{id}102, H. Duran Yildiz ^{id}3a, M. Düren ^{id}58, A. Durglishvili ^{id}149b, B.L. Dwyer ^{id}115, G.I. Dyckes ^{id}17a, M. Dyndal ^{id}86a, B.S. Dziedzic ^{id}87, Z.O. Earnshaw ^{id}146, G.H. Eberwein ^{id}126, B. Eckerova ^{id}28a, S. Eggebrecht ^{id}55, E. Egidio Purcino De Souza ^{id}127, L.F. Ehrke ^{id}56, G. Eigen ^{id}16, K. Einsweiler ^{id}17a, T. Ekelof ^{id}161, P.A. Ekman ^{id}98, S. El Farkh ^{id}35b, Y. El Ghazali ^{id}35b, H. El Jarrari ^{id}36, A. El Moussaouy ^{id}108, V. Ellajosyula ^{id}161, M. Ellert ^{id}161, F. Ellinghaus ^{id}171, N. Ellis ^{id}36, J. Elmsheuser ^{id}29, M. Elsing ^{id}36, D. Emelianov ^{id}134, Y. Enari ^{id}153, I. Ene ^{id}17a, S. Epari ^{id}13, P.A. Erland ^{id}87, M. Errenst ^{id}171, M. Escalier ^{id}66, C. Escobar ^{id}163, E. Etzion ^{id}151, G. Evans ^{id}130a, H. Evans ^{id}68, L.S. Evans ^{id}95, M.O. Evans ^{id}146, A. Ezhilov ^{id}37, S. Ezzarqtouni ^{id}35a, F. Fabbri ^{id}59, L. Fabbri ^{id}23b,23a, G. Facini ^{id}96, V. Fadeyev ^{id}136, R.M. Fakhrutdinov ^{id}37, D. Fakoudis ^{id}100, S. Falciano ^{id}75a, L.F. Falda Ulhoa Coelho ^{id}36, P.J. Falke ^{id}24, J. Faltova ^{id}133,

C. Fan ¹⁶², Y. Fan ^{14a}, Y. Fang ^{14a,14e}, M. Fanti ^{71a,71b}, M. Faraj ^{69a,69b}, Z. Farazpay ⁹⁷, A. Farbin ⁸, A. Farilla ^{77a}, T. Farooque ¹⁰⁷, S.M. Farrington ⁵², F. Fassi ^{35e}, D. Fassouliotis ⁹, M. Faucci Giannelli ^{76a,76b}, W.J. Fawcett ³², L. Fayard ⁶⁶, P. Federic ¹³³, P. Federicova ¹³¹, O.L. Fedin ^{37,a}, G. Fedotov ³⁷, M. Feickert ¹⁷⁰, L. Feligioni ¹⁰², D.E. Fellers ¹²³, C. Feng ^{62b}, M. Feng ^{14b}, Z. Feng ¹¹⁴, M.J. Fenton ¹⁵⁹, A.B. Fenyuk ³⁷, L. Ferencz ⁴⁸, R.A.M. Ferguson ⁹¹, S.I. Fernandez Luengo ^{137f}, P. Fernandez Martinez ¹³, M.J.V. Fernoux ¹⁰², J. Ferrando ⁹¹, A. Ferrari ¹⁶¹, P. Ferrari ^{114,113}, R. Ferrari ^{73a}, D. Ferrere ⁵⁶, C. Ferretti ¹⁰⁶, F. Fiedler ¹⁰⁰, P. Fiedler ¹³², A. Filipčič ⁹³, E.K. Filmer ¹, F. Filthaut ¹¹³, M.C.N. Fiolhais ^{130a,130c}, L. Fiorini ¹⁶³, W.C. Fisher ¹⁰⁷, T. Fitschen ¹⁰¹, P.M. Fitzhugh ¹³⁵, I. Fleck ¹⁴¹, P. Fleischmann ¹⁰⁶, T. Flick ¹⁷¹, M. Flores ^{33d,ad}, L.R. Flores Castillo ^{64a}, L. Flores Sanz De Acedo ³⁶, F.M. Follega ^{78a,78b}, N. Fomin ¹⁶, J.H. Foo ¹⁵⁵, A. Formica ¹³⁵, A.C. Forti ¹⁰¹, E. Fortin ³⁶, A.W. Fortman ^{17a}, M.G. Foti ^{17a}, L. Fountas ^{9,j}, D. Fournier ⁶⁶, H. Fox ⁹¹, P. Francavilla ^{74a,74b}, S. Francescato ⁶¹, S. Franchellucci ⁵⁶, M. Franchini ^{23b,23a}, S. Franchino ^{63a}, D. Francis ³⁶, L. Franco ¹¹³, V. Franco Lima ³⁶, L. Franconi ⁴⁸, M. Franklin ⁶¹, G. Frattari ²⁶, A.C. Freegard ⁹⁴, W.S. Freund ^{83b}, Y.Y. Frid ¹⁵¹, J. Friend ⁵⁹, N. Fritzsche ⁵⁰, A. Froch ⁵⁴, D. Froidevaux ³⁶, J.A. Frost ¹²⁶, Y. Fu ^{62a}, S. Fuenzalida Garrido ^{137f}, M. Fujimoto ¹⁰², K.Y. Fung ^{64a}, E. Furtado De Simas Filho ^{83b}, M. Furukawa ¹⁵³, J. Fuster ¹⁶³, A. Gabrielli ^{23b,23a}, A. Gabrielli ¹⁵⁵, P. Gadow ³⁶, G. Gagliardi ^{57b,57a}, L.G. Gagnon ^{17a}, E.J. Gallas ¹²⁶, B.J. Gallop ¹³⁴, K.K. Gan ¹¹⁹, S. Ganguly ¹⁵³, Y. Gao ⁵², F.M. Garay Walls ^{137a,137b}, B. Garcia ²⁹, C. García ¹⁶³, A. Garcia Alonso ¹¹⁴, A.G. Garcia Caffaro ¹⁷², J.E. García Navarro ¹⁶³, M. Garcia-Sciveres ^{17a}, G.L. Gardner ¹²⁸, R.W. Gardner ³⁹, N. Garelli ¹⁵⁸, D. Garg ⁸⁰, R.B. Garg ^{143,n}, J.M. Gargan ⁵², C.A. Garner ¹⁵⁵, C.M. Garvey ^{33a}, P. Gaspar ^{83b}, V.K. Gassmann ¹⁵⁸, G. Gaudio ^{73a}, V. Gautam ¹³, P. Gauzzi ^{75a,75b}, I.L. Gavrilenko ³⁷, A. Gavrilyuk ³⁷, C. Gay ¹⁶⁴, G. Gaycken ⁴⁸, E.N. Gazis ¹⁰, A.A. Geanta ^{27b}, C.M. Gee ¹³⁶, A. Gekow ¹¹⁹, C. Gemme ^{57b}, M.H. Genest ⁶⁰, S. Gentile ^{75a,75b}, A.D. Gentry ¹¹², S. George ⁹⁵, W.F. George ²⁰, T. Geralis ⁴⁶, P. Gessinger-Befurt ³⁶, M.E. Geyik ¹⁷¹, M. Ghani ¹⁶⁷, M. Ghneimat ¹⁴¹, K. Ghorbanian ⁹⁴, A. Ghosal ¹⁴¹, A. Ghosh ¹⁵⁹, A. Ghosh ⁷, B. Giacobbe ^{23b}, S. Giagu ^{75a,75b}, T. Giani ¹¹⁴, P. Giannetti ^{74a}, A. Giannini ^{62a}, S.M. Gibson ⁹⁵, M. Gignac ¹³⁶, D.T. Gil ^{86b}, A.K. Gilbert ^{86a}, B.J. Gilbert ⁴¹, D. Gillberg ³⁴, G. Gilles ¹¹⁴, L. Ginabat ¹²⁷, D.M. Gingrich ^{2,ag}, M.P. Giordani ^{69a,69c}, P.F. Giraud ¹³⁵, G. Giugliarelli ^{69a,69c}, D. Giugni ^{71a}, F. Giuli ³⁶, I. Gkialas ^{9,j}, L.K. Gladilin ³⁷, C. Glasman ⁹⁹, G.R. Gledhill ¹²³, G. Glemža ⁴⁸, M. Glisic ¹²³, I. Gnesi ^{43b,f}, Y. Go ²⁹, M. Goblirsch-Kolb ³⁶, B. Gocke ⁴⁹, D. Godin ¹⁰⁸, B. Gokturk ^{21a}, S. Goldfarb ¹⁰⁵, T. Golling ⁵⁶, M.G.D. Gololo ^{33g}, D. Golubkov ³⁷, J.P. Gombas ¹⁰⁷, A. Gomes ^{130a,130b}, G. Gomes Da Silva ¹⁴¹, A.J. Gomez Delegido ¹⁶³, R. Gonçalves ^{130a,130c}, L. Gonella ²⁰, A. Gongadze ^{149c}, F. Gonnella ²⁰, J.L. Gonski ⁴¹, R.Y. González Andana ⁵², S. González de la Hoz ¹⁶³, R. Gonzalez Lopez ⁹², C. Gonzalez Renteria ^{17a}, M.V. Gonzalez Rodrigues ⁴⁸, R. Gonzalez Suarez ¹⁶¹, S. Gonzalez-Sevilla ⁵⁶, G.R. Gonzalvo Rodriguez ¹⁶³, L. Goossens ³⁶, B. Gorini ³⁶, E. Gorini ^{70a,70b}, A. Gorišek ⁹³, T.C. Gosart ¹²⁸, A.T. Goshaw ⁵¹, M.I. Gostkin ³⁸, S. Goswami ¹²¹, C.A. Gottardo ³⁶, S.A. Gotz ¹⁰⁹, M. Gouighri ^{35b}, V. Goumarre ⁴⁸, A.G. Goussiou ¹³⁸, N. Govender ^{33c}, I. Grabowska-Bold ^{86a}, K. Graham ³⁴, E. Gramstad ¹²⁵, S. Grancagnolo ^{70a,70b}, M. Grandi ¹⁴⁶, C.M. Grant ^{1,135}, P.M. Gravila ^{27f}, F.G. Gravili ^{70a,70b}, H.M. Gray ^{17a}, M. Greco ^{70a,70b}, C. Grefe ²⁴, I.M. Gregor ⁴⁸, P. Grenier ¹⁴³, S.G. Grewe ¹¹⁰, C. Grieco ¹³, A.A. Grillo ¹³⁶, K. Grimm ³¹, S. Grinstein ^{13,t}, J.-F. Grivaz ⁶⁶, E. Gross ¹⁶⁹, J. Grosse-Knetter ⁵⁵, J.C. Grundy ¹²⁶, L. Guan ¹⁰⁶, W. Guan ²⁹, C. Gubbels ¹⁶⁴, J.G.R. Guerrero Rojas ¹⁶³, G. Guerrieri ^{69a,69c}, F. Guescini ¹¹⁰, R. Gugel ¹⁰⁰, J.A.M. Guhit ¹⁰⁶, A. Guida ¹⁸, E. Guilloton ^{167,134}, S. Guindon ³⁶, F. Guo ^{14a,14e}, J. Guo ^{62c}, L. Guo ⁴⁸, Y. Guo ¹⁰⁶,

R. Gupta ⁴⁸, R. Gupta ¹²⁹, S. Gurbuz ²⁴, S.S. Gurdasani ⁵⁴, G. Gustavino ³⁶, M. Guth ⁵⁶, P. Gutierrez ¹²⁰, L.F. Gutierrez Zagazeta ¹²⁸, M. Gutsche ⁵⁰, C. Gutschow ⁹⁶, C. Gwenlan ¹²⁶, C.B. Gwilliam ⁹², E.S. Haaland ¹²⁵, A. Haas ¹¹⁷, M. Habedank ⁴⁸, C. Haber ^{17a}, H.K. Hadavand ⁸, A. Hadeef ⁵⁰, S. Hadzic ¹¹⁰, A.I. Hagan ⁹¹, J.J. Hahn ¹⁴¹, E.H. Haines ⁹⁶, M. Haleem ¹⁶⁶, J. Haley ¹²¹, J.J. Hall ¹³⁹, G.D. Hallewell ¹⁰², L. Halser ¹⁹, K. Hamano ¹⁶⁵, M. Hamer ²⁴, G.N. Hamity ⁵², E.J. Hampshire ⁹⁵, J. Han ^{62b}, K. Han ^{62a}, L. Han ^{14c}, L. Han ^{62a}, S. Han ^{17a}, Y.F. Han ¹⁵⁵, K. Hanagaki ⁸⁴, M. Hance ¹³⁶, D.A. Hangal ⁴¹, H. Hanif ¹⁴², M.D. Hank ¹²⁸, J.B. Hansen ⁴², P.H. Hansen ⁴², K. Hara ¹⁵⁷, D. Harada ⁵⁶, T. Harenberg ¹⁷¹, S. Harkusha ³⁷, M.L. Harris ¹⁰³, Y.T. Harris ¹²⁶, J. Harrison ¹³, N.M. Harrison ¹¹⁹, P.F. Harrison ¹⁶⁷, N.M. Hartman ¹¹⁰, N.M. Hartmann ¹⁰⁹, Y. Hasegawa ¹⁴⁰, R. Hauser ¹⁰⁷, C.M. Hawkes ²⁰, R.J. Hawkins ³⁶, Y. Hayashi ¹⁵³, S. Hayashida ¹¹¹, D. Hayden ¹⁰⁷, C. Hayes ¹⁰⁶, R.L. Hayes ¹¹⁴, C.P. Hays ¹²⁶, J.M. Hays ⁹⁴, H.S. Hayward ⁹², F. He ^{62a}, M. He ^{14a,14e}, Y. He ¹⁵⁴, Y. He ⁴⁸, N.B. Heatley ⁹⁴, V. Hedberg ⁹⁸, A.L. Heggelund ¹²⁵, N.D. Hehir ^{94,*}, C. Heidegger ⁵⁴, K.K. Heidegger ⁵⁴, W.D. Heidorn ⁸¹, J. Heilman ³⁴, S. Heim ⁴⁸, T. Heim ^{17a}, J.G. Heinlein ¹²⁸, J.J. Heinrich ¹²³, L. Heinrich ^{110,ae}, J. Hejbal ¹³¹, A. Held ¹⁷⁰, S. Hellesund ¹⁶, C.M. Helling ¹⁶⁴, S. Hellman ^{47a,47b}, R.C.W. Henderson ⁹¹, L. Henkelmann ³², A.M. Henriques Correia ³⁶, H. Herde ⁹⁸, Y. Hernández Jiménez ¹⁴⁵, L.M. Herrmann ²⁴, T. Herrmann ⁵⁰, G. Herten ⁵⁴, R. Hertenberger ¹⁰⁹, L. Hervas ³⁶, M.E. Hesping ¹⁰⁰, N.P. Hessey ^{156a}, E. Hill ¹⁵⁵, S.J. Hillier ²⁰, J.R. Hinds ¹⁰⁷, F. Hinterkeuser ²⁴, M. Hirose ¹²⁴, S. Hirose ¹⁵⁷, D. Hirschbuehl ¹⁷¹, T.G. Hitchings ¹⁰¹, B. Hiti ⁹³, J. Hobbs ¹⁴⁵, R. Hobincu ^{27e}, N. Hod ¹⁶⁹, M.C. Hodgkinson ¹³⁹, B.H. Hodgkinson ³², A. Hoecker ³⁶, D.D. Hofer ¹⁰⁶, J. Hofer ⁴⁸, T. Holm ²⁴, M. Holzbock ¹¹⁰, L.B.A.H. Hommels ³², B.P. Honan ¹⁰¹, J. Hong ^{62c}, T.M. Hong ¹²⁹, B.H. Hooberman ¹⁶², W.H. Hopkins ⁶, Y. Horii ¹¹¹, S. Hou ¹⁴⁸, A.S. Howard ⁹³, J. Howarth ⁵⁹, J. Hoya ⁶, M. Hrabovsky ¹²², A. Hrynevich ⁴⁸, T. Hryn'ova ⁴, P.J. Hsu ⁶⁵, S.-C. Hsu ¹³⁸, Q. Hu ^{62a}, Y.F. Hu ^{14a,14e}, S. Huang ^{64b}, X. Huang ^{14c}, X. Huang ^{14a,14e}, Y. Huang ¹³⁹, Y. Huang ^{14a}, Z. Huang ¹⁰¹, Z. Hubacek ¹³², M. Huebner ²⁴, F. Huegging ²⁴, T.B. Huffman ¹²⁶, C.A. Hugli ⁴⁸, M. Huhtinen ³⁶, S.K. Huiberts ¹⁶, R. Hulsken ¹⁰⁴, N. Huseynov ¹², J. Huston ¹⁰⁷, J. Huth ⁶¹, R. Hyneman ¹⁴³, G. Iacobucci ⁵⁶, G. Iakovidis ²⁹, I. Ibragimov ¹⁴¹, L. Iconomidou-Fayard ⁶⁶, J.P. Iddon ³⁶, P. Iengo ^{72a,72b}, R. Iguchi ¹⁵³, T. Iizawa ¹²⁶, Y. Ikegami ⁸⁴, N. Ilic ¹⁵⁵, H. Imam ^{35a}, M. Ince Lezki ⁵⁶, T. Ingebretsen Carlson ^{47a,47b}, G. Introzzi ^{73a,73b}, M. Iodice ^{77a}, V. Ippolito ^{75a,75b}, R.K. Irwin ⁹², M. Ishino ¹⁵³, W. Islam ¹⁷⁰, C. Issever ^{18,48}, S. Istin ^{21a,al}, H. Ito ¹⁶⁸, J.M. Iturbe Ponce ^{64a}, R. Iuppa ^{78a,78b}, A. Ivina ¹⁶⁹, J.M. Izen ⁴⁵, V. Izzo ^{72a}, P. Jacka ^{131,132}, P. Jackson ¹, B.P. Jaeger ¹⁴², C.S. Jagfeld ¹⁰⁹, G. Jain ^{156a}, P. Jain ⁵⁴, K. Jakobs ⁵⁴, T. Jakoubek ¹⁶⁹, J. Jamieson ⁵⁹, K.W. Janas ^{86a}, M. Javurkova ¹⁰³, L. Jeanty ¹²³, J. Jejelava ^{149a,aa}, P. Jenni ^{54,g}, C.E. Jessiman ³⁴, C. Jia ^{62b}, J. Jia ¹⁴⁵, X. Jia ⁶¹, X. Jia ^{14a,14e}, Z. Jia ^{14c}, S. Jiggins ⁴⁸, J. Jimenez Pena ¹³, S. Jin ^{14c}, A. Jinaru ^{27b}, O. Jinnouchi ¹⁵⁴, P. Johansson ¹³⁹, K.A. Johns ⁷, J.W. Johnson ¹³⁶, D.M. Jones ³², E. Jones ⁴⁸, P. Jones ³², R.W.L. Jones ⁹¹, T.J. Jones ⁹², H.L. Joos ^{55,36}, R. Joshi ¹¹⁹, J. Jovicevic ¹⁵, X. Ju ^{17a}, J.J. Junggeburth ¹⁰³, T. Junkermann ^{63a}, A. Juste Rozas ^{13,t}, M.K. Juzek ⁸⁷, S. Kabana ^{137e}, A. Kaczmarska ⁸⁷, M. Kado ¹¹⁰, H. Kagan ¹¹⁹, M. Kagan ¹⁴³, A. Kahn ⁴¹, A. Kahn ¹²⁸, C. Kahra ¹⁰⁰, T. Kaji ¹⁵³, E. Kajomovitz ¹⁵⁰, N. Kakati ¹⁶⁹, I. Kalaitzidou ⁵⁴, C.W. Kalderon ²⁹, A. Kamenshchikov ¹⁵⁵, N.J. Kang ¹³⁶, D. Kar ^{33g}, K. Karava ¹²⁶, M.J. Kareem ^{156b}, E. Karentzos ⁵⁴, I. Karkanas ¹⁵², O. Karkout ¹¹⁴, S.N. Karpov ³⁸, Z.M. Karpova ³⁸, V. Kartvelishvili ⁹¹, A.N. Karyukhin ³⁷, E. Kasimi ¹⁵², J. Katzy ⁴⁸, S. Kaur ³⁴, K. Kawade ¹⁴⁰, M.P. Kawale ¹²⁰, C. Kawamoto ⁸⁸, T. Kawamoto ^{62a}, E.F. Kay ³⁶, F.I. Kaya ¹⁵⁸, S. Kazakos ¹⁰⁷, V.F. Kazanin ³⁷, Y. Ke ¹⁴⁵, J.M. Keaveney ^{33a}, R. Keeler ¹⁶⁵, G.V. Kehris ⁶¹, J.S. Keller ³⁴,

A.S. Kelly⁹⁶, J.J. Kempster¹⁴⁶, P.D. Kennedy¹⁰⁰, O. Kepka¹³¹, B.P. Kerridge¹⁶⁷, S. Kersten¹⁷¹,
 B.P. Kerševan⁹³, S. Keshri⁶⁶, L. Keszeghova^{28a}, S. Ketabchi Haghighat¹⁵⁵, R.A. Khan¹²⁹,
 A. Khanov¹²¹, A.G. Kharlamov³⁷, T. Kharlamova³⁷, E.E. Khoda¹³⁸, M. Kholodenko³⁷,
 T.J. Khoo¹⁸, G. Khoriali¹⁶⁶, J. Khubua^{149b,*}, Y.A.R. Khwaira⁶⁶, B. Kibirige^{33g},
 A. Kilgallon¹²³, D.W. Kim^{47a,47b}, Y.K. Kim³⁹, N. Kimura⁹⁶, M.K. Kingston⁵⁵,
 A. Kirchhoff⁵⁵, C. Kirfel²⁴, F. Kirfel²⁴, J. Kirk¹³⁴, A.E. Kiryunin¹¹⁰, C. Kitsaki¹⁰,
 O. Kivernyk²⁴, M. Klassen^{63a}, C. Klein³⁴, L. Klein¹⁶⁶, M.H. Klein⁴⁴, S.B. Klein⁵⁶,
 U. Klein⁹², P. Klimek³⁶, A. Klimentov²⁹, T. Klioutchnikova³⁶, P. Kluit¹¹⁴, S. Kluth¹¹⁰,
 E. Kneringer⁷⁹, T.M. Knight¹⁵⁵, A. Knue⁴⁹, R. Kobayashi⁸⁸, D. Kobylanski¹⁶⁹,
 S.F. Koch¹²⁶, M. Kocian¹⁴³, P. Kodyš¹³³, D.M. Koeck¹²³, P.T. Koenig²⁴, T. Koffas³⁴,
 O. Kolay⁵⁰, I. Koletsou⁴, T. Komarek¹²², K. Köneke⁵⁴, A.X.Y. Kong¹, T. Kono¹¹⁸,
 N. Konstantinidis⁹⁶, P. Kontaxakis⁵⁶, B. Konya⁹⁸, R. Kopeliansky⁶⁸, S. Koperny^{86a},
 K. Korcyl⁸⁷, K. Kordas^{152,e}, A. Korn⁹⁶, S. Korn⁵⁵, I. Korolkov¹³, N. Korotkova³⁷,
 B. Kortman¹¹⁴, O. Kortner¹¹⁰, S. Kortner¹¹⁰, W.H. Kostecka¹¹⁵, V.V. Kostyukhin¹⁴¹,
 A. Kotsokechagia¹³⁵, A. Kotwal⁵¹, A. Koulouris³⁶, A. Kourkoumeli-Charalampidi^{73a,73b},
 C. Kourkoumelis⁹, E. Kourlitis^{110,ae}, O. Kovanda¹⁴⁶, R. Kowalewski¹⁶⁵, W. Kozanecki¹³⁵,
 A.S. Kozhin³⁷, V.A. Kramarenko³⁷, G. Kramberger⁹³, P. Kramer¹⁰⁰, M.W. Krasny¹²⁷,
 A. Krasnahorkay³⁶, J.W. Kraus¹⁷¹, J.A. Kremer⁴⁸, T. Kresse⁵⁰, J. Kretzschmar⁹²,
 K. Kreul¹⁸, P. Krieger¹⁵⁵, S. Krishnamurthy¹⁰³, M. Krivos¹³³, K. Krizka²⁰,
 K. Kroeninger⁴⁹, H. Kroha¹¹⁰, J. Kroll¹³¹, J. Kroll¹²⁸, K.S. Krowpman¹⁰⁷, U. Kruchonak³⁸,
 H. Krüger²⁴, N. Krumnack⁸¹, M.C. Kruse⁵¹, O. Kuchinskaia³⁷, S. Kuday^{3a}, S. Kuehn³⁶,
 R. Kuesters⁵⁴, T. Kuhl⁴⁸, V. Kukhtin³⁸, Y. Kulchitsky^{37,a}, S. Kuleshov^{137d,137b},
 M. Kumar^{33g}, N. Kumari⁴⁸, P. Kumari^{156b}, A. Kupco¹³¹, T. Kupfer⁴⁹, A. Kupich³⁷,
 O. Kuprash⁵⁴, H. Kurashige⁸⁵, L.L. Kurchaninov^{156a}, O. Kurdysh⁶⁶, Y.A. Kurochkin³⁷,
 A. Kurova³⁷, M. Kuze¹⁵⁴, A.K. Kvam¹⁰³, J. Kvita¹²², T. Kwan¹⁰⁴, N.G. Kyriacou¹⁰⁶,
 L.A.O. Laatu¹⁰², C. Lacasta¹⁶³, F. Lacava^{75a,75b}, H. Lacker¹⁸, D. Lacour¹²⁷, N.N. Lad⁹⁶,
 E. Ladygin³⁸, B. Laforge¹²⁷, T. Lagouri^{27b}, F.Z. Lahbabi^{35a}, S. Lai⁵⁵, I.K. Lakomic^{86a},
 N. Lalloue⁶⁰, J.E. Lambert¹⁶⁵, S. Lammers⁶⁸, W. Lampl⁷, C. Lampoudis^{152,e},
 A.N. Lancaster¹¹⁵, E. Lançon²⁹, U. Landgraf⁵⁴, M.P.J. Landon⁹⁴, V.S. Lang⁵⁴,
 R.J. Langenberg¹⁰³, O.K.B. Langrekken¹²⁵, A.J. Lankford¹⁵⁹, F. Lanni³⁶, K. Lantzsch²⁴,
 A. Lanza^{73a}, A. Lapertosa^{57b,57a}, J.F. Laporte¹³⁵, T. Lari^{71a}, F. Lasagni Manghi^{23b},
 M. Lassnig³⁶, V. Latonova¹³¹, A. Laudrain¹⁰⁰, A. Laurier¹⁵⁰, S.D. Lawlor¹³⁹,
 Z. Lawrence¹⁰¹, R. Lazaridou¹⁶⁷, M. Lazzaroni^{71a,71b}, B. Le¹⁰¹, E.M. Le Boulicaut⁵¹,
 B. Leban⁹³, A. Lebedev⁸¹, M. LeBlanc¹⁰¹, F. Ledroit-Guillon⁶⁰, A.C.A. Lee⁹⁶, S.C. Lee¹⁴⁸,
 S. Lee^{47a,47b}, T.F. Lee⁹², L.L. Leeuw^{33c}, H.P. Lefebvre⁹⁵, M. Lefebvre¹⁶⁵, C. Leggett^{17a},
 G. Lehmann Miotto³⁶, M. Leigh⁵⁶, W.A. Leight¹⁰³, W. Leinonen¹¹³, A. Leisos^{152,s},
 M.A.L. Leite^{83c}, C.E. Leitgeb¹⁸, R. Leitner¹³³, K.J.C. Leney⁴⁴, T. Lenz²⁴, S. Leone^{74a},
 C. Leonidopoulos⁵², A. Leopold¹⁴⁴, C. Leroy¹⁰⁸, R. Les¹⁰⁷, C.G. Lester³², M. Levchenko³⁷,
 J. Levêque⁴, L.J. Levinson¹⁶⁹, G. Levrini^{23b,23a}, M.P. Lewicki⁸⁷, D.J. Lewis⁴, A. Li⁵,
 B. Li^{62b}, C. Li^{62a}, C-Q. Li¹¹⁰, H. Li^{62a}, H. Li^{62b}, H. Li^{14c}, H. Li^{14b}, H. Li^{62b}, J. Li^{62c},
 K. Li¹³⁸, L. Li^{62c}, M. Li^{14a,14e}, Q.Y. Li^{62a}, S. Li^{14a,14e}, S. Li^{62d,62c,d}, T. Li⁵, X. Li¹⁰⁴,
 Z. Li¹²⁶, Z. Li¹⁰⁴, Z. Li^{14a,14e}, S. Liang^{14a,14e}, Z. Liang^{14a}, M. Liberatore¹³⁵, B. Liberti^{76a},
 K. Lie^{64c}, J. Lieber Marin^{83b}, H. Lien⁶⁸, K. Lin¹⁰⁷, R.E. Lindley⁷, J.H. Lindon²,
 E. Lipeles¹²⁸, A. Lipniacka¹⁶, A. Lister¹⁶⁴, J.D. Little⁴, B. Liu^{14a}, B.X. Liu¹⁴²,
 D. Liu^{62d,62c}, J.B. Liu^{62a}, J.K.K. Liu³², K. Liu^{62d,62c}, M. Liu^{62a}, M.Y. Liu^{62a}, P. Liu^{14a},
 Q. Liu^{62d,138,62c}, X. Liu^{62a}, X. Liu^{62b}, Y. Liu^{14d,14e}, Y.L. Liu^{62b}, Y.W. Liu^{62a},
 J. Llorente Merino¹⁴², S.L. Lloyd⁹⁴, E.M. Lobodzinska⁴⁸, P. Loch⁷, T. Lohse¹⁸,

K. Lohwasser ¹³⁹, E. Loiacono ⁴⁸, M. Lokajicek ^{131,*}, J.D. Lomas ²⁰, J.D. Long ¹⁶²,
 I. Longarini ¹⁵⁹, L. Longo ^{70a,70b}, R. Longo ¹⁶², I. Lopez Paz ⁶⁷, A. Lopez Solis ⁴⁸,
 N. Lorenzo Martinez ⁴, A.M. Lory ¹⁰⁹, G. Löschcke Centeno ¹⁴⁶, O. Loseva ³⁷, X. Lou ^{47a,47b},
 X. Lou ^{14a,14e}, A. Lounis ⁶⁶, J. Love ⁶, P.A. Love ⁹¹, G. Lu ^{14a,14e}, M. Lu ⁸⁰, S. Lu ¹²⁸,
 Y.J. Lu ⁶⁵, H.J. Lubatti ¹³⁸, C. Luci ^{75a,75b}, F.L. Lucio Alves ^{14c}, F. Luehring ⁶⁸, I. Luise ¹⁴⁵,
 O. Lukianchuk ⁶⁶, O. Lundberg ¹⁴⁴, B. Lund-Jensen ^{144,*}, N.A. Luongo ⁶, M.S. Lutz ³⁶,
 A.B. Lux ²⁵, D. Lynn ²⁹, R. Lysak ¹³¹, E. Lytken ⁹⁸, V. Lyubushkin ³⁸, T. Lyubushkina ³⁸,
 M.M. Lyukova ¹⁴⁵, H. Ma ²⁹, K. Ma ^{62a}, L.L. Ma ^{62b}, W. Ma ^{62a}, Y. Ma ¹²¹,
 D.M. Mac Donell ¹⁶⁵, G. Maccarrone ⁵³, J.C. MacDonald ¹⁰⁰, P.C. Machado De Abreu Farias ^{83b},
 R. Madar ⁴⁰, W.F. Mader ⁵⁰, T. Madula ⁹⁶, J. Maeda ⁸⁵, T. Maeno ²⁹, H. Maguire ¹³⁹,
 V. Maiboroda ¹³⁵, A. Maio ^{130a,130b,130d}, K. Maj ^{86a}, O. Majersky ⁴⁸, S. Majewski ¹²³,
 N. Makovec ⁶⁶, V. Maksimovic ¹⁵, B. Malaescu ¹²⁷, Pa. Malecki ⁸⁷, V.P. Maleev ³⁷,
 F. Malek ^{60,o}, M. Mali ⁹³, D. Malito ⁹⁵, U. Mallik ⁸⁰, S. Maltezos ¹⁰, S. Malyukov ³⁸,
 J. Mamuzic ¹³, G. Mancini ⁵³, M.N. Mancini ²⁶, G. Manco ^{73a,73b}, J.P. Mandalia ⁹⁴,
 I. Mandić ⁹³, L. Manhaes de Andrade Filho ^{83a}, I.M. Maniatis ¹⁶⁹, J. Manjarres Ramos ^{102,ab},
 D.C. Mankad ¹⁶⁹, A. Mann ¹⁰⁹, S. Manzoni ³⁶, L. Mao ^{62c}, X. Mapekula ^{33c}, A. Marantis ^{152,s},
 G. Marchiori ⁵, M. Marcisovsky ¹³¹, C. Marcon ^{71a}, M. Marinescu ²⁰, S. Marium ⁴⁸,
 M. Marjanovic ¹²⁰, E.J. Marshall ⁹¹, Z. Marshall ^{17a}, S. Marti-Garcia ¹⁶³, T.A. Martin ¹⁶⁷,
 V.J. Martin ⁵², B. Martin dit Latour ¹⁶, L. Martinelli ^{75a,75b}, M. Martinez ^{13,t},
 P. Martinez Agullo ¹⁶³, V.I. Martinez Outschoorn ¹⁰³, P. Martinez Suarez ¹³, S. Martin-Haugh ¹³⁴,
 V.S. Martoiu ^{27b}, A.C. Martyniuk ⁹⁶, A. Marzin ³⁶, D. Mascione ^{78a,78b}, L. Masetti ¹⁰⁰,
 T. Mashimo ¹⁵³, J. Masik ¹⁰¹, A.L. Maslennikov ³⁷, P. Massarotti ^{72a,72b}, P. Mastrandrea ^{74a,74b},
 A. Mastroberardino ^{43b,43a}, T. Masubuchi ¹⁵³, T. Mathisen ¹⁶¹, J. Matousek ¹³³, N. Matsuzawa ¹⁵³,
 J. Maurer ^{27b}, B. Maček ⁹³, D.A. Maximov ³⁷, R. Mazini ¹⁴⁸, I. Maznas ¹⁵², M. Mazza ¹⁰⁷,
 S.M. Mazza ¹³⁶, E. Mazzeo ^{71a,71b}, C. Mc Ginn ²⁹, J.P. Mc Gowan ¹⁰⁴, S.P. Mc Kee ¹⁰⁶,
 C.C. McCracken ¹⁶⁴, E.F. McDonald ¹⁰⁵, A.E. McDougall ¹¹⁴, J.A. Mcfayden ¹⁴⁶,
 R.P. McGovern ¹²⁸, G. Mchedlidze ^{149b}, R.P. Mckenzie ^{33g}, T.C. McLachlan ⁴⁸,
 D.J. McLaughlin ⁹⁶, S.J. McMahon ¹³⁴, C.M. Mcpartland ⁹², R.A. McPherson ^{165,x},
 S. Mehlhase ¹⁰⁹, A. Mehta ⁹², D. Melini ¹⁶³, B.R. Mellado Garcia ^{33g}, A.H. Melo ⁵⁵,
 F. Meloni ⁴⁸, A.M. Mendes Jacques Da Costa ¹⁰¹, H.Y. Meng ¹⁵⁵, L. Meng ⁹¹, S. Menke ¹¹⁰,
 M. Mentink ³⁶, E. Meoni ^{43b,43a}, G. Mercado ¹¹⁵, C. Merlassino ^{69a,69c}, L. Merola ^{72a,72b},
 C. Meroni ^{71a,71b}, J. Metcalfe ⁶, A.S. Mete ⁶, C. Meyer ⁶⁸, J-P. Meyer ¹³⁵, R.P. Middleton ¹³⁴,
 L. Mijović ⁵², G. Mikenberg ¹⁶⁹, M. Mikestikova ¹³¹, M. Mikuž ⁹³, H. Mildner ¹⁰⁰, A. Milic ³⁶,
 D.W. Miller ³⁹, E.H. Miller ¹⁴³, L.S. Miller ³⁴, A. Milov ¹⁶⁹, D.A. Milstead ^{47a,47b}, T. Min ^{14c},
 A.A. Minaenko ³⁷, I.A. Minashvili ^{149b}, L. Mince ⁵⁹, A.I. Mincer ¹¹⁷, B. Mindur ^{86a},
 M. Mineev ³⁸, Y. Mino ⁸⁸, L.M. Mir ¹³, M. Miralles Lopez ⁵⁹, M. Mironova ^{17a}, A. Mishima ¹⁵³,
 M.C. Missio ¹¹³, A. Mitra ¹⁶⁷, V.A. Mitsou ¹⁶³, Y. Mitsumori ¹¹¹, O. Miu ¹⁵⁵,
 P.S. Miyagawa ⁹⁴, T. Mkrtchyan ^{63a}, M. Mlinarevic ⁹⁶, T. Mlinarevic ⁹⁶, M. Mlynarikova ³⁶,
 S. Mobius ¹⁹, P. Mogg ¹⁰⁹, M.H. Mohamed Farook ¹¹², A.F. Mohammed ^{14a,14e}, S. Mohapatra ⁴¹,
 G. Mokgatitwane ^{33g}, L. Moleri ¹⁶⁹, B. Mondal ¹⁴¹, S. Mondal ¹³², K. Mönig ⁴⁸,
 E. Monnier ¹⁰², L. Monsonis Romero ¹⁶³, J. Montejo Berlingen ¹³, M. Montella ¹¹⁹,
 F. Montekali ^{77a,77b}, F. Monticelli ⁹⁰, S. Monzani ^{69a,69c}, N. Morange ⁶⁶,
 A.L. Moreira De Carvalho ^{130a}, M. Moreno Llácer ¹⁶³, C. Moreno Martinez ⁵⁶, P. Morettini ^{57b},
 S. Morgenstern ³⁶, M. Morii ⁶¹, M. Morinaga ¹⁵³, F. Morodei ^{75a,75b}, L. Morvaj ³⁶,
 P. Moschovakos ³⁶, B. Moser ³⁶, M. Mosidze ^{149b}, T. Moskalets ⁵⁴, P. Moskvitina ¹¹³,
 J. Moss ^{31,1}, E.J.W. Moyses ¹⁰³, O. Mtintsilana ^{33g}, S. Muanza ¹⁰², J. Mueller ¹²⁹,
 D. Muenstermann ⁹¹, R. Müller ¹⁹, G.A. Mullier ¹⁶¹, A.J. Mullin ³², J.J. Mullin ¹²⁸, D.P. Mungo ¹⁵⁵,

D. Munoz Perez [ID163](#), F.J. Munoz Sanchez [ID101](#), M. Murin [ID101](#), W.J. Murray [ID167,134](#),
 M. Muškinja [ID17a](#), C. Mwewa [ID29](#), A.G. Myagkov [ID37,a](#), A.J. Myers [ID8](#), G. Myers [ID68](#), M. Myska [ID132](#),
 B.P. Nachman [ID17a](#), O. Nackenhorst [ID49](#), K. Nagai [ID126](#), K. Nagano [ID84](#), J.L. Nagle [ID29,aj](#), E. Nagy [ID102](#),
 A.M. Nairz [ID36](#), Y. Nakahama [ID84](#), K. Nakamura [ID84](#), K. Nakkalil [ID5](#), H. Nanjo [ID124](#), R. Narayan [ID44](#),
 E.A. Narayanan [ID112](#), I. Naryshkin [ID37](#), M. Naseri [ID34](#), S. Nasri [ID116b](#), C. Nass [ID24](#), G. Navarro [ID22a](#),
 J. Navarro-Gonzalez [ID163](#), R. Nayak [ID151](#), A. Nayaz [ID18](#), P.Y. Nechaeva [ID37](#), F. Nechansky [ID48](#),
 L. Nedic [ID126](#), T.J. Neep [ID20](#), A. Negri [ID73a,73b](#), M. Negrini [ID23b](#), C. Nellist [ID114](#), C. Nelson [ID104](#),
 K. Nelson [ID106](#), S. Nemecek [ID131](#), M. Nessi [ID36,h](#), M.S. Neubauer [ID162](#), F. Neuhaus [ID100](#),
 J. Neundorf [ID48](#), R. Newhouse [ID164](#), P.R. Newman [ID20](#), C.W. Ng [ID129](#), Y.W.Y. Ng [ID48](#), B. Ngair [ID116a](#),
 H.D.N. Nguyen [ID108](#), R.B. Nickerson [ID126](#), R. Nicolaidou [ID135](#), J. Nielsen [ID136](#), M. Niemeyer [ID55](#),
 J. Niermann [ID55,36](#), N. Nikiforou [ID36](#), V. Nikolaenko [ID37,a](#), I. Nikolic-Audit [ID127](#), K. Nikolopoulos [ID20](#),
 P. Nilsson [ID29](#), I. Ninca [ID48](#), H.R. Nindhito [ID56](#), G. Ninio [ID151](#), A. Nisati [ID75a](#), N. Nishu [ID2](#),
 R. Nisius [ID110](#), J-E. Nitschke [ID50](#), E.K. Nkadimeng [ID33g](#), T. Nobe [ID153](#), D.L. Noel [ID32](#),
 T. Nommensen [ID147](#), M.B. Norfolk [ID139](#), R.R.B. Norisam [ID96](#), B.J. Norman [ID34](#), M. Noury [ID35a](#),
 J. Novak [ID93](#), T. Novak [ID48](#), L. Novotny [ID132](#), R. Novotny [ID112](#), L. Nozka [ID122](#), K. Ntekas [ID159](#),
 N.M.J. Nunes De Moura Junior [ID83b](#), E. Nurse [ID96](#), J. Ocariz [ID127](#), A. Ochi [ID85](#), I. Ochoa [ID130a](#),
 S. Oerdek [ID48,u](#), J.T. Offermann [ID39](#), A. Ogrodnik [ID133](#), A. Oh [ID101](#), C.C. Ohm [ID144](#), H. Oide [ID84](#),
 R. Oishi [ID153](#), M.L. Ojeda [ID48](#), Y. Okumura [ID153](#), L.F. Oleiro Seabra [ID130a](#), S.A. Olivares Pino [ID137d](#),
 D. Oliveira Damazio [ID29](#), D. Oliveira Goncalves [ID83a](#), J.L. Oliver [ID159](#), Ö.O. Öncel [ID54](#),
 A.P. O'Neill [ID19](#), A. Onofre [ID130a,130e](#), P.U.E. Onyisi [ID11](#), M.J. Oreglia [ID39](#), G.E. Orellana [ID90](#),
 D. Orestano [ID77a,77b](#), N. Orlando [ID13](#), R.S. Orr [ID155](#), V. O'Shea [ID59](#), L.M. Osojnak [ID128](#),
 R. Ospanov [ID62a](#), G. Otero y Garzon [ID30](#), H. Otono [ID89](#), P.S. Ott [ID63a](#), G.J. Ottino [ID17a](#), M. Ouchrif [ID35d](#),
 F. Ould-Saada [ID125](#), M. Owen [ID59](#), R.E. Owen [ID134](#), K.Y. Oyulmaz [ID21a](#), V.E. Ozcan [ID21a](#),
 F. Ozturk [ID87](#), N. Ozturk [ID8](#), S. Ozturk [ID82](#), H.A. Pacey [ID126](#), A. Pacheco Pages [ID13](#),
 C. Padilla Aranda [ID13](#), G. Padovano [ID75a,75b](#), S. Pagan Griso [ID17a](#), G. Palacino [ID68](#), A. Palazzo [ID70a,70b](#),
 J. Pan [ID172](#), T. Pan [ID64a](#), D.K. Panchal [ID11](#), C.E. Pandini [ID114](#), J.G. Panduro Vazquez [ID95](#),
 H.D. Pandya [ID1](#), H. Pang [ID14b](#), P. Pani [ID48](#), G. Panizzo [ID69a,69c](#), L. Paolozzi [ID56](#), S. Parajuli [ID162](#),
 A. Paramonov [ID6](#), C. Paraskevopoulos [ID53](#), D. Paredes Hernandez [ID64b](#), K.R. Park [ID41](#), T.H. Park [ID155](#),
 M.A. Parker [ID32](#), F. Parodi [ID57b,57a](#), E.W. Parrish [ID115](#), V.A. Parrish [ID52](#), J.A. Parsons [ID41](#),
 U. Parzefall [ID54](#), B. Pascual Dias [ID108](#), L. Pascual Dominguez [ID151](#), E. Pasqualucci [ID75a](#),
 S. Passaggio [ID57b](#), F. Pastore [ID95](#), P. Patel [ID87](#), U.M. Patel [ID51](#), J.R. Pater [ID101](#), T. Pauly [ID36](#),
 J. Pearkes [ID143](#), M. Pedersen [ID125](#), R. Pedro [ID130a](#), S.V. Peleganchuk [ID37](#), O. Penc [ID36](#), E.A. Pender [ID52](#),
 K.E. Penski [ID109](#), M. Penzin [ID37](#), B.S. Peralva [ID83d](#), A.P. Pereira Peixoto [ID60](#), L. Pereira Sanchez [ID47a,47b](#),
 D.V. Perepelitsa [ID29,aj](#), E. Perez Codina [ID156a](#), M. Perganti [ID10](#), H. Pernegger [ID36](#), O. Perrin [ID40](#),
 K. Peters [ID48](#), R.F.Y. Peters [ID101](#), B.A. Petersen [ID36](#), T.C. Petersen [ID42](#), E. Petit [ID102](#), V. Petousis [ID132](#),
 C. Petridou [ID152,e](#), A. Petrukhin [ID141](#), M. Pettee [ID17a](#), N.E. Pettersson [ID36](#), A. Petukhov [ID37](#),
 K. Petukhova [ID133](#), R. Pezoa [ID137f](#), L. Pezzotti [ID36](#), G. Pezzullo [ID172](#), T.M. Pham [ID170](#), T. Pham [ID105](#),
 P.W. Phillips [ID134](#), G. Piacquadio [ID145](#), E. Pianori [ID17a](#), F. Piazza [ID123](#), R. Piegai [ID30](#), D. Pietreanu [ID27b](#),
 A.D. Pilkington [ID101](#), M. Pinamonti [ID69a,69c](#), J.L. Pinfeld [ID2](#), B.C. Pinheiro Pereira [ID130a](#),
 A.E. Pinto Pinoargote [ID100,135](#), L. Pintucci [ID69a,69c](#), K.M. Piper [ID146](#), A. Pirttikoski [ID56](#), D.A. Pizzi [ID34](#),
 L. Pizzimento [ID64b](#), A. Pizzini [ID114](#), M.-A. Pleier [ID29](#), V. Plesanovs [ID54](#), V. Pleskot [ID133](#), E. Plotnikova [ID38](#),
 G. Poddar [ID4](#), R. Poettgen [ID98](#), L. Poggioli [ID127](#), I. Pokharel [ID55](#), S. Polacek [ID133](#), G. Polesello [ID73a](#),
 A. Poley [ID142,156a](#), A. Polini [ID23b](#), C.S. Pollard [ID167](#), Z.B. Pollock [ID119](#), E. Pompa Pacchi [ID75a,75b](#),
 D. Ponomarenko [ID113](#), L. Pontecorvo [ID36](#), S. Popa [ID27a](#), G.A. Popeneciu [ID27d](#), A. Poreba [ID36](#),
 D.M. Portillo Quintero [ID156a](#), S. Pospisil [ID132](#), M.A. Postill [ID139](#), P. Postolache [ID27c](#), K. Potamianos [ID167](#),
 P.A. Potepa [ID86a](#), I.N. Potrap [ID38](#), C.J. Potter [ID32](#), H. Potti [ID1](#), T. Poulsen [ID48](#), J. Poveda [ID163](#),
 M.E. Pozo Astigarraga [ID36](#), A. Prades Ibanez [ID163](#), J. Pretel [ID54](#), D. Price [ID101](#), M. Primavera [ID70a](#),

M.A. Principe Martin [ID⁹⁹](#), R. Privara [ID¹²²](#), T. Procter [ID⁵⁹](#), M.L. Proffitt [ID¹³⁸](#), N. Proklova [ID¹²⁸](#),
K. Prokofiev [ID^{64c}](#), G. Proto [ID¹¹⁰](#), J. Proudfoot [ID⁶](#), M. Przybycien [ID^{86a}](#), W.W. Przygoda [ID^{86b}](#),
A. Psallidas [ID⁴⁶](#), J.E. Puddefoot [ID¹³⁹](#), D. Pudzha [ID³⁷](#), D. Pyatiizbyantseva [ID³⁷](#), J. Qian [ID¹⁰⁶](#),
D. Qichen [ID¹⁰¹](#), Y. Qin [ID¹⁰¹](#), T. Qiu [ID⁵²](#), A. Quadt [ID⁵⁵](#), M. Queitsch-Maitland [ID¹⁰¹](#), G. Quetant [ID⁵⁶](#),
R.P. Quinn [ID¹⁶⁴](#), G. Rabanal Bolanos [ID⁶¹](#), D. Rafanoharana [ID⁵⁴](#), F. Ragusa [ID^{71a,71b}](#), J.L. Rainbolt [ID³⁹](#),
J.A. Raine [ID⁵⁶](#), S. Rajagopalan [ID²⁹](#), E. Ramakoti [ID³⁷](#), I.A. Ramirez-Berend [ID³⁴](#), K. Ran [ID^{48,14e}](#),
N.P. Rapheeha [ID^{33g}](#), H. Rasheed [ID^{27b}](#), V. Raskina [ID¹²⁷](#), D.F. Rassloff [ID^{63a}](#), A. Rastogi [ID^{17a}](#),
S. Rave [ID¹⁰⁰](#), B. Ravina [ID⁵⁵](#), I. Ravinovich [ID¹⁶⁹](#), M. Raymond [ID³⁶](#), A.L. Read [ID¹²⁵](#), N.P. Readioff [ID¹³⁹](#),
D.M. Rebuzzi [ID^{73a,73b}](#), G. Redlinger [ID²⁹](#), A.S. Reed [ID¹¹⁰](#), K. Reeves [ID²⁶](#), J.A. Reidelsturz [ID¹⁷¹](#),
D. Reikher [ID¹⁵¹](#), A. Rej [ID⁴⁹](#), C. Rembser [ID³⁶](#), A. Renardi [ID⁴⁸](#), M. Renda [ID^{27b}](#), M.B. Rendel [ID¹¹⁰](#),
F. Renner [ID⁴⁸](#), A.G. Rennie [ID¹⁵⁹](#), A.L. Rescia [ID⁴⁸](#), S. Resconi [ID^{71a}](#), M. Ressegotti [ID^{57b,57a}](#), S. Rettie [ID³⁶](#),
J.G. Reyes Rivera [ID¹⁰⁷](#), E. Reynolds [ID^{17a}](#), O.L. Rezanova [ID³⁷](#), P. Reznicek [ID¹³³](#), N. Ribaric [ID⁹¹](#),
E. Ricci [ID^{78a,78b}](#), R. Richter [ID¹¹⁰](#), S. Richter [ID^{47a,47b}](#), E. Richter-Was [ID^{86b}](#), M. Ridel [ID¹²⁷](#),
S. Ridouani [ID^{35d}](#), P. Rieck [ID¹¹⁷](#), P. Riedler [ID³⁶](#), E.M. Riefel [ID^{47a,47b}](#), J.O. Rieger [ID¹¹⁴](#),
M. Rijssenbeek [ID¹⁴⁵](#), A. Rimoldi [ID^{73a,73b}](#), M. Rimoldi [ID³⁶](#), L. Rinaldi [ID^{23b,23a}](#), T.T. Rinn [ID²⁹](#),
M.P. Rinnagel [ID¹⁰⁹](#), G. Ripellino [ID¹⁶¹](#), I. Riu [ID¹³](#), P. Rivadeneira [ID⁴⁸](#), J.C. Rivera Vergara [ID¹⁶⁵](#),
F. Rizatdinova [ID¹²¹](#), E. Rizvi [ID⁹⁴](#), B.A. Roberts [ID¹⁶⁷](#), B.R. Roberts [ID^{17a}](#), S.H. Robertson [ID^{104,x}](#),
D. Robinson [ID³²](#), C.M. Robles Gajardo [ID^{137f}](#), M. Robles Manzano [ID¹⁰⁰](#), A. Robson [ID⁵⁹](#), A. Rocchi [ID^{76a,76b}](#),
C. Roda [ID^{74a,74b}](#), S. Rodriguez Bosca [ID^{63a}](#), Y. Rodriguez Garcia [ID^{22a}](#), A. Rodriguez Rodriguez [ID⁵⁴](#),
A.M. Rodríguez Vera [ID^{156b}](#), S. Roe [ID³⁶](#), J.T. Roemer [ID¹⁵⁹](#), A.R. Roepe-Gier [ID¹³⁶](#), J. Roggel [ID¹⁷¹](#),
O. Røhne [ID¹²⁵](#), R.A. Rojas [ID¹⁰³](#), C.P.A. Roland [ID¹²⁷](#), J. Roloff [ID²⁹](#), A. Romaniouk [ID³⁷](#),
E. Romano [ID^{73a,73b}](#), M. Romano [ID^{23b}](#), A.C. Romero Hernandez [ID¹⁶²](#), N. Rompotis [ID⁹²](#), L. Roos [ID¹²⁷](#),
S. Rosati [ID^{75a}](#), B.J. Rosser [ID³⁹](#), E. Rossi [ID¹²⁶](#), E. Rossi [ID^{72a,72b}](#), L.P. Rossi [ID^{57b}](#), L. Rossini [ID⁵⁴](#),
R. Rosten [ID¹¹⁹](#), M. Rotaru [ID^{27b}](#), B. Rottler [ID⁵⁴](#), C. Rougier [ID^{102,ab}](#), D. Rousseau [ID⁶⁶](#), D. Rousso [ID³²](#),
A. Roy [ID¹⁶²](#), S. Roy-Garand [ID¹⁵⁵](#), A. Rozanov [ID¹⁰²](#), Z.M.A. Rozario [ID⁵⁹](#), Y. Rozen [ID¹⁵⁰](#),
A. Rubio Jimenez [ID¹⁶³](#), A.J. Ruby [ID⁹²](#), V.H. Ruelas Rivera [ID¹⁸](#), T.A. Ruggeri [ID¹](#), A. Ruggiero [ID¹²⁶](#),
A. Ruiz-Martinez [ID¹⁶³](#), A. Rummler [ID³⁶](#), Z. Rurikova [ID⁵⁴](#), N.A. Rusakovich [ID³⁸](#), H.L. Russell [ID¹⁶⁵](#),
G. Russo [ID^{75a,75b}](#), J.P. Rutherford [ID⁷](#), S. Rutherford Colmenares [ID³²](#), K. Rybacki [ID⁹¹](#), M. Rybar [ID¹³³](#),
E.B. Rye [ID¹²⁵](#), A. Ryzhov [ID⁴⁴](#), J.A. Sabater Iglesias [ID⁵⁶](#), P. Sabatini [ID¹⁶³](#), H.F-W. Sadrozinski [ID¹³⁶](#),
F. Safai Tehrani [ID^{75a}](#), B. Safarzadeh Samani [ID¹³⁴](#), M. Safdari [ID¹⁴³](#), S. Saha [ID¹⁶⁵](#), M. Sahinsoy [ID¹¹⁰](#),
A. Saibel [ID¹⁶³](#), M. Saimpert [ID¹³⁵](#), M. Saito [ID¹⁵³](#), T. Saito [ID¹⁵³](#), D. Salamani [ID³⁶](#), A. Salnikov [ID¹⁴³](#),
J. Salt [ID¹⁶³](#), A. Salvador Salas [ID¹⁵¹](#), D. Salvatore [ID^{43b,43a}](#), F. Salvatore [ID¹⁴⁶](#), A. Salzburger [ID³⁶](#),
D. Sammel [ID⁵⁴](#), D. Sampsonidis [ID^{152,e}](#), D. Sampsonidou [ID¹²³](#), J. Sánchez [ID¹⁶³](#),
V. Sanchez Sebastian [ID¹⁶³](#), H. Sandaker [ID¹²⁵](#), C.O. Sander [ID⁴⁸](#), J.A. Sandesara [ID¹⁰³](#), M. Sandhoff [ID¹⁷¹](#),
C. Sandoval [ID^{22b}](#), D.P.C. Sankey [ID¹³⁴](#), T. Sano [ID⁸⁸](#), A. Sansoni [ID⁵³](#), L. Santi [ID^{75a,75b}](#), C. Santoni [ID⁴⁰](#),
H. Santos [ID^{130a,130b}](#), A. Santra [ID¹⁶⁹](#), K.A. Saoucha [ID¹⁶⁰](#), J.G. Saraiva [ID^{130a,130d}](#), J. Sardain [ID⁷](#),
O. Sasaki [ID⁸⁴](#), K. Sato [ID¹⁵⁷](#), C. Sauer [ID^{63b}](#), F. Sauerburger [ID⁵⁴](#), E. Sauvan [ID⁴](#), P. Savard [ID^{155,ag}](#),
R. Sawada [ID¹⁵³](#), C. Sawyer [ID¹³⁴](#), L. Sawyer [ID⁹⁷](#), I. Sayago Galvan [ID¹⁶³](#), C. Sbarra [ID^{23b}](#), A. Sbrizzi [ID^{23b,23a}](#),
T. Scanlon [ID⁹⁶](#), J. Schaarschmidt [ID¹³⁸](#), U. Schäfer [ID¹⁰⁰](#), A.C. Schaffer [ID^{66,44}](#), D. Schaile [ID¹⁰⁹](#),
R.D. Schamberger [ID¹⁴⁵](#), C. Scharf [ID¹⁸](#), M.M. Schefer [ID¹⁹](#), V.A. Schegelsky [ID³⁷](#), D. Scheirich [ID¹³³](#),
F. Schenck [ID¹⁸](#), M. Schernau [ID¹⁵⁹](#), C. Scheulen [ID⁵⁵](#), C. Schiavi [ID^{57b,57a}](#), E.J. Schioppa [ID^{70a,70b}](#),
M. Schioppa [ID^{43b,43a}](#), B. Schlag [ID^{143,n}](#), K.E. Schleicher [ID⁵⁴](#), S. Schlenker [ID³⁶](#), J. Schmeing [ID¹⁷¹](#),
M.A. Schmidt [ID¹⁷¹](#), K. Schmieden [ID¹⁰⁰](#), C. Schmitt [ID¹⁰⁰](#), N. Schmitt [ID¹⁰⁰](#), S. Schmitt [ID⁴⁸](#),
L. Schoeffel [ID¹³⁵](#), A. Schoening [ID^{63b}](#), P.G. Scholer [ID⁵⁴](#), E. Schopf [ID¹²⁶](#), M. Schott [ID¹⁰⁰](#),
J. Schovancova [ID³⁶](#), S. Schramm [ID⁵⁶](#), T. Schroer [ID⁵⁶](#), H-C. Schultz-Coulon [ID^{63a}](#), M. Schumacher [ID⁵⁴](#),
B.A. Schumm [ID¹³⁶](#), Ph. Schune [ID¹³⁵](#), A.J. Schuy [ID¹³⁸](#), H.R. Schwartz [ID¹³⁶](#), A. Schwartzman [ID¹⁴³](#),
T.A. Schwarz [ID¹⁰⁶](#), Ph. Schwemling [ID¹³⁵](#), R. Schwienhorst [ID¹⁰⁷](#), A. Sciandra [ID¹³⁶](#), G. Sciolla [ID²⁶](#),

F. Scuri ^{74a}, C.D. Sebastiani ⁹², K. Sedlaczek ¹¹⁵, P. Seema ¹⁸, S.C. Seidel ¹¹², A. Seiden ¹³⁶,
 B.D. Seidlitz ⁴¹, C. Seitz ⁴⁸, J.M. Seixas ^{83b}, G. Sekhniaidze ^{72a}, L. Selem ⁶⁰,
 N. Semprini-Cesari ^{23b,23a}, D. Sengupta ⁵⁶, V. Senthilkumar ¹⁶³, L. Serin ⁶⁶, L. Serkin ^{69a,69b},
 M. Sessa ^{76a,76b}, H. Severini ¹²⁰, F. Sforza ^{57b,57a}, A. Sfyrla ⁵⁶, E. Shabalina ⁵⁵, R. Shaheen ¹⁴⁴,
 J.D. Shahinian ¹²⁸, D. Shaked Renous ¹⁶⁹, L.Y. Shan ^{14a}, M. Shapiro ^{17a}, A. Sharma ³⁶,
 A.S. Sharma ¹⁶⁴, P. Sharma ⁸⁰, P.B. Shatalov ³⁷, K. Shaw ¹⁴⁶, S.M. Shaw ¹⁰¹,
 A. Shcherbakova ³⁷, Q. Shen ^{62c,5}, D.J. Sheppard ¹⁴², P. Sherwood ⁹⁶, L. Shi ⁹⁶, X. Shi ^{14a},
 C.O. Shimmin ¹⁷², J.D. Shinner ⁹⁵, I.P.J. Shipsey ¹²⁶, S. Shirabe ⁸⁹, M. Shiyakova ^{38,v},
 J. Shlomi ¹⁶⁹, M.J. Shochet ³⁹, J. Shojaii ¹⁰⁵, D.R. Shope ¹²⁵, B. Shrestha ¹²⁰, S. Shrestha ^{119,ak},
 E.M. Shrif ^{33g}, M.J. Shroff ¹⁶⁵, P. Sicho ¹³¹, A.M. Sickles ¹⁶², E. Sideras Haddad ^{33g},
 A. Sidoti ^{23b}, F. Siegert ⁵⁰, Dj. Sijacki ¹⁵, F. Sili ⁹⁰, J.M. Silva ²⁰, M.V. Silva Oliveira ²⁹,
 S.B. Silverstein ^{47a}, S. Simion ⁶⁶, R. Simoniello ³⁶, E.L. Simpson ⁵⁹, H. Simpson ¹⁴⁶,
 L.R. Simpson ¹⁰⁶, N.D. Simpson ⁹⁸, S. Simsek ⁸², S. Sindhu ⁵⁵, P. Sinervo ¹⁵⁵, S. Singh ¹⁵⁵,
 S. Sinha ⁴⁸, S. Sinha ¹⁰¹, M. Sioli ^{23b,23a}, I. Siral ³⁶, E. Sitnikova ⁴⁸, S.Yu. Sivoklov ^{37,*},
 J. Sjölin ^{47a,47b}, A. Skaf ⁵⁵, E. Skorda ²⁰, P. Skubic ¹²⁰, M. Slawinska ⁸⁷, V. Smakhtin ¹⁶⁹,
 B.H. Smart ¹³⁴, S. Yu. Smirnov ³⁷, Y. Smirnov ³⁷, L.N. Smirnova ^{37,a}, O. Smirnova ⁹⁸,
 A.C. Smith ⁴¹, E.A. Smith ³⁹, H.A. Smith ¹²⁶, J.L. Smith ⁹², R. Smith ¹⁴³, M. Smizanska ⁹¹,
 K. Smolek ¹³², A.A. Snesarev ³⁷, S.R. Snider ¹⁵⁵, H.L. Snoek ¹¹⁴, S. Snyder ²⁹, R. Sobie ^{165,x},
 A. Soffer ¹⁵¹, C.A. Solans Sanchez ³⁶, E.Yu. Soldatov ³⁷, U. Soldevila ¹⁶³, A.A. Solodkov ³⁷,
 S. Solomon ²⁶, A. Soloshenko ³⁸, K. Solovieva ⁵⁴, O.V. Solovyanov ⁴⁰, V. Solovyev ³⁷,
 P. Sommer ³⁶, A. Sonay ¹³, W.Y. Song ^{156b}, A. Sopczak ¹³², A.L. Sopio ⁹⁶, F. Sopkova ^{28b},
 J.D. Sorenson ¹¹², I.R. Sotarriva Alvarez ¹⁵⁴, V. Sothilingam ^{63a}, O.J. Soto Sandoval ^{137c,137b},
 S. Sottocornola ⁶⁸, R. Soualah ¹⁶⁰, Z. Soumami ^{35e}, D. South ⁴⁸, N. Soybelman ¹⁶⁹,
 S. Spagnolo ^{70a,70b}, M. Spalla ¹¹⁰, D. Sperlich ⁵⁴, G. Spigo ³⁶, S. Spinali ⁹¹, D.P. Spiteri ⁵⁹,
 M. Spousta ¹³³, E.J. Staats ³⁴, R. Stamen ^{63a}, A. Stampekis ²⁰, M. Standke ²⁴, E. Stanecka ⁸⁷,
 M.V. Stange ⁵⁰, B. Stanislaus ^{17a}, M.M. Stanitzki ⁴⁸, B. Stapf ⁴⁸, E.A. Starchenko ³⁷,
 G.H. Stark ¹³⁶, J. Stark ^{102,ab}, P. Staroba ¹³¹, P. Starovoitov ^{63a}, S. Stärz ¹⁰⁴, R. Staszewski ⁸⁷,
 G. Stavropoulos ⁴⁶, J. Steentoft ¹⁶¹, P. Steinberg ²⁹, B. Stelzer ^{142,156a}, H.J. Stelzer ¹²⁹,
 O. Stelzer-Chilton ^{156a}, H. Stenzel ⁵⁸, T.J. Stevenson ¹⁴⁶, G.A. Stewart ³⁶, J.R. Stewart ¹²¹,
 M.C. Stockton ³⁶, G. Stoicea ^{27b}, M. Stolarski ^{130a}, S. Stonjek ¹¹⁰, A. Straessner ⁵⁰,
 J. Strandberg ¹⁴⁴, S. Strandberg ^{47a,47b}, M. Stratmann ¹⁷¹, M. Strauss ¹²⁰, T. Strebler ¹⁰²,
 P. Strizenc ^{28b}, R. Ströhmer ¹⁶⁶, D.M. Strom ¹²³, R. Stroynowski ⁴⁴, A. Strubig ^{47a,47b},
 S.A. Stucci ²⁹, B. Stugu ¹⁶, J. Stupak ¹²⁰, N.A. Styles ⁴⁸, D. Su ¹⁴³, S. Su ^{62a}, W. Su ^{62d},
 X. Su ^{62a,66}, K. Sugizaki ¹⁵³, V.V. Sulim ³⁷, M.J. Sullivan ⁹², D.M.S. Sultan ^{78a,78b},
 L. Sultanaliyeva ³⁷, S. Sultansoy ^{3b}, T. Sumida ⁸⁸, S. Sun ¹⁰⁶, S. Sun ¹⁷⁰,
 O. Sunneborn Gudnadottir ¹⁶¹, N. Sur ¹⁰², M.R. Sutton ¹⁴⁶, H. Suzuki ¹⁵⁷, M. Svatos ¹³¹,
 M. Swiatlowski ^{156a}, T. Swirski ¹⁶⁶, I. Sykora ^{28a}, M. Sykora ¹³³, T. Sykora ¹³³, D. Ta ¹⁰⁰,
 K. Tackmann ^{48,u}, A. Taffard ¹⁵⁹, R. Tafirout ^{156a}, J.S. Tafoya Vargas ⁶⁶, Y. Takubo ⁸⁴,
 M. Talby ¹⁰², A.A. Talyshev ³⁷, K.C. Tam ^{64b}, N.M. Tamir ¹⁵¹, A. Tanaka ¹⁵³, J. Tanaka ¹⁵³,
 R. Tanaka ⁶⁶, M. Tanasini ^{57b,57a}, Z. Tao ¹⁶⁴, S. Tapia Araya ^{137f}, S. Tapprogge ¹⁰⁰,
 A. Tarek Abouelfadl Mohamed ¹⁰⁷, S. Tarem ¹⁵⁰, K. Tariq ^{14a}, G. Tarna ^{102,27b}, G.F. Tartarelli ^{71a},
 P. Tas ¹³³, M. Tasevsky ¹³¹, E. Tassi ^{43b,43a}, A.C. Tate ¹⁶², G. Tateno ¹⁵³, Y. Tayalati ^{35e,w},
 G.N. Taylor ¹⁰⁵, W. Taylor ^{156b}, A.S. Tee ¹⁷⁰, R. Teixeira De Lima ¹⁴³, P. Teixeira-Dias ⁹⁵,
 J.J. Teoh ¹⁵⁵, K. Terashi ¹⁵³, J. Terron ⁹⁹, S. Terzo ¹³, M. Testa ⁵³, R.J. Teuscher ^{155,x},
 A. Thaler ⁷⁹, O. Theiner ⁵⁶, N. Themistokleous ⁵², T. Thevenaux-Pelzer ¹⁰², O. Thielmann ¹⁷¹,
 D.W. Thomas ⁹⁵, J.P. Thomas ²⁰, E.A. Thompson ^{17a}, P.D. Thompson ²⁰, E. Thomson ¹²⁸,
 Y. Tian ⁵⁵, V. Tikhomirov ^{37,a}, Yu.A. Tikhonov ³⁷, S. Timoshenko ³⁷, D. Timoshyn ¹³³,

E.X.L. Ting ¹, P. Tipton ¹⁷², S.H. Tlou ^{33g}, A. Tnourji ⁴⁰, K. Todome ¹⁵⁴, S. Todorova-Nova ¹³³,
 S. Todt ⁵⁰, M. Togawa ⁸⁴, J. Tojo ⁸⁹, S. Tokár ^{28a}, K. Tokushuku ⁸⁴, O. Toldaiev ⁶⁸, R. Tombs ³²,
 M. Tomoto ^{84,111}, L. Tompkins ^{143,n}, K.W. Topolnicki ^{86b}, E. Torrence ¹²³, H. Torres ^{102,ab},
 E. Torró Pastor ¹⁶³, M. Toscani ³⁰, C. Tosciri ³⁹, M. Tost ¹¹, D.R. Tovey ¹³⁹, A. Traeet ¹⁶,
 I.S. Trandafir ^{27b}, T. Trefzger ¹⁶⁶, A. Tricoli ²⁹, I.M. Trigger ^{156a}, S. Trincaz-Duvoid ¹²⁷,
 D.A. Trischuk ²⁶, B. Trocmé ⁶⁰, C. Troncon ^{71a}, L. Truong ^{33c}, M. Trzebinski ⁸⁷, A. Trzupiek ⁸⁷,
 F. Tsai ¹⁴⁵, M. Tsai ¹⁰⁶, A. Tsiamis ^{152,e}, P.V. Tsiarehka ³⁷, S. Tsigaridas ^{156a}, A. Tsirigotis ^{152,s},
 V. Tsiskaridze ¹⁵⁵, E.G. Tskhadadze ^{149a}, M. Tsopoulou ^{152,e}, Y. Tsujikawa ⁸⁸, I.I. Tsukerman ³⁷,
 V. Tsulaia ^{17a}, S. Tsuno ⁸⁴, K. Tsuru ¹¹⁸, D. Tsybychev ¹⁴⁵, Y. Tu ^{64b}, A. Tudorache ^{27b},
 V. Tudorache ^{27b}, A.N. Tuna ⁶¹, S. Turchikhin ^{57b,57a}, I. Turk Cakir ^{3a}, R. Turra ^{71a},
 T. Turtuvshin ^{38,y}, P.M. Tuts ⁴¹, S. Tzamarías ^{152,e}, P. Tzanis ¹⁰, E. Tzovara ¹⁰⁰, F. Ukegawa ¹⁵⁷,
 P.A. Ulloa Poblete ^{137c,137b}, E.N. Umaka ²⁹, G. Unal ³⁶, M. Unal ¹¹, A. Undrus ²⁹, G. Unel ¹⁵⁹,
 J. Urban ^{28b}, P. Urquijo ¹⁰⁵, P. Urrejola ^{137a}, G. Usai ⁸, R. Ushioda ¹⁵⁴, M. Usman ¹⁰⁸,
 Z. Uysal ⁸², V. Vacek ¹³², B. Vachon ¹⁰⁴, K.O.H. Vadla ¹²⁵, T. Vafeiadis ³⁶, A. Vaitkus ⁹⁶,
 C. Valderanis ¹⁰⁹, E. Valdes Santurio ^{47a,47b}, M. Valente ^{156a}, S. Valentinetti ^{23b,23a}, A. Valero ¹⁶³,
 E. Valiente Moreno ¹⁶³, A. Vallier ^{102,ab}, J.A. Valls Ferrer ¹⁶³, D.R. Van Arneeman ¹¹⁴,
 T.R. Van Daalen ¹³⁸, A. Van Der Graaf ⁴⁹, P. Van Gemmeren ⁶, M. Van Rijnbach ^{125,36},
 S. Van Stroud ⁹⁶, I. Van Vulpen ¹¹⁴, M. Vanadia ^{76a,76b}, W. Vandelli ³⁶, E.R. Vandewall ¹²¹,
 D. Vannicola ¹⁵¹, L. Vannoli ^{57b,57a}, R. Vari ^{75a}, E.W. Varnes ⁷, C. Varni ^{17b}, T. Varol ¹⁴⁸,
 D. Varouchas ⁶⁶, L. Varriale ¹⁶³, K.E. Varvell ¹⁴⁷, M.E. Vasile ^{27b}, L. Vaslin ⁸⁴, G.A. Vasquez ¹⁶⁵,
 A. Vasyukov ³⁸, F. Vazeille ⁴⁰, T. Vazquez Schroeder ³⁶, J. Veatch ³¹, V. Vecchio ¹⁰¹,
 M.J. Veen ¹⁰³, I. Veliscek ¹²⁶, L.M. Veloce ¹⁵⁵, F. Veloso ^{130a,130c}, S. Veneziano ^{75a},
 A. Ventura ^{70a,70b}, S. Ventura Gonzalez ¹³⁵, A. Verbytskyi ¹¹⁰, M. Verducci ^{74a,74b}, C. Vergis ²⁴,
 M. Verissimo De Araujo ^{83b}, W. Verkerke ¹¹⁴, J.C. Vermeulen ¹¹⁴, C. Vernieri ¹⁴³,
 M. Vessella ¹⁰³, M.C. Vetterli ^{142,ag}, A. Vgenopoulos ^{152,e}, N. Viaux Maira ^{137f}, T. Vickey ¹³⁹,
 O.E. Vickey Boeriu ¹³⁹, G.H.A. Viehhauser ¹²⁶, L. Viganì ^{63b}, M. Villa ^{23b,23a},
 M. Villaplana Perez ¹⁶³, E.M. Villhauer ⁵², E. Vilucchi ⁵³, M.G. Vinciter ³⁴, G.S. Virdee ²⁰,
 A. Vishwakarma ⁵², A. Visibile ¹¹⁴, C. Vittori ³⁶, I. Vivarelli ¹⁴⁶, E. Voevodina ¹¹⁰, F. Vogel ¹⁰⁹,
 J.C. Voigt ⁵⁰, P. Vokac ¹³², Yu. Volkotrub ^{86a}, J. Von Ahnen ⁴⁸, E. Von Toerne ²⁴,
 B. Vormwald ³⁶, V. Vorobel ¹³³, K. Vorobev ³⁷, M. Vos ¹⁶³, K. Voss ¹⁴¹, M. Vozak ¹¹⁴,
 L. Vozdecky ⁹⁴, N. Vranjes ¹⁵, M. Vranjes Milosavljevic ¹⁵, M. Vreeswijk ¹¹⁴, N.K. Vu ^{62d,62c},
 R. Vuillermet ³⁶, O. Vujanovic ¹⁰⁰, I. Vukotic ³⁹, S. Wada ¹⁵⁷, C. Wagner ¹⁰³, J.M. Wagner ^{17a},
 W. Wagner ¹⁷¹, S. Wahdan ¹⁷¹, H. Wahlberg ⁹⁰, M. Wakida ¹¹¹, J. Walder ¹³⁴, R. Walker ¹⁰⁹,
 W. Walkowiak ¹⁴¹, A. Wall ¹²⁸, T. Wamorkar ⁶, A.Z. Wang ¹³⁶, C. Wang ¹⁰⁰, C. Wang ¹¹,
 H. Wang ^{17a}, J. Wang ^{64c}, R.-J. Wang ¹⁰⁰, R. Wang ⁶¹, R. Wang ⁶, S.M. Wang ¹⁴⁸,
 S. Wang ^{62b}, T. Wang ^{62a}, W.T. Wang ⁸⁰, W. Wang ^{14a}, X. Wang ^{14c}, X. Wang ¹⁶²,
 X. Wang ^{62c}, Y. Wang ^{62d}, Y. Wang ^{14c}, Z. Wang ¹⁰⁶, Z. Wang ^{62d,51,62c}, Z. Wang ¹⁰⁶,
 A. Warburton ¹⁰⁴, R.J. Ward ²⁰, N. Warrack ⁵⁹, S. Waterhouse ⁹⁵, A.T. Watson ²⁰, H. Watson ⁵⁹,
 M.F. Watson ²⁰, E. Watton ^{59,134}, G. Watts ¹³⁸, B.M. Waugh ⁹⁶, C. Weber ²⁹, H.A. Weber ¹⁸,
 M.S. Weber ¹⁹, S.M. Weber ^{63a}, C. Wei ^{62a}, Y. Wei ¹²⁶, A.R. Weidberg ¹²⁶, E.J. Weik ¹¹⁷,
 J. Weingarten ⁴⁹, M. Weirich ¹⁰⁰, C. Weiser ⁵⁴, C.J. Wells ⁴⁸, T. Wenaus ²⁹, B. Wendland ⁴⁹,
 T. Wengler ³⁶, N.S. Wenke ¹¹⁰, N. Wermes ²⁴, M. Wessels ^{63a}, A.M. Wharton ⁹¹, A.S. White ⁶¹,
 A. White ⁸, M.J. White ¹, D. Whiteson ¹⁵⁹, L. Wickremasinghe ¹²⁴, W. Wiedenmann ¹⁷⁰,
 M. Wielers ¹³⁴, C. Wiglesworth ⁴², D.J. Wilbern ¹²⁰, H.G. Wilkens ³⁶, D.M. Williams ⁴¹,
 H.H. Williams ¹²⁸, S. Williams ³², S. Willocq ¹⁰³, B.J. Wilson ¹⁰¹, P.J. Windischhofer ³⁹,
 F.I. Winkel ³⁰, F. Winklmeier ¹²³, B.T. Winter ⁵⁴, J.K. Winter ¹⁰¹, M. Wittgen ¹⁴³, M. Wobisch ⁹⁷,
 Z. Wolffs ¹¹⁴, J. Wollrath ¹⁵⁹, M.W. Wolter ⁸⁷, H. Wolters ^{130a,130c}, E.L. Woodward ⁴¹,

S.D. Worm ¹[ID](#)⁴⁸, B.K. Wosiek ¹[ID](#)⁸⁷, K.W. Woźniak ¹[ID](#)⁸⁷, S. Wozniowski ¹[ID](#)⁵⁵, K. Wraight ¹[ID](#)⁵⁹, C. Wu ¹[ID](#)²⁰, J. Wu ¹[ID](#)^{14a,14e}, M. Wu ¹[ID](#)^{64a}, M. Wu ¹[ID](#)¹¹³, S.L. Wu ¹[ID](#)¹⁷⁰, X. Wu ¹[ID](#)⁵⁶, Y. Wu ¹[ID](#)^{62a}, Z. Wu ¹[ID](#)¹³⁵, J. Wuerzinger ¹[ID](#)^{110,ae}, T.R. Wyatt ¹[ID](#)¹⁰¹, B.M. Wynne ¹[ID](#)⁵², S. Xella ¹[ID](#)⁴², L. Xia ¹[ID](#)^{14c}, M. Xia ¹[ID](#)^{14b}, J. Xiang ¹[ID](#)^{64c}, M. Xie ¹[ID](#)^{62a}, X. Xie ¹[ID](#)^{62a}, S. Xin ¹[ID](#)^{14a,14e}, A. Xiong ¹[ID](#)¹²³, J. Xiong ¹[ID](#)^{17a}, D. Xu ¹[ID](#)^{14a}, H. Xu ¹[ID](#)^{62a}, L. Xu ¹[ID](#)^{62a}, R. Xu ¹[ID](#)¹²⁸, T. Xu ¹[ID](#)¹⁰⁶, Y. Xu ¹[ID](#)^{14b}, Z. Xu ¹[ID](#)⁵², Z. Xu ¹[ID](#)^{14c}, B. Yabsley ¹[ID](#)¹⁴⁷, S. Yacoob ¹[ID](#)^{33a}, Y. Yamaguchi ¹[ID](#)¹⁵⁴, E. Yamashita ¹[ID](#)¹⁵³, H. Yamauchi ¹[ID](#)¹⁵⁷, T. Yamazaki ¹[ID](#)^{17a}, Y. Yamazaki ¹[ID](#)⁸⁵, J. Yan ¹[ID](#)^{62c}, S. Yan ¹[ID](#)¹²⁶, Z. Yan ¹[ID](#)²⁵, H.J. Yang ¹[ID](#)^{62c,62d}, H.T. Yang ¹[ID](#)^{62a}, S. Yang ¹[ID](#)^{62a}, T. Yang ¹[ID](#)^{64c}, X. Yang ¹[ID](#)³⁶, X. Yang ¹[ID](#)^{14a}, Y. Yang ¹[ID](#)⁴⁴, Y. Yang ¹[ID](#)^{62a}, Z. Yang ¹[ID](#)^{62a}, W.-M. Yao ¹[ID](#)^{17a}, H. Ye ¹[ID](#)^{14c}, H. Ye ¹[ID](#)⁵⁵, J. Ye ¹[ID](#)^{14a}, S. Ye ¹[ID](#)²⁹, X. Ye ¹[ID](#)^{62a}, Y. Yeh ¹[ID](#)⁹⁶, I. Yeletsikh ¹[ID](#)³⁸, B.K. Yeo ¹[ID](#)^{17b}, M.R. Yexley ¹[ID](#)⁹⁶, P. Yin ¹[ID](#)⁴¹, K. Yorita ¹[ID](#)¹⁶⁸, S. Younas ¹[ID](#)^{27b}, C.J.S. Young ¹[ID](#)³⁶, C. Young ¹[ID](#)¹⁴³, C. Yu ¹[ID](#)^{14a,14e,ai}, Y. Yu ¹[ID](#)^{62a}, M. Yuan ¹[ID](#)¹⁰⁶, R. Yuan ¹[ID](#)^{62b}, L. Yue ¹[ID](#)⁹⁶, M. Zaazoua ¹[ID](#)^{62a}, B. Zabinski ¹[ID](#)⁸⁷, E. Zaid ¹[ID](#)⁵², Z.K. Zak ¹[ID](#)⁸⁷, T. Zakareishvili ¹[ID](#)¹⁶³, N. Zakharchuk ¹[ID](#)³⁴, S. Zambito ¹[ID](#)⁵⁶, J.A. Zamora Saa ¹[ID](#)^{137d,137b}, J. Zang ¹[ID](#)¹⁵³, D. Zanzi ¹[ID](#)⁵⁴, O. Zaplatilek ¹[ID](#)¹³², C. Zeitnitz ¹[ID](#)¹⁷¹, H. Zeng ¹[ID](#)^{14a}, J.C. Zeng ¹[ID](#)¹⁶², D.T. Zenger Jr ¹[ID](#)²⁶, O. Zenin ¹[ID](#)³⁷, T. Ženiš ¹[ID](#)^{28a}, S. Zenz ¹[ID](#)⁹⁴, S. Zerradi ¹[ID](#)^{35a}, D. Zerwas ¹[ID](#)⁶⁶, M. Zhai ¹[ID](#)^{14a,14e}, D.F. Zhang ¹[ID](#)¹³⁹, J. Zhang ¹[ID](#)^{62b}, J. Zhang ¹[ID](#)⁶, K. Zhang ¹[ID](#)^{14a,14e}, L. Zhang ¹[ID](#)^{14c}, P. Zhang ¹[ID](#)^{14a,14e}, R. Zhang ¹[ID](#)¹⁷⁰, S. Zhang ¹[ID](#)¹⁰⁶, S. Zhang ¹[ID](#)⁴⁴, T. Zhang ¹[ID](#)¹⁵³, X. Zhang ¹[ID](#)^{62c}, X. Zhang ¹[ID](#)^{62b}, Y. Zhang ¹[ID](#)^{62c,5}, Y. Zhang ¹[ID](#)⁹⁶, Y. Zhang ¹[ID](#)^{14c}, Z. Zhang ¹[ID](#)^{17a}, Z. Zhang ¹[ID](#)⁶⁶, H. Zhao ¹[ID](#)¹³⁸, T. Zhao ¹[ID](#)^{62b}, Y. Zhao ¹[ID](#)¹³⁶, Z. Zhao ¹[ID](#)^{62a}, A. Zhemchugov ¹[ID](#)³⁸, J. Zheng ¹[ID](#)^{14c}, K. Zheng ¹[ID](#)¹⁶², X. Zheng ¹[ID](#)^{62a}, Z. Zheng ¹[ID](#)¹⁴³, D. Zhong ¹[ID](#)¹⁶², B. Zhou ¹[ID](#)¹⁰⁶, H. Zhou ¹[ID](#)⁷, N. Zhou ¹[ID](#)^{62c}, Y. Zhou ¹[ID](#)^{14c}, Y. Zhou ¹[ID](#)⁷, C.G. Zhu ¹[ID](#)^{62b}, J. Zhu ¹[ID](#)¹⁰⁶, Y. Zhu ¹[ID](#)^{62c}, Y. Zhu ¹[ID](#)^{62a}, X. Zhuang ¹[ID](#)^{14a}, K. Zhukov ¹[ID](#)³⁷, V. Zhulanov ¹[ID](#)³⁷, N.I. Zimine ¹[ID](#)³⁸, J. Zinsser ¹[ID](#)^{63b}, M. Ziolkowski ¹[ID](#)¹⁴¹, L. Živković ¹[ID](#)¹⁵, A. Zoccoli ¹[ID](#)^{23b,23a}, K. Zoch ¹[ID](#)⁶¹, T.G. Zorbas ¹[ID](#)¹³⁹, O. Zormpa ¹[ID](#)⁴⁶, W. Zou ¹[ID](#)⁴¹, L. Zwalinski ¹[ID](#)³⁶.

¹Department of Physics, University of Adelaide, Adelaide; Australia.

²Department of Physics, University of Alberta, Edmonton AB; Canada.

³(^a)Department of Physics, Ankara University, Ankara;(b)Division of Physics, TOBB University of Economics and Technology, Ankara; Türkiye.

⁴LAPP, Université Savoie Mont Blanc, CNRS/IN2P3, Annecy; France.

⁵APC, Université Paris Cité, CNRS/IN2P3, Paris; France.

⁶High Energy Physics Division, Argonne National Laboratory, Argonne IL; United States of America.

⁷Department of Physics, University of Arizona, Tucson AZ; United States of America.

⁸Department of Physics, University of Texas at Arlington, Arlington TX; United States of America.

⁹Physics Department, National and Kapodistrian University of Athens, Athens; Greece.

¹⁰Physics Department, National Technical University of Athens, Zografou; Greece.

¹¹Department of Physics, University of Texas at Austin, Austin TX; United States of America.

¹²Institute of Physics, Azerbaijan Academy of Sciences, Baku; Azerbaijan.

¹³Institut de Física d'Altes Energies (IFAE), Barcelona Institute of Science and Technology, Barcelona; Spain.

¹⁴(^a)Institute of High Energy Physics, Chinese Academy of Sciences, Beijing;(b)Physics Department, Tsinghua University, Beijing;(c)Department of Physics, Nanjing University, Nanjing;(d)School of Science, Shenzhen Campus of Sun Yat-sen University;(e)University of Chinese Academy of Science (UCAS), Beijing; China.

¹⁵Institute of Physics, University of Belgrade, Belgrade; Serbia.

¹⁶Department for Physics and Technology, University of Bergen, Bergen; Norway.

¹⁷(^a)Physics Division, Lawrence Berkeley National Laboratory, Berkeley CA;(b)University of California, Berkeley CA; United States of America.

- ¹⁸Institut für Physik, Humboldt Universität zu Berlin, Berlin; Germany.
- ¹⁹Albert Einstein Center for Fundamental Physics and Laboratory for High Energy Physics, University of Bern, Bern; Switzerland.
- ²⁰School of Physics and Astronomy, University of Birmingham, Birmingham; United Kingdom.
- ²¹(^a) Department of Physics, Bogazici University, Istanbul; (^b) Department of Physics Engineering, Gaziantep University, Gaziantep; (^c) Department of Physics, Istanbul University, Istanbul; Türkiye.
- ²²(^a) Facultad de Ciencias y Centro de Investigaciones, Universidad Antonio Nariño, Bogotá; (^b) Departamento de Física, Universidad Nacional de Colombia, Bogotá; Colombia.
- ²³(^a) Dipartimento di Fisica e Astronomia A. Righi, Università di Bologna, Bologna; (^b) INFN Sezione di Bologna; Italy.
- ²⁴Physikalisches Institut, Universität Bonn, Bonn; Germany.
- ²⁵Department of Physics, Boston University, Boston MA; United States of America.
- ²⁶Department of Physics, Brandeis University, Waltham MA; United States of America.
- ²⁷(^a) Transilvania University of Brasov, Brasov; (^b) Horia Hulubei National Institute of Physics and Nuclear Engineering, Bucharest; (^c) Department of Physics, Alexandru Ioan Cuza University of Iasi, Iasi; (^d) National Institute for Research and Development of Isotopic and Molecular Technologies, Physics Department, Cluj-Napoca; (^e) National University of Science and Technology Politehnica, Bucharest; (^f) West University in Timisoara, Timisoara; (^g) Faculty of Physics, University of Bucharest, Bucharest; Romania.
- ²⁸(^a) Faculty of Mathematics, Physics and Informatics, Comenius University, Bratislava; (^b) Department of Subnuclear Physics, Institute of Experimental Physics of the Slovak Academy of Sciences, Kosice; Slovak Republic.
- ²⁹Physics Department, Brookhaven National Laboratory, Upton NY; United States of America.
- ³⁰Universidad de Buenos Aires, Facultad de Ciencias Exactas y Naturales, Departamento de Física, y CONICET, Instituto de Física de Buenos Aires (IFIBA), Buenos Aires; Argentina.
- ³¹California State University, CA; United States of America.
- ³²Cavendish Laboratory, University of Cambridge, Cambridge; United Kingdom.
- ³³(^a) Department of Physics, University of Cape Town, Cape Town; (^b) iThemba Labs, Western Cape; (^c) Department of Mechanical Engineering Science, University of Johannesburg, Johannesburg; (^d) National Institute of Physics, University of the Philippines Diliman (Philippines); (^e) University of South Africa, Department of Physics, Pretoria; (^f) University of Zululand, KwaDlangezwa; (^g) School of Physics, University of the Witwatersrand, Johannesburg; South Africa.
- ³⁴Department of Physics, Carleton University, Ottawa ON; Canada.
- ³⁵(^a) Faculté des Sciences Ain Chock, Réseau Universitaire de Physique des Hautes Energies - Université Hassan II, Casablanca; (^b) Faculté des Sciences, Université Ibn-Tofail, Kénitra; (^c) Faculté des Sciences Semlalia, Université Cadi Ayyad, LPHEA-Marrakech; (^d) LPMR, Faculté des Sciences, Université Mohamed Premier, Oujda; (^e) Faculté des sciences, Université Mohammed V, Rabat; (^f) Institute of Applied Physics, Mohammed VI Polytechnic University, Ben Guerir; Morocco.
- ³⁶CERN, Geneva; Switzerland.
- ³⁷Affiliated with an institute covered by a cooperation agreement with CERN.
- ³⁸Affiliated with an international laboratory covered by a cooperation agreement with CERN.
- ³⁹Enrico Fermi Institute, University of Chicago, Chicago IL; United States of America.
- ⁴⁰LPC, Université Clermont Auvergne, CNRS/IN2P3, Clermont-Ferrand; France.
- ⁴¹Nevis Laboratory, Columbia University, Irvington NY; United States of America.
- ⁴²Niels Bohr Institute, University of Copenhagen, Copenhagen; Denmark.
- ⁴³(^a) Dipartimento di Fisica, Università della Calabria, Rende; (^b) INFN Gruppo Collegato di Cosenza, Laboratori Nazionali di Frascati; Italy.
- ⁴⁴Physics Department, Southern Methodist University, Dallas TX; United States of America.

- ⁴⁵Physics Department, University of Texas at Dallas, Richardson TX; United States of America.
- ⁴⁶National Centre for Scientific Research "Demokritos", Agia Paraskevi; Greece.
- ⁴⁷(^a) Department of Physics, Stockholm University; (^b) Oskar Klein Centre, Stockholm; Sweden.
- ⁴⁸Deutsches Elektronen-Synchrotron DESY, Hamburg and Zeuthen; Germany.
- ⁴⁹Fakultät Physik, Technische Universität Dortmund, Dortmund; Germany.
- ⁵⁰Institut für Kern- und Teilchenphysik, Technische Universität Dresden, Dresden; Germany.
- ⁵¹Department of Physics, Duke University, Durham NC; United States of America.
- ⁵²SUPA - School of Physics and Astronomy, University of Edinburgh, Edinburgh; United Kingdom.
- ⁵³INFN e Laboratori Nazionali di Frascati, Frascati; Italy.
- ⁵⁴Physikalisches Institut, Albert-Ludwigs-Universität Freiburg, Freiburg; Germany.
- ⁵⁵II. Physikalisches Institut, Georg-August-Universität Göttingen, Göttingen; Germany.
- ⁵⁶Département de Physique Nucléaire et Corpusculaire, Université de Genève, Genève; Switzerland.
- ⁵⁷(^a) Dipartimento di Fisica, Università di Genova, Genova; (^b) INFN Sezione di Genova; Italy.
- ⁵⁸II. Physikalisches Institut, Justus-Liebig-Universität Giessen, Giessen; Germany.
- ⁵⁹SUPA - School of Physics and Astronomy, University of Glasgow, Glasgow; United Kingdom.
- ⁶⁰LPSC, Université Grenoble Alpes, CNRS/IN2P3, Grenoble INP, Grenoble; France.
- ⁶¹Laboratory for Particle Physics and Cosmology, Harvard University, Cambridge MA; United States of America.
- ⁶²(^a) Department of Modern Physics and State Key Laboratory of Particle Detection and Electronics, University of Science and Technology of China, Hefei; (^b) Institute of Frontier and Interdisciplinary Science and Key Laboratory of Particle Physics and Particle Irradiation (MOE), Shandong University, Qingdao; (^c) School of Physics and Astronomy, Shanghai Jiao Tong University, Key Laboratory for Particle Astrophysics and Cosmology (MOE), SKLPPC, Shanghai; (^d) Tsung-Dao Lee Institute, Shanghai; (^e) School of Physics and Microelectronics, Zhengzhou University; China.
- ⁶³(^a) Kirchhoff-Institut für Physik, Ruprecht-Karls-Universität Heidelberg, Heidelberg; (^b) Physikalisches Institut, Ruprecht-Karls-Universität Heidelberg, Heidelberg; Germany.
- ⁶⁴(^a) Department of Physics, Chinese University of Hong Kong, Shatin, N.T., Hong Kong; (^b) Department of Physics, University of Hong Kong, Hong Kong; (^c) Department of Physics and Institute for Advanced Study, Hong Kong University of Science and Technology, Clear Water Bay, Kowloon, Hong Kong; China.
- ⁶⁵Department of Physics, National Tsing Hua University, Hsinchu; Taiwan.
- ⁶⁶IJCLab, Université Paris-Saclay, CNRS/IN2P3, 91405, Orsay; France.
- ⁶⁷Centro Nacional de Microelectrónica (IMB-CNM-CSIC), Barcelona; Spain.
- ⁶⁸Department of Physics, Indiana University, Bloomington IN; United States of America.
- ⁶⁹(^a) INFN Gruppo Collegato di Udine, Sezione di Trieste, Udine; (^b) ICTP, Trieste; (^c) Dipartimento Politecnico di Ingegneria e Architettura, Università di Udine, Udine; Italy.
- ⁷⁰(^a) INFN Sezione di Lecce; (^b) Dipartimento di Matematica e Fisica, Università del Salento, Lecce; Italy.
- ⁷¹(^a) INFN Sezione di Milano; (^b) Dipartimento di Fisica, Università di Milano, Milano; Italy.
- ⁷²(^a) INFN Sezione di Napoli; (^b) Dipartimento di Fisica, Università di Napoli, Napoli; Italy.
- ⁷³(^a) INFN Sezione di Pavia; (^b) Dipartimento di Fisica, Università di Pavia, Pavia; Italy.
- ⁷⁴(^a) INFN Sezione di Pisa; (^b) Dipartimento di Fisica E. Fermi, Università di Pisa, Pisa; Italy.
- ⁷⁵(^a) INFN Sezione di Roma; (^b) Dipartimento di Fisica, Sapienza Università di Roma, Roma; Italy.
- ⁷⁶(^a) INFN Sezione di Roma Tor Vergata; (^b) Dipartimento di Fisica, Università di Roma Tor Vergata, Roma; Italy.
- ⁷⁷(^a) INFN Sezione di Roma Tre; (^b) Dipartimento di Matematica e Fisica, Università Roma Tre, Roma; Italy.
- ⁷⁸(^a) INFN-TIFPA; (^b) Università degli Studi di Trento, Trento; Italy.
- ⁷⁹Universität Innsbruck, Department of Astro and Particle Physics, Innsbruck; Austria.

- ⁸⁰University of Iowa, Iowa City IA; United States of America.
- ⁸¹Department of Physics and Astronomy, Iowa State University, Ames IA; United States of America.
- ⁸²Istinye University, Sariyer, Istanbul; Türkiye.
- ⁸³(^a)Departamento de Engenharia Elétrica, Universidade Federal de Juiz de Fora (UFJF), Juiz de Fora;(^b)Universidade Federal do Rio De Janeiro COPPE/EE/IF, Rio de Janeiro;(^c)Instituto de Física, Universidade de São Paulo, São Paulo;(^d)Rio de Janeiro State University, Rio de Janeiro; Brazil.
- ⁸⁴KEK, High Energy Accelerator Research Organization, Tsukuba; Japan.
- ⁸⁵Graduate School of Science, Kobe University, Kobe; Japan.
- ⁸⁶(^a) AGH University of Krakow, Faculty of Physics and Applied Computer Science, Krakow;(^b) Marian Smoluchowski Institute of Physics, Jagiellonian University, Krakow; Poland.
- ⁸⁷Institute of Nuclear Physics Polish Academy of Sciences, Krakow; Poland.
- ⁸⁸Faculty of Science, Kyoto University, Kyoto; Japan.
- ⁸⁹Research Center for Advanced Particle Physics and Department of Physics, Kyushu University, Fukuoka ; Japan.
- ⁹⁰Instituto de Física La Plata, Universidad Nacional de La Plata and CONICET, La Plata; Argentina.
- ⁹¹Physics Department, Lancaster University, Lancaster; United Kingdom.
- ⁹²Oliver Lodge Laboratory, University of Liverpool, Liverpool; United Kingdom.
- ⁹³Department of Experimental Particle Physics, Jožef Stefan Institute and Department of Physics, University of Ljubljana, Ljubljana; Slovenia.
- ⁹⁴School of Physics and Astronomy, Queen Mary University of London, London; United Kingdom.
- ⁹⁵Department of Physics, Royal Holloway University of London, Egham; United Kingdom.
- ⁹⁶Department of Physics and Astronomy, University College London, London; United Kingdom.
- ⁹⁷Louisiana Tech University, Ruston LA; United States of America.
- ⁹⁸Fysiska institutionen, Lunds universitet, Lund; Sweden.
- ⁹⁹Departamento de Física Teórica C-15 and CIAFF, Universidad Autónoma de Madrid, Madrid; Spain.
- ¹⁰⁰Institut für Physik, Universität Mainz, Mainz; Germany.
- ¹⁰¹School of Physics and Astronomy, University of Manchester, Manchester; United Kingdom.
- ¹⁰²CPPM, Aix-Marseille Université, CNRS/IN2P3, Marseille; France.
- ¹⁰³Department of Physics, University of Massachusetts, Amherst MA; United States of America.
- ¹⁰⁴Department of Physics, McGill University, Montreal QC; Canada.
- ¹⁰⁵School of Physics, University of Melbourne, Victoria; Australia.
- ¹⁰⁶Department of Physics, University of Michigan, Ann Arbor MI; United States of America.
- ¹⁰⁷Department of Physics and Astronomy, Michigan State University, East Lansing MI; United States of America.
- ¹⁰⁸Group of Particle Physics, University of Montreal, Montreal QC; Canada.
- ¹⁰⁹Fakultät für Physik, Ludwig-Maximilians-Universität München, München; Germany.
- ¹¹⁰Max-Planck-Institut für Physik (Werner-Heisenberg-Institut), München; Germany.
- ¹¹¹Graduate School of Science and Kobayashi-Maskawa Institute, Nagoya University, Nagoya; Japan.
- ¹¹²Department of Physics and Astronomy, University of New Mexico, Albuquerque NM; United States of America.
- ¹¹³Institute for Mathematics, Astrophysics and Particle Physics, Radboud University/Nikhef, Nijmegen; Netherlands.
- ¹¹⁴Nikhef National Institute for Subatomic Physics and University of Amsterdam, Amsterdam; Netherlands.
- ¹¹⁵Department of Physics, Northern Illinois University, DeKalb IL; United States of America.
- ¹¹⁶(^a)New York University Abu Dhabi, Abu Dhabi;(^b)United Arab Emirates University, Al Ain; United Arab Emirates.

- ¹¹⁷Department of Physics, New York University, New York NY; United States of America.
- ¹¹⁸Ochanomizu University, Otsuka, Bunkyo-ku, Tokyo; Japan.
- ¹¹⁹Ohio State University, Columbus OH; United States of America.
- ¹²⁰Homer L. Dodge Department of Physics and Astronomy, University of Oklahoma, Norman OK; United States of America.
- ¹²¹Department of Physics, Oklahoma State University, Stillwater OK; United States of America.
- ¹²²Palacký University, Joint Laboratory of Optics, Olomouc; Czech Republic.
- ¹²³Institute for Fundamental Science, University of Oregon, Eugene, OR; United States of America.
- ¹²⁴Graduate School of Science, Osaka University, Osaka; Japan.
- ¹²⁵Department of Physics, University of Oslo, Oslo; Norway.
- ¹²⁶Department of Physics, Oxford University, Oxford; United Kingdom.
- ¹²⁷LPNHE, Sorbonne Université, Université Paris Cité, CNRS/IN2P3, Paris; France.
- ¹²⁸Department of Physics, University of Pennsylvania, Philadelphia PA; United States of America.
- ¹²⁹Department of Physics and Astronomy, University of Pittsburgh, Pittsburgh PA; United States of America.
- ¹³⁰^(a)Laboratório de Instrumentação e Física Experimental de Partículas - LIP, Lisboa; ^(b)Departamento de Física, Faculdade de Ciências, Universidade de Lisboa, Lisboa; ^(c)Departamento de Física, Universidade de Coimbra, Coimbra; ^(d)Centro de Física Nuclear da Universidade de Lisboa, Lisboa; ^(e)Departamento de Física, Universidade do Minho, Braga; ^(f)Departamento de Física Teórica y del Cosmos, Universidad de Granada, Granada (Spain); ^(g)Departamento de Física, Instituto Superior Técnico, Universidade de Lisboa, Lisboa; Portugal.
- ¹³¹Institute of Physics of the Czech Academy of Sciences, Prague; Czech Republic.
- ¹³²Czech Technical University in Prague, Prague; Czech Republic.
- ¹³³Charles University, Faculty of Mathematics and Physics, Prague; Czech Republic.
- ¹³⁴Particle Physics Department, Rutherford Appleton Laboratory, Didcot; United Kingdom.
- ¹³⁵IRFU, CEA, Université Paris-Saclay, Gif-sur-Yvette; France.
- ¹³⁶Santa Cruz Institute for Particle Physics, University of California Santa Cruz, Santa Cruz CA; United States of America.
- ¹³⁷^(a)Departamento de Física, Pontificia Universidad Católica de Chile, Santiago; ^(b)Millennium Institute for Subatomic physics at high energy frontier (SAPHIR), Santiago; ^(c)Instituto de Investigación Multidisciplinario en Ciencia y Tecnología, y Departamento de Física, Universidad de La Serena; ^(d)Universidad Andres Bello, Department of Physics, Santiago; ^(e)Instituto de Alta Investigación, Universidad de Tarapacá, Arica; ^(f)Departamento de Física, Universidad Técnica Federico Santa María, Valparaíso; Chile.
- ¹³⁸Department of Physics, University of Washington, Seattle WA; United States of America.
- ¹³⁹Department of Physics and Astronomy, University of Sheffield, Sheffield; United Kingdom.
- ¹⁴⁰Department of Physics, Shinshu University, Nagano; Japan.
- ¹⁴¹Department Physik, Universität Siegen, Siegen; Germany.
- ¹⁴²Department of Physics, Simon Fraser University, Burnaby BC; Canada.
- ¹⁴³SLAC National Accelerator Laboratory, Stanford CA; United States of America.
- ¹⁴⁴Department of Physics, Royal Institute of Technology, Stockholm; Sweden.
- ¹⁴⁵Departments of Physics and Astronomy, Stony Brook University, Stony Brook NY; United States of America.
- ¹⁴⁶Department of Physics and Astronomy, University of Sussex, Brighton; United Kingdom.
- ¹⁴⁷School of Physics, University of Sydney, Sydney; Australia.
- ¹⁴⁸Institute of Physics, Academia Sinica, Taipei; Taiwan.
- ¹⁴⁹^(a)E. Andronikashvili Institute of Physics, Iv. Javakhishvili Tbilisi State University, Tbilisi; ^(b)High

- Energy Physics Institute, Tbilisi State University, Tbilisi;^(c) University of Georgia, Tbilisi; Georgia.
- ¹⁵⁰Department of Physics, Technion, Israel Institute of Technology, Haifa; Israel.
- ¹⁵¹Raymond and Beverly Sackler School of Physics and Astronomy, Tel Aviv University, Tel Aviv; Israel.
- ¹⁵²Department of Physics, Aristotle University of Thessaloniki, Thessaloniki; Greece.
- ¹⁵³International Center for Elementary Particle Physics and Department of Physics, University of Tokyo, Tokyo; Japan.
- ¹⁵⁴Department of Physics, Tokyo Institute of Technology, Tokyo; Japan.
- ¹⁵⁵Department of Physics, University of Toronto, Toronto ON; Canada.
- ¹⁵⁶^(a)TRIUMF, Vancouver BC;^(b)Department of Physics and Astronomy, York University, Toronto ON; Canada.
- ¹⁵⁷Division of Physics and Tomonaga Center for the History of the Universe, Faculty of Pure and Applied Sciences, University of Tsukuba, Tsukuba; Japan.
- ¹⁵⁸Department of Physics and Astronomy, Tufts University, Medford MA; United States of America.
- ¹⁵⁹Department of Physics and Astronomy, University of California Irvine, Irvine CA; United States of America.
- ¹⁶⁰University of Sharjah, Sharjah; United Arab Emirates.
- ¹⁶¹Department of Physics and Astronomy, University of Uppsala, Uppsala; Sweden.
- ¹⁶²Department of Physics, University of Illinois, Urbana IL; United States of America.
- ¹⁶³Instituto de Física Corpuscular (IFIC), Centro Mixto Universidad de Valencia - CSIC, Valencia; Spain.
- ¹⁶⁴Department of Physics, University of British Columbia, Vancouver BC; Canada.
- ¹⁶⁵Department of Physics and Astronomy, University of Victoria, Victoria BC; Canada.
- ¹⁶⁶Fakultät für Physik und Astronomie, Julius-Maximilians-Universität Würzburg, Würzburg; Germany.
- ¹⁶⁷Department of Physics, University of Warwick, Coventry; United Kingdom.
- ¹⁶⁸Waseda University, Tokyo; Japan.
- ¹⁶⁹Department of Particle Physics and Astrophysics, Weizmann Institute of Science, Rehovot; Israel.
- ¹⁷⁰Department of Physics, University of Wisconsin, Madison WI; United States of America.
- ¹⁷¹Fakultät für Mathematik und Naturwissenschaften, Fachgruppe Physik, Bergische Universität Wuppertal, Wuppertal; Germany.
- ¹⁷²Department of Physics, Yale University, New Haven CT; United States of America.
- ^a Also Affiliated with an institute covered by a cooperation agreement with CERN.
- ^b Also at An-Najah National University, Nablus; Palestine.
- ^c Also at Borough of Manhattan Community College, City University of New York, New York NY; United States of America.
- ^d Also at Center for High Energy Physics, Peking University; China.
- ^e Also at Center for Interdisciplinary Research and Innovation (CIRI-AUTH), Thessaloniki; Greece.
- ^f Also at Centro Studi e Ricerche Enrico Fermi; Italy.
- ^g Also at CERN, Geneva; Switzerland.
- ^h Also at Département de Physique Nucléaire et Corpusculaire, Université de Genève, Genève; Switzerland.
- ⁱ Also at Departament de Física de la Universitat Autònoma de Barcelona, Barcelona; Spain.
- ^j Also at Department of Financial and Management Engineering, University of the Aegean, Chios; Greece.
- ^k Also at Department of Physics, Ben Gurion University of the Negev, Beer Sheva; Israel.
- ^l Also at Department of Physics, California State University, Sacramento; United States of America.
- ^m Also at Department of Physics, King's College London, London; United Kingdom.
- ⁿ Also at Department of Physics, Stanford University, Stanford CA; United States of America.
- ^o Also at Department of Physics, Stellenbosch University; South Africa.
- ^p Also at Department of Physics, University of Fribourg, Fribourg; Switzerland.

- q* Also at Department of Physics, University of Thessaly; Greece.
- r* Also at Department of Physics, Westmont College, Santa Barbara; United States of America.
- s* Also at Hellenic Open University, Patras; Greece.
- t* Also at Institutio Catalana de Recerca i Estudis Avancats, ICREA, Barcelona; Spain.
- u* Also at Institut für Experimentalphysik, Universität Hamburg, Hamburg; Germany.
- v* Also at Institute for Nuclear Research and Nuclear Energy (INRNE) of the Bulgarian Academy of Sciences, Sofia; Bulgaria.
- w* Also at Institute of Applied Physics, Mohammed VI Polytechnic University, Ben Guerir; Morocco.
- x* Also at Institute of Particle Physics (IPP); Canada.
- y* Also at Institute of Physics and Technology, Mongolian Academy of Sciences, Ulaanbaatar; Mongolia.
- z* Also at Institute of Physics, Azerbaijan Academy of Sciences, Baku; Azerbaijan.
- aa* Also at Institute of Theoretical Physics, Ilia State University, Tbilisi; Georgia.
- ab* Also at L2IT, Université de Toulouse, CNRS/IN2P3, UPS, Toulouse; France.
- ac* Also at Lawrence Livermore National Laboratory, Livermore; United States of America.
- ad* Also at National Institute of Physics, University of the Philippines Diliman (Philippines); Philippines.
- ae* Also at Technical University of Munich, Munich; Germany.
- af* Also at The Collaborative Innovation Center of Quantum Matter (CICQM), Beijing; China.
- ag* Also at TRIUMF, Vancouver BC; Canada.
- ah* Also at Università di Napoli Parthenope, Napoli; Italy.
- ai* Also at University of Chinese Academy of Sciences (UCAS), Beijing; China.
- aj* Also at University of Colorado Boulder, Department of Physics, Colorado; United States of America.
- ak* Also at Washington College, Chestertown, MD; United States of America.
- al* Also at Yeditepe University, Physics Department, Istanbul; Türkiye.
- * Deceased